

INFORMATION TO USERS

This manuscript has been reproduced from the microfilm master. UMI films the text directly from the original or copy submitted. Thus, some thesis and dissertation copies are in typewriter face, while others may be from any type of computer printer.

The quality of this reproduction is dependent upon the quality of the copy submitted. Broken or indistinct print, colored or poor quality illustrations and photographs, print bleedthrough, substandard margins, and improper alignment can adversely affect reproduction.

In the unlikely event that the author did not send UMI a complete manuscript and there are missing pages, these will be noted. Also, if unauthorized copyright material had to be removed, a note will indicate the deletion.

Oversize materials (e.g., maps, drawings, charts) are reproduced by sectioning the original, beginning at the upper left-hand corner and continuing from left to right in equal sections with small overlaps. Each original is also photographed in one exposure and is included in reduced form at the back of the book.

Photographs included in the original manuscript have been reproduced xerographically in this copy. Higher quality 6" x 9" black and white photographic prints are available for any photographs or illustrations appearing in this copy for an additional charge. Contact UMI directly to order.

UMI

A Bell & Howell Information Company
300 North Zeeb Road, Ann Arbor MI 48106-1346 USA
313/761-4700 800/521-0600

UNIVERSITY OF OKLAHOMA
GRADUATE COLLEGE

ELECTRICALLY CONDUCTING POLYMER-
MATRIX COMPOSITES: A MORPHOLOGICAL AND
STRUCTURAL PERSPECTIVE

A DISSERTATION
SUBMITTED TO THE GRADUATE FACULTY
in partial fulfillment of the requirements for the
degree of
Doctor of Philosophy

By

William Berlin Genetti

Norman, Oklahoma
1998

UMI Number: 9914412

UMI Microform 9914412
Copyright 1999, by UMI Company. All rights reserved.

**This microform edition is protected against unauthorized
copying under Title 17, United States Code.**


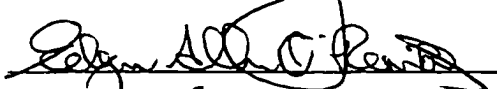
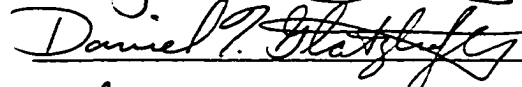
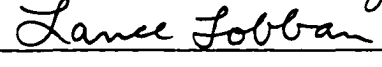
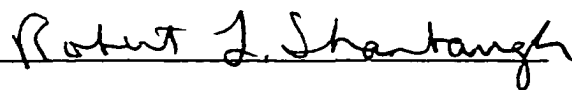
UMI
300 North Zeeb Road
Ann Arbor, MI 48103

© Copyright by WILLIAM BERLIN GENETTI
All Rights Reserved

ELECTRICALLY CONDUCTING POLYMER-MATRIX COMPOSITES:
A MORPHOLOGICAL AND STRUCTURAL PERSPECTIVE

A Dissertation APPROVED FOR THE
SCHOOL OF CHEMICAL ENGINEERING
AND MATERIAL SCIENCE

BY

Dedicated to my parents,
William Ernest and Sandra Lee Genetti
and to my wife,
Majan Marie Genetti,
and to our daughter
Jessica Star

ACKNOWLEDGMENTS

I would like to express my appreciation to my thesis advisor, Brian Grady, who gave me autonomy in much of the work presented in this dissertation. Attempts at experiments were allowed even when his opinion was that the equipment would not work as intended. I would also like to thank Edgar O'Rear, Robert Shambaugh, Lance Lobban, and Daniel Glatzhofer for serving on my dissertation committee.

Special thanks to Edgar O'Rear and Daniel Glatzhofer for both technical discussion and use of equipment for many of the experiments in this work. I would like to thank Dr. Glatzhofer for the many discussions about electrical conductivity measurements that lead to several changes in experimental setup. He also helped in specifying the equipment for conductivity measurements when we invested in equipment for our laboratory.

Several undergraduates need to be acknowledged for their assistance in this work. Jim Yeager helped in getting the solution casting system designed and put into place. Steve Stewart assisted in the initial work with TTF-TCNQ. Richard Lamirand needs special thanks due to the extent of time he spent working in our labs. He helped in solution casting the reticulate doped composites, specifying and setting up the extruder, designing the calendaring system, building the pelletizer, tensile testing, stress

relaxation measurements, and DSC experiments. Phil Doerpinghaus obtained adsorption isotherms for the nickel flake. Aaron Lowe designed a sheeting die for the extruder and did some work with surface modifications to glass fibers by admicellar polymerization. Monil Shah performed many of the surface modifications on silica and alumina and did mechanical property characterization. He also became our resident expert on extrusion of highly filled composites. Sooi Sooi Ooi and Cassandra Auzenne are currently working on an in-situ film formation study of nickel filled LDPE composites. Sooi is working on obtaining temperature profiles as a function of time on extruded films and Cassandra is measuring the viscosity as a function of nickel content. Each of the undergraduates who has worked in our laboratory has made a significant contribution to my research.

The following graduate students have been part of the Grady Group: Bryan McAlister, Jennifer Reynolds, Paul Hunt, Keith Farrell, and Andy Carswell. I would like to thank all of them for their input during technical discussions and their friendship. Special thanks to Paul Hunt for his assistance with the adsorption isotherms and extrusion and to Keith Farrell for helping with the SEM images. I would also like to thank Stephen Henderson, a post-doc in our research group, for going to SSRL and working shifts on the WAXS study. Chung-Li Lai and Wei-Li Yuan, from Dr. O'Rear's group, both assisted in the admicellar polymerization on nickel. Wei-Li also scanned the STM, AFM, and CITS images.

Several pieces of equipment needed to be machined for the stretching and WAXS experiments. I would like to thank Joel Young, from the physics machine shop, for his assistance in designing and building this equipment. Larry Isley, from the CEMS machine shop, assisted in designing and building the following polymer processing equipment: dies, a calendaring system, and a pelletizer. I also appreciate Larry teaching me how to use the equipment in the shop.

Without the assistance of the SSRL staff, the WAXS experiments may never have been completed. Bart Johnson taught me how to align the x-ray beam and assisted in beam alignment during one of our trips to SSRL. Sean Brennan reviewed the proposal for beam time and gave technical advice on the capability of the equipment at SSRL. I also appreciated the technical discussions on WAXS with John Arthur.

Aside from research, other graduate students in some of my classes include: Teri Caldwell, Susan Williams, Sanju Vinekar, and Russell Hooper. They each deserve thanks for spending many hours in our study groups and for their friendship.

During my time in Oklahoma, I have also made a lot of good friends outside of school. Each of these people have been supportive and made life a little nicer. I would like to thank Lowell and Jennifer Johnson, Paul and Cathrine Richichi, Chris and Sharline Blamires, Wayne and Liesa Hokenson, Jim and Denise Elledge, Wes and Jennie Jones, Skip Creveling, David Creveling, and David and Kathie Creveling, for their friendship. Friends from outside Oklahoma who have also kept in close contact include Ashby Johnson and Blake Clark.

My parents, William and Sandra Genetti, taught me the importance of hard work and determination. During many frustrating moments in graduate school, it was these principles that kept me going. My siblings have also been important in my life and want to thank Opal Sanderson, Dominic, Andrew, Vincent, and Teressa Scott for their love and support. My appreciation is especially extended to Dominic for many technical discussions by both telephone and e-mail.

Thanks to my loving wife, Majan, and our daughter, Jessica, for understanding and support. The impact they have made in my life is much greater than anything learned in graduate school. I am eternally grateful for our relationship and the happiness that they have brought into my life. Thank you!

TABLE OF CONTENTS

	Page
ACKNOWLEDGMENTS	v
TABLE OF CONTENTS	ix
LIST OF TABLES	xiv
LIST OF FIGURES	xv
ABSTRACT	xxii
CHAPTER	
1. Introduction	
1.1 Introduction	1
1.2 Conduction Mechanisms	7
1.2.1 Intrinsic Resistance of Fillers	7
1.2.1.1 Band Theory	7
1.2.1.2 Metals	9
1.2.1.3 Organic Conductors	11
1.2.1.4 Charge Transfer Complexes	12
1.2.1.5 Electrically Conductive Polymers	14
1.2.2 Particle – Particle Contact Resistance	14
1.2.3 Tunneling Resistance	16
1.2.4 Temperature Dependence of Conductivity	17

1.3 Percolation Theory	20
1.4 Project Overview	25
1.5 Notation	27
1.6 References	29
2. Experimental Procedures	
2.1 Introduction	32
2.2 Composite Film Preparation	32
2.2.1 Solution Casting	32
2.2.2 Powder Mixing	33
2.2.3 Extrusion	33
2.2.4 Uniaxial Orientation	36
2.3 Morphological Studies	36
2.3.1 Orientation Characterization Through Wide Angle X-Ray Scattering (WAXS)	36
2.3.2 Optical Microscope	42
2.3.3 Atomic Force Microscopy (AFM) and Scanning Tunneling Microscopy (STM)	42
2.3.4 Scanning Electron Microscopy	43
2.3.5 Fractional Crystallinity	43
2.4 Isothermal Crystallization	45
2.5 Physical Property Evaluation	48
2.5.1 Conductivity Measurements	48
2.5.2 Thermal Conductivity Ratio	51
2.5.3 Tensile Properties	51

2.5.4 Stress Relaxation Measurements	52
2.6 Notation	53
2.7 References	56
3. Wide Angle X-Ray Scattering Study of Crystalline Orientation in Reticulate Doped Polymer Composites	
3.1 Introduction	58
3.2 Background and Literature Review	59
3.3 Experimental Procedures	62
3.4 Results and Discussion	63
3.5 Conclusions	83
3.6 Notation	85
3.7 References	86
4. Isothermal Crystallization of Nickel Filled Low Low Density Polyethylene	
4.1 Introduction	88
4.2 Background and Literature Search	89
4.2.1 Isothermal Crystallization	89
4.2.2 Thermal Conductivity	93
4.3 Experimental Procedures	94
4.4 Results and Discussion	95
4.4.1 Electrical Conductivity	95
4.4.2 Scanning Electron Microscopy	95
4.4.3 Isothermal Crystallization	101

4.4.4 Fractional Crystallinity	105
4.5 Conclusions	109
4.6 Notation	112
4.7 References	113
5. Polymer Matrix Composites: Conductivity Enhancement Through Polypyrrole Coating of Particulates	
5.1 Introduction	115
5.2 Background and Literature Review	116
5.2.1 Admicellar Polymerization	118
5.2.1.1 Admicelle Formation	118
5.2.1.2 Solubilization	120
5.2.1.3 Polymerization	120
5.2.1.4 Washing	120
5.3 Experimental Procedures	122
5.3.1 Adsorption Isotherms	122
5.3.2 Admicellar Polymerization	123
5.3.3 Particulate Characterization	124
5.3.4 Film Preparation	124
5.3.5 Characterization	125
5.4 Results and Discussion	127
5.4.1 Adsorption Isotherms	127
5.4.2 Particulate Characterization	130
5.4.3 Nickel Composites	134

5.4.3.1 Conductivity	134
5.4.3.2 Crystallinity	139
5.4.3.3 Mechanical Properties	144
5.4.4 Alumina and Glass Fiber Composites	144
5.5 Conclusions	151
5.6 Notation	153
5.7 References	154
6. Conclusions and Future Work	
6.1 Introduction	156
6.2 How Does the Presence of the Filler effect the Polymer?	157
6.2.1 Polymer Crystallite Orientation	157
6.2.2 Crystallization	158
6.3 How Does Modification of the Particulate's Surface Effect the Properties of the Composite Material?	162
6.4 Conclusions	164
Appendix	
A. X-Ray Beam Alignment of The Huber 6-Circle Diffractometer: Stanford Synchrotron Radiation Laboratory Beam Line 7-2	165
B. DSC Calibration Procedures	184
C. Step-by-step TTF Synthesis Procedures	194

LIST OF TABLES

TABLE	PAGE
3-1 Crystallographic Parameters and Physical Properties	70
5-1 Polymerization Conditions	126

LIST OF FIGURES

FIGURE	PAGE
1-1 Percolation Theory	4
1-2 Resistances in Composites	8
a. Intrinsic Resistance of Filler	
b. Particle – Particle Contact Resistance	
c. Tunneling Resistance	
1-3 Band Theory	10
a. Conductor	
b. Semi-conductor	
c. Insulator	
1-4 Organic Conductors	13
a. Charge Transfer Complexes: tetrathiafulvalene-tetracyanoquinodimethane (TTF-TCNQ)	
b. Conductive Polymers: polypyrrole	
1-5 Tunneling Potential Barrier	15
1-6 Temperature Dependence of Composite Resistivity in Iron Filled Styrene-Acrylonitrile Composite Below the Critical Volume Fraction ($V < V_c$)	18
1-7 Temperature Dependence of Composite Resistivity in Iron Filled Styrene-Acetonitrile Composites at a	19

	Concentration of 30% by Volume ($V > V_c$)	
1-8	Statistical Percolation Model	21
2-1	Extrusion Processing	34
	a. Pelletizer	
	b. Calendaring	
2-2	Stretcher	35
2-3	WAXS Patterns;	37
	a. Unoriented Sample	
	b. Oriented Sample	
2-4	a. WAXS Coordination System	38
	b. WAXS Experimental Geometry	
2-5	Schematic Diagram of DSC Melting Curve	44
2-6	DSC Output for LDPE at 100°C;	46
	a. Raw Data	
	b. Cooling Curve	
	c. Corrected Data with Features Due Totally to Crystallization	
2-7	Crystallinity as a Function of Time for LDPE at 100°C	47
2-8	Geometry for Different Conductivity Measurements;	50
	a. Four Point Probe	
	b. Sandwich	
	c. Powder Conductivity	
3-1	Percolation Diagram for TTF-TCNQ filled PE	65

3-2	Optical Microscope Image of TTF-TCNQ Particles;	66
	a. 320X Magnification	
	b. 800X Magnification	
3-3	a. Maximum Aspect Ratio of TTF-TCNQ as a Function of TTF-TCNQ Concentration	67
	b. Average Aspect Ratio of TTF-TCNQ as a Function of TTF-TCNQ Concentration	
3-4	Diffraction Pattern for TTF-TCNQ	68
3-5	Diffraction Pattern for PE	69
3-6	WAXS Comparison for TTF-TCNQ and PE	72
3-7	Chi Scan at 21.4° for a 10% by Volume TTF-TCNQ Composite	73
	a. Unstretched	
	b. Stretched to $\lambda=2.0$	
3-8	Orientation of Unstretched TTF-TCNQ filled PE as a Function of Filler Volume Fraction	74
3-9	Orientation of Stretched TTF-TCNQ-Filled PE as a Function of Draw Ratio and Filler Volume Fraction	76
3-10	Stress Relaxation of TTF-TCNQ-Filled PE as a Function of Filler Loading	77
3-11	a. Slower Relaxation Time as a Function of Volume Fraction TTF-TCNQ	80
	b. Faster Relaxation Time as a Function of Volume Fraction TTF-TCNQ	

3-12	Composite Conductivity as a Function of Volume Fraction TTF-TCNQ and Draw Ratio	81
3-13	Baseline Subtracted DSC Curves for Stretched, 2.5 % TTF-TCNQ Composite Films as a Function of Draw Ratio	82
3-14	Fractional Crystallinity of TTF-TCNQ-Filled PE as a Function of Draw Ratio	84
4-1	Percolation Diagram for Nickel Filled LDPE	96
4-2	SEM Images for Nickel Filled LDPE at a Magnification of 300X	97
4-3	Uncorrected Crystallization Curves for PE at Various Temperatures	100
4-4	Crystallization as a Function of volume Fraction for 2.5, 5, 10, and 20 Percent Nickel Filled LDPE	103
4-5	Avrami Rate Constant, K , as a Function of Temperature and Nickel Content in Nickel Filled LDPE	104
4-6	Heat Transfer Effects;	106
	a. Thermal Conductivity Ratio, k_c/k_p	
	b. Avrami Rate Constant Ratio $(K_c/K_p)^{1/3}$, Which Corresponds to the Ratio of the Linear Growth Rates, G_c/G_p	
4-7	Crystallization as a Function of Volume Fraction for 5, 10, 15, and 20 Percent Silica Filled LDPE	107

4-8	Avrami Exponent, n , as a Function of Temperature and Concentration in Nickel Filled LDPE	108
4-9	Fractional Crystallinity;	111
	a. As a Function of Nickel Concentration for Extruded LDPE Composite Films	
	b. As a Function of Temperature and Nickel Volume Fraction in Isothermally Crystallized LDPE Composite Films	
5-1	Schematic Diagram of the Admicellar Polymerization Process	119
5-2	Schematic Diagram of an Adsorption Isotherm	121
5-3	Adsorption Isotherm of Sodium Dodecyl Sulfate on Nickel Flake	128
5-4	Adsorption Isotherm of Sodium Dodecyl Sulfate on Glass Fibers at a pH of 3.0	129
5-5	STM Image of PPy-coated Nickel Flake	131
5-6	AFM Images of Bare (left) and PPy-coated (right) Nickel Foils	132
5-7	STM and CITS Images of PPy-coated Nickel	133
5-8	Percolation Diagram for Nickel and PPy-coated Nickel by Solution Casting	135
5-9	Schematic Diagram of Molecular Wire Formation in PPy-coated Nickel-LDPE Composites	137

5-10	Percolation Diagram for Nickel and PPy-coated Nickel by Extrusion	140
5-11	Conductivity versus Draw Ratio for Nickel and PPy-coated Nickel-LDPE Composites in the Critical Region (7 % by volume filler)	141
5-12	Conductivity versus Draw Ratio for Nickel and PPy-coated Nickel-LDPE Composites Above the Critical Region (13 % by volume filler)	142
5-13	Schematic Diagram of PPy Entanglements During Stretching	143
5-14	Crystallinity versus Concentration of Nickel-LDPE and PPy-coated Nickel-LDPE Composites	145
5-15	Tensile Modulus versus Concentration of Nickel-LDPE and PPy-coated Nickel-LDPE Composites	147
5-16	Elongation at Break versus Concentration of Nickel-LDPE and PPy-coated Nickel-LDPE Composites	148
5-17	Ultimate Strength versus Concentration of Nickel-LDPE and PPy-coated Nickel-LDPE Composites	149
5-18	Percolation Diagram for Powder Mixed Alumina	150
6-1	Plunger Extruder with Die and Stretching Apparatus	160
6-2	Extruder and Stretcher Shown in χ -Circle	161
A-1	X-ray Experimental Setup;	167
	a. Photograph	
	b. Schematic Diagram	

A-2	Side View of Huber Diffractometer with Ionization Chamber used in Alignment	169
A-3	Side View of Chi and Phi Circles	172
A-4	Front View of Chi and Phi Circles	173
A-5	Photograph of Chi and Phi Circles with Calibration Pin in Goniometer Head.	174
A-6	Pinhole for Alignment	176
A-7	Photograph of Pinhole on Goniometer Head	177
B-1	Changes in DSC Controls;	187
	a. Calibration Zero	
	b. Calibration Range	
	c. ΔT_b	
B-2	ΔT_b Change Estimation; Initial and Final Peaks are Program Peaks	188
B-3	Schematic Diagram of Base Line with Initial and Final Temperature Program Peaks	189
C-1	a. 1,3-dithiole-2-thione	195
	b. Synthesis of Sodium Acetylenide	
C-2	a. Reaction of Sodium Acetylenide with Sulfur	197
	b. Reaction with Carbon Disulfide	
C-3	Acidification	200

ABSTRACT

Past research on conductive polymer-matrix composites has focused on the relationships between concentration, geometry, and dispersion of the discontinuous phase and the physical properties of the resulting material. However, the volume fraction – geometry approach does not take into account the influence of polymer morphology and polymer-filler interactions on the composite properties. The work presented in this dissertation addresses the changes in the polymer morphology and structure resulting from the addition of the conductive filler. In addition, the effect of modifying the polymer-filler interface in conductive composites on the physical properties of the resulting material was also investigated.

Wide angle x-ray scattering (WAXS), conductivity, optical microscopy, stress relaxation, and differential scanning calorimetry (DSC) measurements, were used to show the effect of filler addition and uniaxial orientation on the morphology of the matrix and the physical properties of reticulate doped polymer composites. Reticulate doping consists of casting a composite film from a solution containing a polymer and a charge-transfer complex (CTC) and allowing the conductive, free radical salt to recrystallize as the solvent is removed from the polymer. In this study, the CTC, tetrathiafulvalene-tetracyanoquinodimethane (TTF-TCNQ) was supported by PE. It has

been shown that increasing TTF-TCNQ concentration shifts the preferential orientation of the crystalline phase of the PE from slightly perpendicular to slightly parallel to the casting surface. WAXS measurements were made on samples that were uniaxially stretched at 80°C and cooled to room temperature. These experiments showed a smaller incremental increase in crystalline orientation with increasing TTF-TCNQ. This observation was consistent with a drop in initial relaxation times calculated from room temperature stress relaxation experiments. In the unoriented composites, increasing TTF-TCNQ loading had no effect on PE crystallinity, however, the increase in crystallinity caused by uniaxial stretching was decreased by the presence of TTF-TCNQ.

Isothermal crystallization experiments have been carried out for nickel - low-density polyethylene (LDPE) composites from 95° to 104° C. In this study, the effect of nickel in filled LDPE composites on the crystallization kinetics of the LDPE crystallites has been quantified and compared to the filler's effect on electrical and thermal properties. The crystallization kinetics were altered by the nickel addition in two ways; reducing the nucleation time for a given isothermal crystallization temperature and increasing the crystallization rate. The rates were compared by fitting the data to the Avrami equation. The Avrami exponent was not effected by the addition of nickel, indicating the change was due to increased crystal growth rate rather than a nucleation effect. An upward shift in the Avrami rate constant was found between 7.5 and 10 percent nickel by volume for all temperatures studied. The shift occurred at the end of the critical region in electrical conductivity, and we believe the shift is due to the formation of a continuous network of

nickel particles causing an increase in the local heat dissipation. The network of nickel particles described by percolation statistics, used to characterize electrical conductivity, is also useful in explaining the changes in crystallization kinetics.

The electrical resistance of polymeric materials loaded with conductive fillers can be divided into three major categories: the intrinsic resistance of the filler and matrix, the particle-particle contact resistance, and the tunneling resistance. A method for decreasing both the particle-particle contact and tunneling resistance in particulate filled LDPE composites which involves coating the particles with polypyrrole (PPy) using admicellar polymerization has been developed. Nickel flake, alumina, and glass fibers were used as substrates for polymerization and represent conductive, resistive, and insulating materials, respectively. Addition of PPy to the conductive and resistive particulates lead to an increase of 2 to 4 orders of magnitude in composite conductivity at concentrations above the percolation threshold without significantly changing the thermal or mechanical properties of the composite. It is believed that these resistances are reduced by the formation of PPy “molecular wires” which occur as a result of chain entanglements at high filler loading. Samples prepared by different polymer-filler mixing techniques had different plateau conductivities, indicating that the processing method influences the composite conductivity. The incremental increase in conductivity of glass fiber - LDPE composites due to the PPy-coating was minimal. The limitation of this technology is the ability to get uniform coverage necessary to obtain greater increases in conductivity on non-conductive substrates.

ELECTRICALLY CONDUCTING POLYMER- MATRIX COMPOSITES: A MORPHOLOGICAL AND STRUCTURAL PERSPECTIVE

CHAPTER 1

INTRODUCTION

1.1 INTRODUCTION

Electrically conducting thermoplastic composites consist of a conductive filler supported by an insulating polymer matrix. The advantages of using thermoplastic composites versus other conducting materials include processibility, flexibility, ability to absorb mechanical shock, corrosion resistance, tunable thermal conductivity, ability to form complex parts, parts consolidation, and conductivity control.¹ Much of the research in conductive composites was initiated to find an inexpensive method for electromagnetic shielding of computers and electronic equipment as these devices moved from shielded rooms to desktops in homes and offices. Examples of other applications for conductive composites, both present and future, include conductive adhesives, cold-forming

electronic connections (solders), switching devices, electronic packaging, and surge protection devices.^{2,3}

Polymer-matrix composites can be made using either thermoplastics or thermosets as the supporting matrix.⁴ Thermoplastics are polymers which melt upon heating, and thermoplastic-matrix composites are formed by melting or dissolving the insulating phase, then combining it with the conductive phase through conventional mixing methods. Thermoplastic composite products can be shaped and formed through typical polymer processing techniques such as injection molded or extrusion. Thermosets are cross-linked polymers, which do not dissolve and degrade before melting. Thermoset composites are produced by mixing the conductive filler with a monomer or an uncrosslinked polymer, then allowing the crosslinking reaction to take place. Two-part epoxies are the most common thermoset-matrix for conductive composites, and parts that require shaping are often processed by reaction injection molding.

Electrically conducting thermoplastic composites were first introduced into the commercial market as electronic packaging for computer chips, motherboards, memory chips, and other devices. Electronic packaging is still the largest market, and these composites have traditionally been carbon black filled polyethylene or polypropylene because carbon black does not deteriorate the mechanical properties to the same degree as metals. Recently, aluminum filled composites have also been used where high conductivity is required. Conductive epoxies have traditionally been marketed as conductive adhesives and cold-forming solders. These applications use epoxies filled

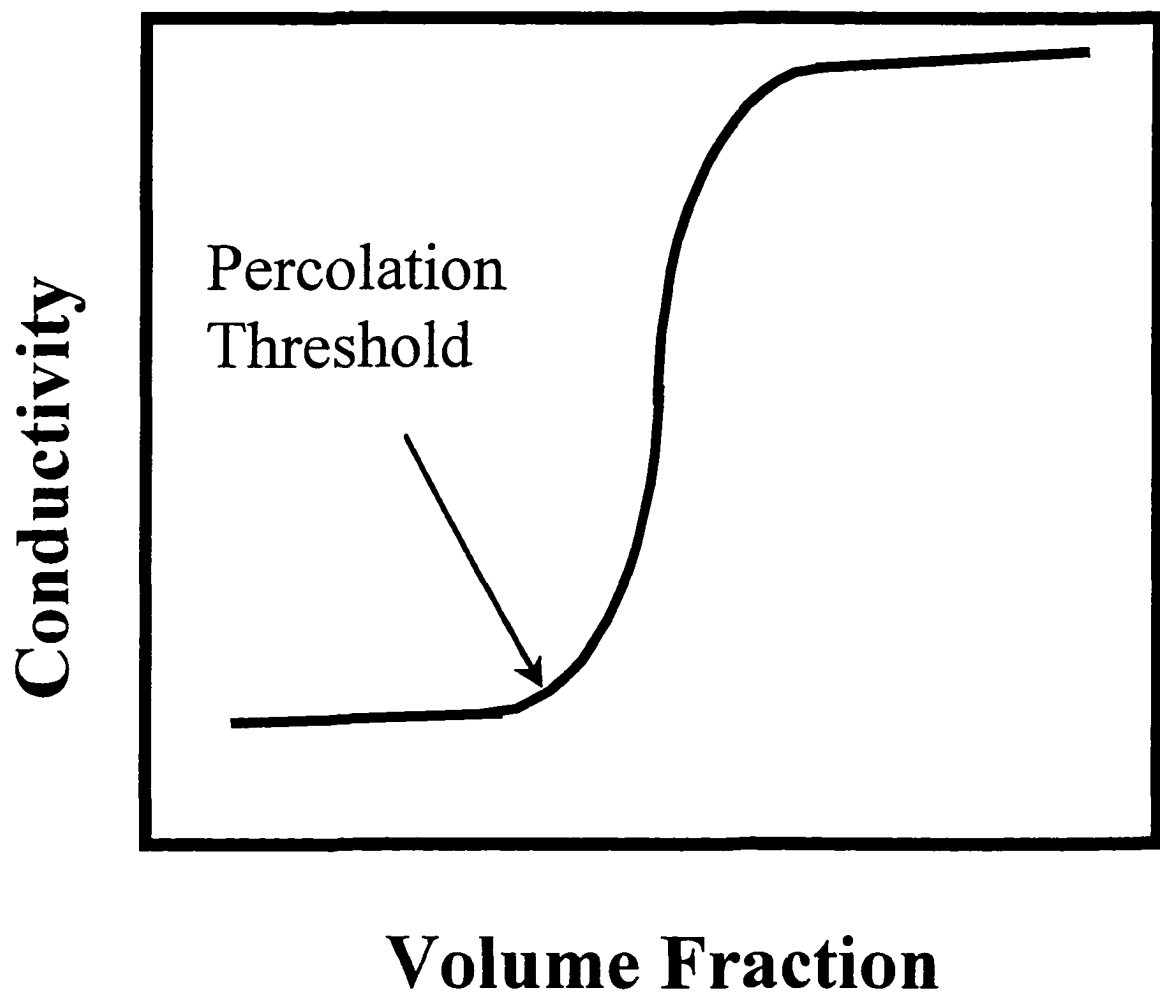
with gold, silver, nickel, or copper flake or fibers, which allow conductivity on the order of 10^3 S/cm.

Two landmark studies of conduction in metal filled polymers were reported by Gurland in 1966, and Malliaris and Turner in 1971. Gurland studied hot pressed polymers filled with silver and showed that there was a relationship between the degree of contiguity or connectedness and conduction.⁵ In order to achieve conduction in filled polymer systems, conductive pathways of filler particles must form throughout the matrix allowing electrons to freely move from one side of the material to another.⁶ Percolation statistics quantitatively relates the volume fraction of the filler to the electrical conductivity of the composite.^{5,7} As shown in Figure 1-1, the composite conductivity increases slowly with increasing filler concentration until the critical volume fraction is reached.⁸ At V_c , which is termed the critical volume fraction or the percolation threshold, a very sharp jump in conductivity is obtained over a very small range in concentration, referred to as the critical region. In this critical region the conductivity, σ , and concentration have a power law relationship as given by Equation 1-1,

$$\sigma \propto (V - V_c)^{t_{per}} \quad [1-1]$$

where V is the volume fraction.⁹ The power law index, t_{per} , is a function of the interactions between the polymer and the matrix.¹⁰ The critical region ends when all of the filler particles are involved in at least one conductive pathway and higher filler concentrations only achieve moderate changes in conductivity.

Figure 1-1 Percolation Statistics



The size and shape of the filler particles affect the percolation threshold. As the size of the filler particles decreases, the surface area available for conductive contacts increases relative to particle volume, thus causing the formation of conductive pathways at lower volume fractions. For spherical powders, the percolation threshold is approximately 30 percent filler by volume, but if fibers are used, the critical volume fraction becomes a function of the aspect ratio (length divided by diameter). For aspect ratios larger than 100, conduction can occur at a volume fraction as low as 6 percent.

Janzen was the first to point out that the conductivity data for composite materials, even with the same filler and polymer, was inconsistent.¹¹ This inconsistency may be a result of the samples having different polymer morphologies. In systems of carbon black supported by polypropylene (PP), acrylonitrile butadiene styrene terpolymer (ABS), and polycarbonate (PC), PP composites had a higher conductivity at a given filler concentration. Since PP is semi-crystalline, the filler particles were excluded from the crystalline regions increasing the filler concentration in the amorphous phase, thus increasing the probability of forming conductive pathways and lowering the critical volume fraction.¹² Recently, the dependence of the composite conductivity on the morphology of the matrix polymer was shown by isolating carbon black in one phase of a polymer blend.¹³ V_c is also affected by the dispersion and morphology of the filler particles. Malliaris and Turner studied pressed, powder-mixed composites of nickel-filled polyethylene (PE) and polyvinylchloride (PVC) resins which formed segregated phases of metal and polymer.¹⁴ By increasing the degree of segregation, the critical

volume fraction was reduced. Choosing a semicrystalline polymer as the matrix can induce this segregation. Bigg *et al.* have shown that the filler particles are excluded from the crystalline regions of the sample, thus increasing the absolute filler concentration in the amorphous regions.¹⁵ Since the amorphous regions of the polymer tend to be continuous, conductive pathways form at lower bulk concentrations, thus requiring less filler content to achieve the same conductivity.

Above the critical volume fraction, the composite conductivity is affected by the intrinsic conductivity of the filler and matrix, and polymer-filler interactions. In systems with high polymer-filler adhesion, the polymer forms a thick film around the conductive filler which limits the particle-particle contact, thus the composite has low conductivity but good mechanical properties. In systems with weak polymer-filler adhesion, the particles have a higher probability of contacting, but the mechanical properties deteriorate significantly.¹⁶ The intrinsic balance between conduction and mechanical properties has been a major stumbling block in bringing electrically conducting thermoplastic composites to many commercial markets.

The parameters summarized below have experimentally been shown to effect the conductivity of electrically conducting thermoplastic composite:⁹

- The type, size, or shape of the filler particles.
- The dispersion of the filler in the polymer matrix.
- The volume fraction of the filler.
- The interactions between the polymer and the conductive filler.

- The morphology and crystallinity of the matrix polymer.

1.2 CONDUCTION MECHANISMS

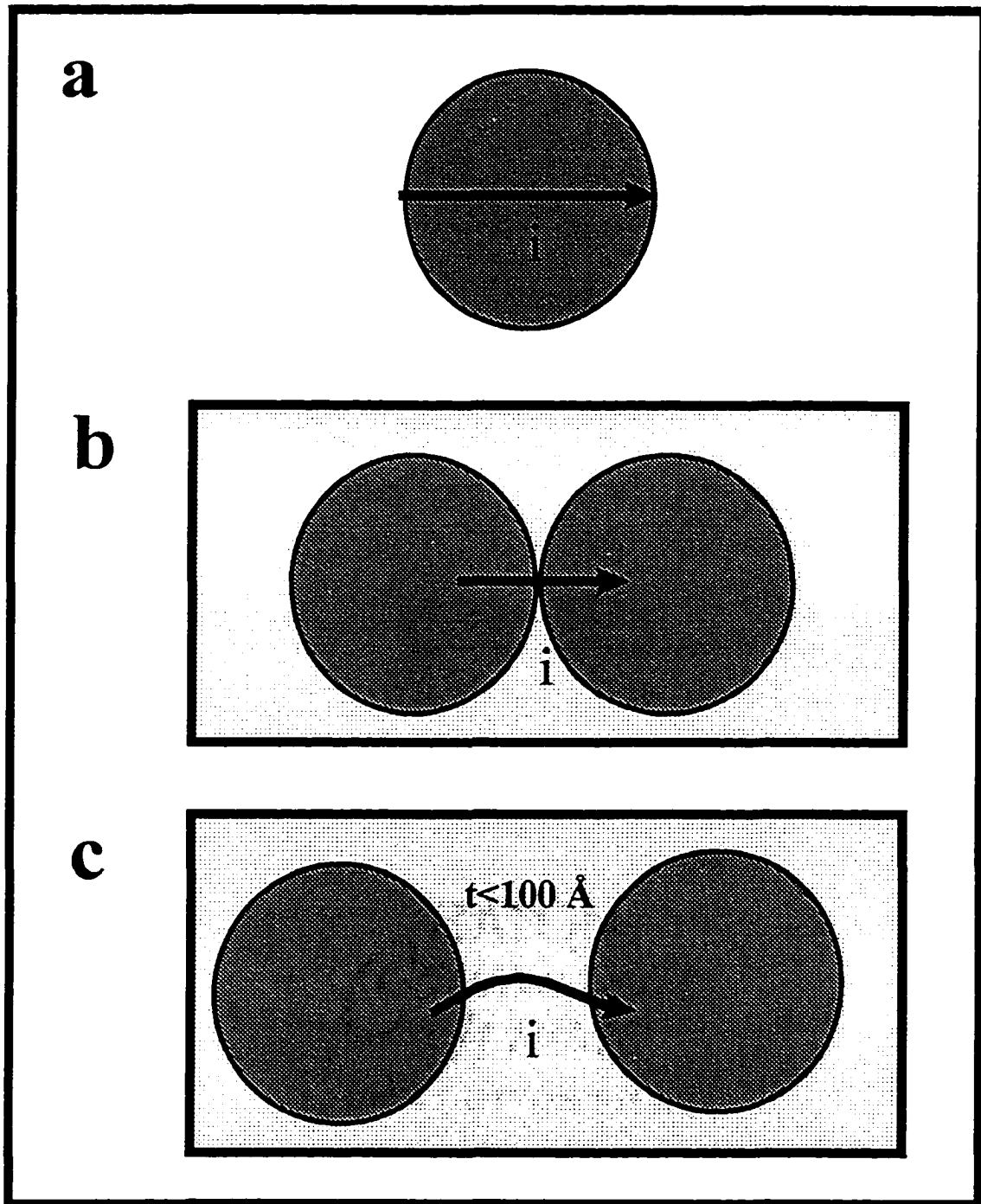
The resistance to electron flow in conductive composites, schematically shown in Figure 1-2, is comprised of three resistances: the intrinsic resistivity of the filler material, the particle-particle contact resistance, and the tunneling resistance.¹⁷ The particle-particle contact resistance is the resistance due to forcing the electron through a small conductive area. The tunneling resistance is a result of electrons passing through a very thin insulating film which is possible when the film thickness is less than 100 Å. Any modifications to the composite that affect at least one of the three resistances can change the composite conductivity.

1.2.1 Intrinsic Resistance of the Filler

1.2.1.1 *Band Theory*

Band theory explains the differences between conduction mechanisms for conductors, semi-conductors, and insulators, as well as describes the necessary transitions to transform a material from one class to another.^{18,19,20} Electrons are classified as being either core electrons, which are always bound to the atomic nucleus, or valence electrons, which are sometimes bound to the nucleus and at other times are not, depending on the energy level of

Figure 1-2 Resistances in Composites; a) Intrinsic Resistance of Filler; b) Particle-Particle Contact Resistance; c) Tunneling Resistance

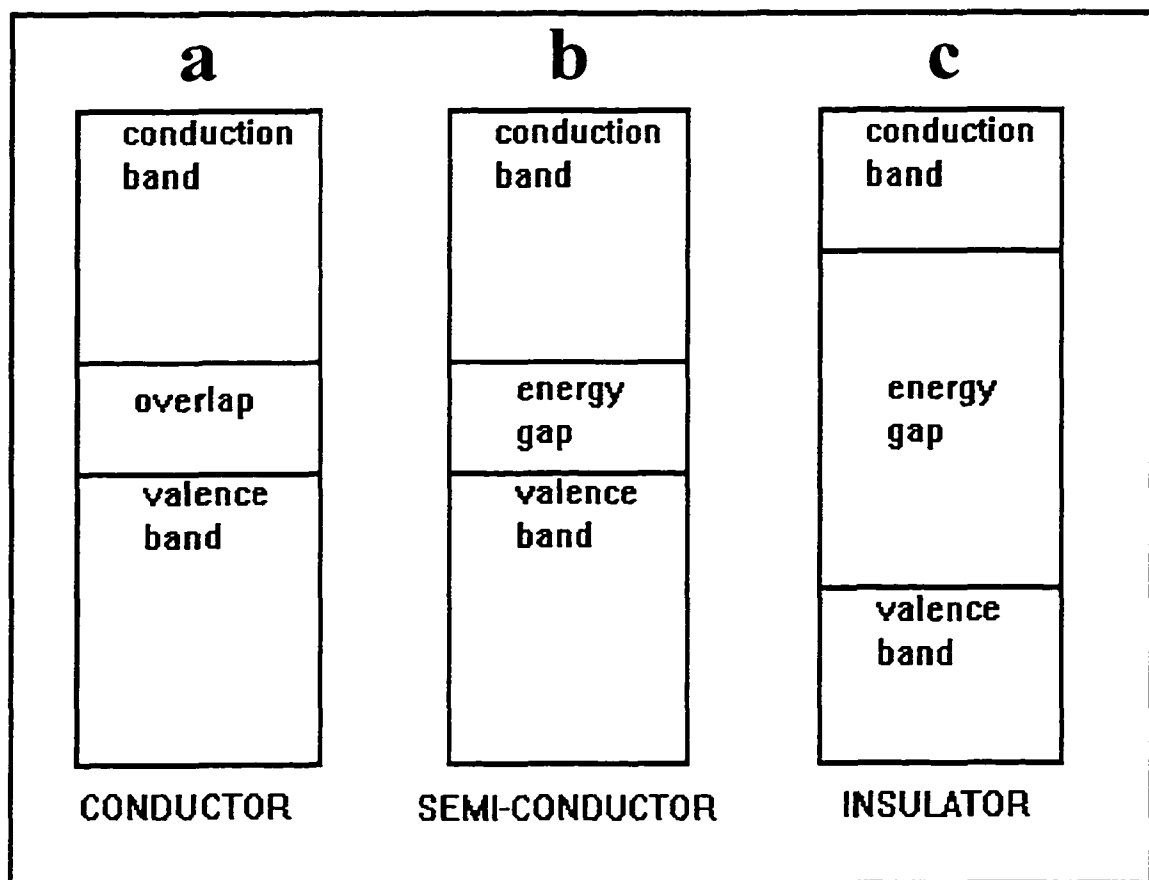


the atoms. As the molecular orbitals begin to hybridize, a valence band, where the electrons are tightly held by the atom to which they correspond when filled, and a conduction band, where the electrons are free to move throughout the material, form with an energy gap between the two bands. In order for conduction to occur, the electrons must be in the conduction band. The energy gap is the defining characteristic of metals, semi-conductors, and insulators. As shown in Figure 1-3(a), in electrical conductors the valence and conduction bands overlap due to the unfilled electron energy level, thus there is no energy gap and electrons from the unfilled energy can move freely throughout the material. This is a characteristic of all metals and is often referred to as metal-like conduction. Figure 1-3(b) shows the extremely small band gap indicative of a semi-conductor, which is easily overcome through photon absorption or temperature elevation. An insulator, schematically depicted in Figure 1-3(c), has such a large energy gap between the valence and conductive bands that electron transfer is prohibited.

1.2.1.2 Metals

Depending on the type of material used as the filler, the conduction mechanism of the filler particles will be very different. Metals, such as gold, silver, copper, and nickel, are often used as fillers and have conductivities on the order of 10^5 siemens per centimeter. In metals, the electrons in the valence band can be approximated as a free electron gas. In this approximation, the valence electrons of each atom in a lattice are free to move

Figure 1-3 Band Theory; a) Conductor; b) Semi-Conductor; c) Insulator



while the core electrons are tightly bound to the positively charged nucleus.²¹ This approximation is fairly accurate in metals because the volume of the core nucleus is small compared to the volume of the entire atom and because the core electrons shield the valence electrons from the ionic core. Equation 1-2 gives the conductivity for the free electron gas.

$$\sigma = \frac{n_e q^2 \tau}{m_e} \quad [1-2]$$

Where n_e is the electron density of the conduction electrons, q is the electron charge, m_e is the effective electron mass, and τ is the collision time, as defined by Equation 1-3, in terms of the electron mean free path (mfp) and the electron velocity (v_e).

$$\text{mfp} = v_e \tau \quad [1-3]$$

1.2.1.3 Organic Conductors

In the ground state, most organic materials are insulators because there are no partially filled energy levels and the gap between the valence and conduction bands is very large. The energy gap must be overcome in order for these intrinsically insulating materials to become conductors.²⁰ Two classes of conductive organic conductors, charge-transfer complexes (CTC) and electrically conducting polymers (CP) both use chemical modification (doping) of the molecular orbitals in order to eliminate the band gap.^{22,23} Doping consists of chemically treating the pi-orbitals with a charge transfer agent which is either an electron acceptor, close to the valence band energy level, or an electron

donor, close to the conduction band energy level.^{24,25,26} In organic conductors bands formed by atoms in close spatial proximity and similar crystallographic and electronic environments because of uniform pi-orbital orientation. This situation is realized in planer molecules with a network of conjugated double bonds, as depicted for both the CTC tetrathiafulvalene-tetracyanoquinodimethane (TTF-TCNQ) and the CP polypyrrole (PPy) in Figure 1-4(a) and 1-4(b), respectively, which have extensive overlap of the p_z -orbitals.² Equation 1-4 is used to describe conduction, and while often used for ionically conductive materials, also applies to electrically conductive organic conductors.¹⁹

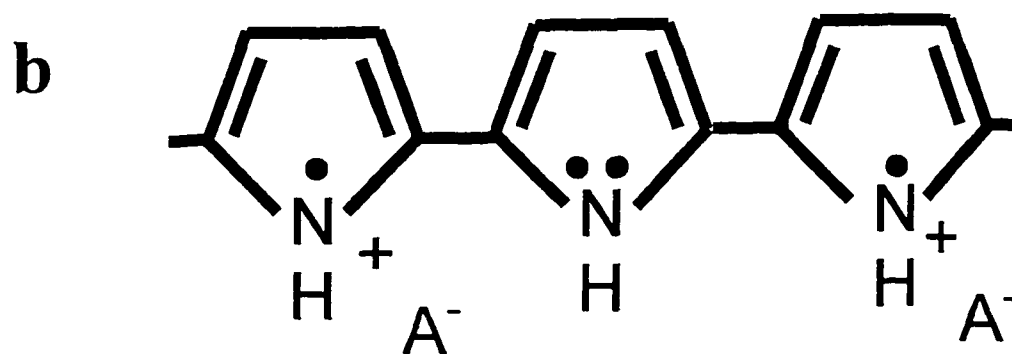
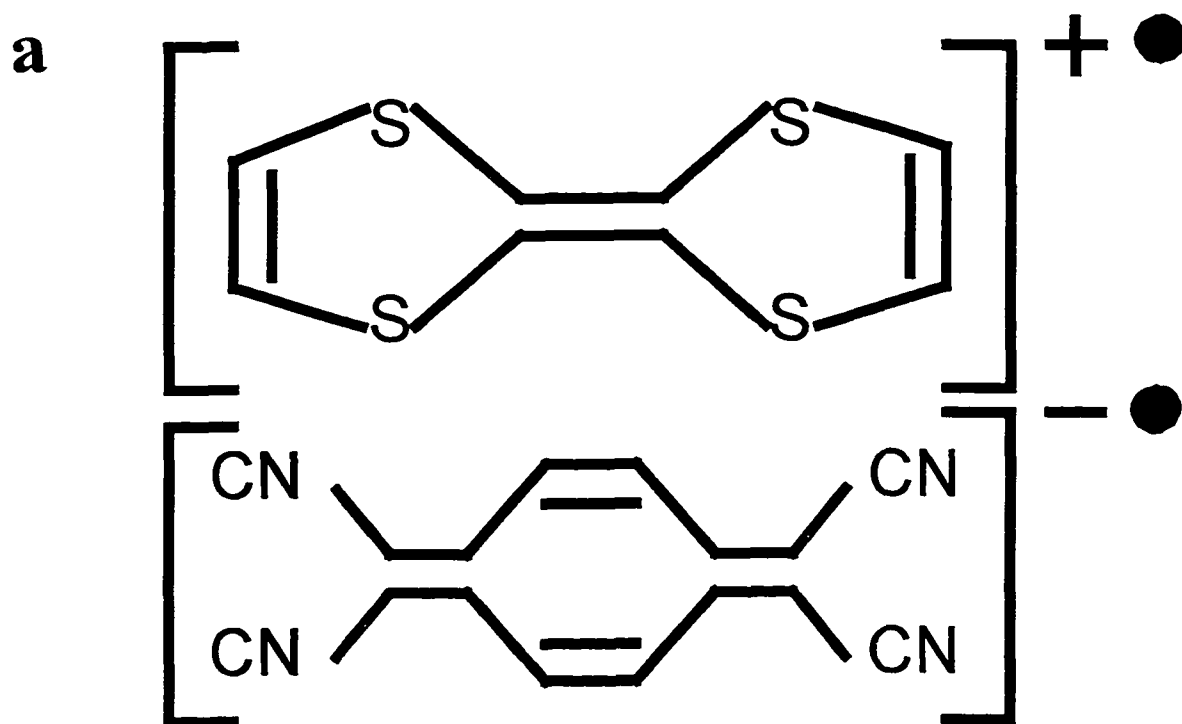
$$\sigma = q\eta\mu \quad [1-4]$$

Where q is the electron charge, η is the concentration of charge carriers, and μ is the transfer mobility. Mobility is an experimentally determined value.

1.2.1.4 Charge Transfer Complexes

Organic charge transfer complexes, such as TTF-TCNQ [Figure 1-4(a)], are used as fillers in reticulate doped polymer-matrix composites.²⁷ Many CT complexes form rod-shaped crystals and have an intrinsic conductivity of approximately 500 S/cm. Doping occurs as an organic free radical salt if formed from two organic molecules with overlapping p_z orbitals. The crystal structure of the resulting salt creates a conduction band, which allows electrons associated with the pi-bonds to conduct through this network of p_z orbitals, thus creating a quasi-1-dimensional synthetic metal.

Figure 1-4 Organic Conductors; a) Charge-Transfer Complex: tetrathiafulvalene-tetracyanoquinodimethane (TTF-TCNQ); b) Conductive Polymer: polypyrrole (PPy)



1.2.1.4 Electrically Conductive Polymers

An example of an electrically conducting polymer, polypyrrole, is shown in Figure 1-4(b). The addition of the dopant creates a polymeric or polyradical cation salt along the conjugated backbone of the polymer, thus allowing the conduction of the electrons associated with the p_z orbitals. Unlike metals and CTC, the electrical conductivity of CP can be controlled by the amount of charge transfer agent introduced, thus allowing the tuning of the conductivity from insulating to conducting.²⁸ The conductivity of CP's range from approximately 10^{-5} to 200 siemens per centimeter depending on the procedure for synthesis, doping, and film formation.

1.2.2 Particle-Particle Contact Resistance

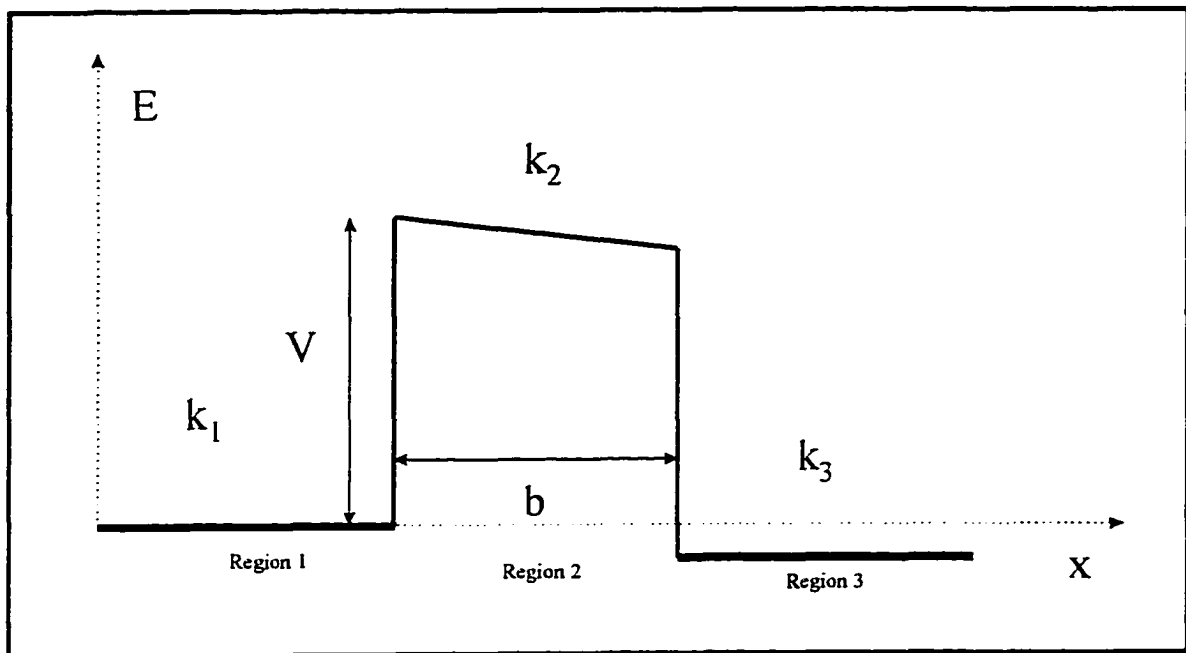
In polymer-matrix composites, the conductivity of the composite is several orders of magnitude lower than that of the conductive filler. Even if the conductive particles are contacting each other, there is still a particle-particle contact resistance due to electrons being forced through small contact areas. This particle-particle contact resistance (R_{cr}) is mathematically modeled by Equation 1-5.¹⁷

[1-5]

$$R_{cr} = \frac{\rho_0}{d}$$

Where ρ_0 is the resistivity of the filler and d is the contact area diameter. The contact resistance has experimentally been shown to be important for any system where the ratio of the diameter of the filler to the contact diameter is greater than ten.

Figure 1-5 Tunneling Potential Barrier



1.2.3 Tunneling Resistance

In systems with good polymer-filler adhesion, a thin polymer film coats the outside of the particles. Since the polymer is an insulator, the overall resistance is increased by the presence of this film. If the film thickness is less than 100 Å, conduction through quantum mechanical tunneling can occur. According to classical Newtonian physics, an electron in the conductive phase would not be able to penetrate the polymer-filler interface and conduction would stop. Wave - particle dualism explains why tunneling occurs: the polymer film creates a potential barrier between two conductive phases, but this barrier can be overcome if the wavelengths of the electrons are similar to the width of the potential barrier. Figure 1-5 shows schematically the potential barrier of the polymer film in tunneling, where E is the energy, x is the distance, b is the film thickness, k_w is the wave-vector, and H is the height of the barrier. The height of the barrier is related to the difference in energy of the conduction band of the polymer film and the Fermi energy of the conductive phase. If it is assumed that region 1 and region 3 in Figure 1-5 can be represented by the free electron model, then the current density (j) due to tunneling can be expressed by Equation 1-6.

$$j = \frac{2q}{h} \int f_1(E) [1 - f_3(E)] dE \int \frac{b^2 k_{\perp}}{(2\pi)^2} Z(E, k_{\perp}) dE \quad [1-6]$$

Where f_1 and f_3 represent the Fermi distribution functions for region 1 and region 3, respectively, and Z denotes the tunneling probability of electrons at a given energy. The

wave-vector k_{\perp} represents a vector made up of the components of the wave vector perpendicular to the tunneling current.

1.2.4 Temperature Dependence of Electrical Conductivity

Unlike homogeneous materials, the temperature dependence of conductivity for polymer-matrix composites is not a function of the discontinuous conductive phase.²⁹ Below the percolation threshold, as shown in Figure 1-6, the conductivity of the composite is nearly that of the polymer and the resistivity decreases exponentially with increasing temperature. Figure 1-7 shows the resistivity versus temperature profile for volume fractions greater than the percolation threshold. The resistivity initially increases with temperature due to the positive coefficient of expansion of the polymer. As the matrix expands the conductive particles move away from each other until the network has been ruptured, at which point the conductivity is again nearly that of the polymer-matrix, and at higher temperatures the resistivity decreases until the matrix either melts (thermoplastics) or degrades (thermosets). In both of these cases, it is the effect of temperature on the polymer-matrix that is responsible for the temperature dependence of the composite conductivity.

Figure 1-6 Temperature Dependence of Composite Resistivity in Iron Filled Styrene-Acrylonitrile Composite Below the Critical Volume Fraction ($V < V_c$) - This figure was adapted from reference 29

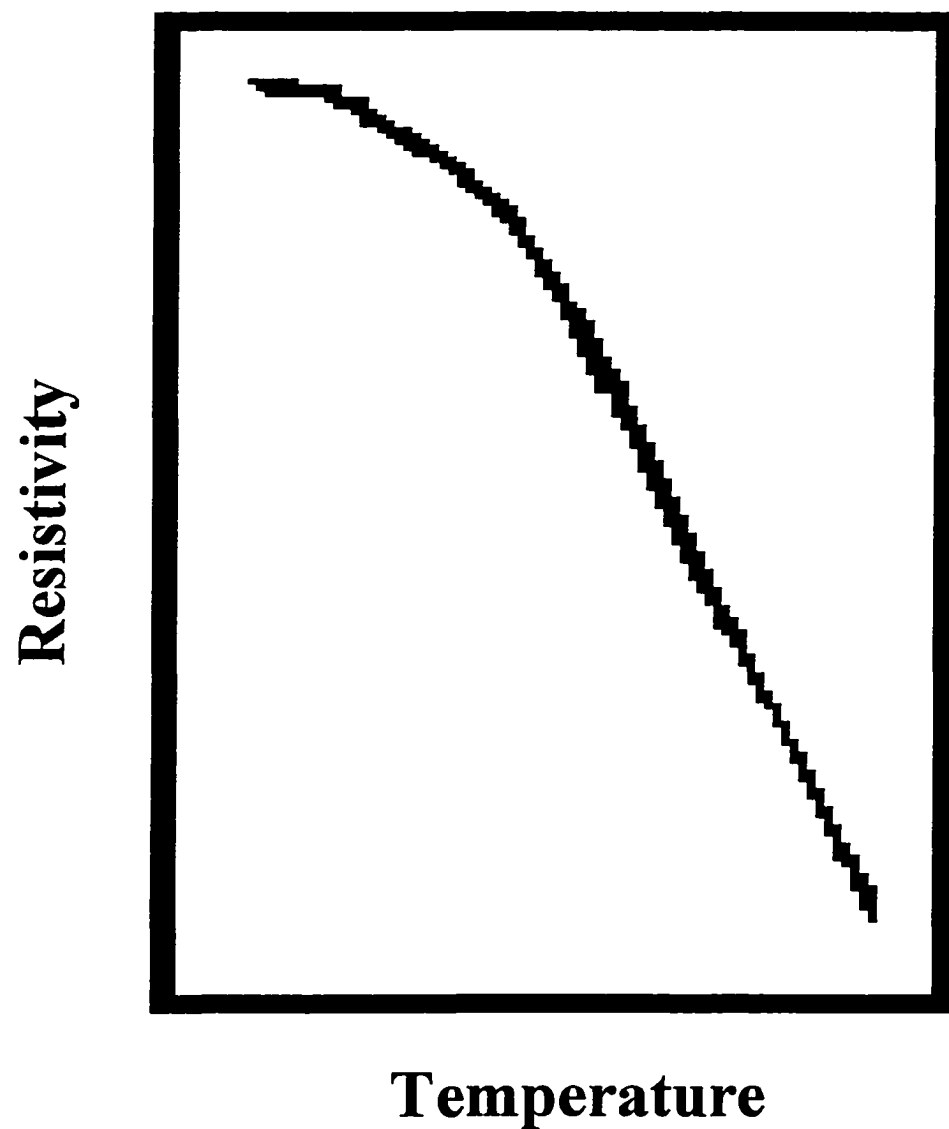
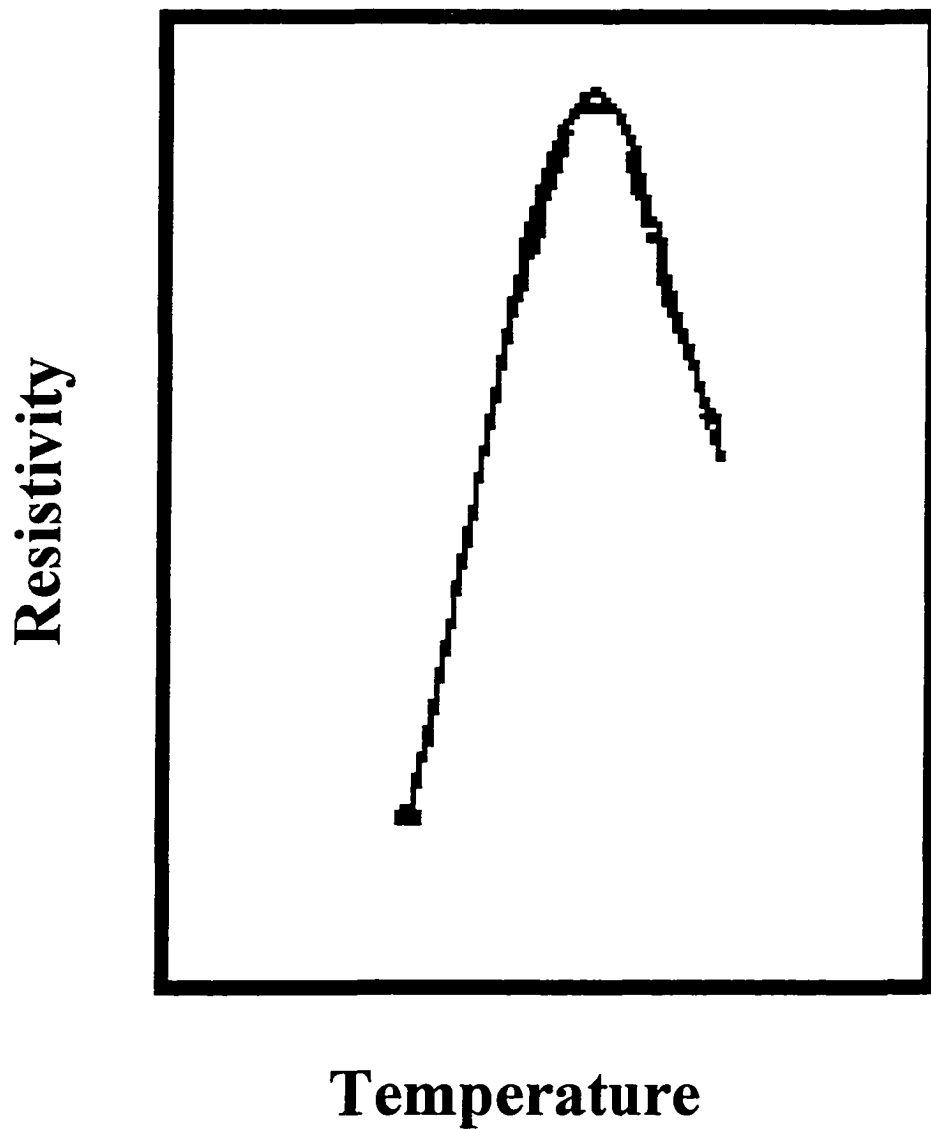


Figure 1-7 Temperature Dependence of Composite Resistivity in Iron Filled Styrene Acetonitrile Composites at a Concentration of 30% by Volume ($V > V_c$) - This figure was adapted from reference 29



1.3 PERCOLATION THEORY

As discussed in the introduction, percolation theory is used to model the conductivity of composite materials based on the critical volume fraction (V_c). Three approaches are taken in the literature; statistical, thermodynamic, and structure oriented percolation.⁹

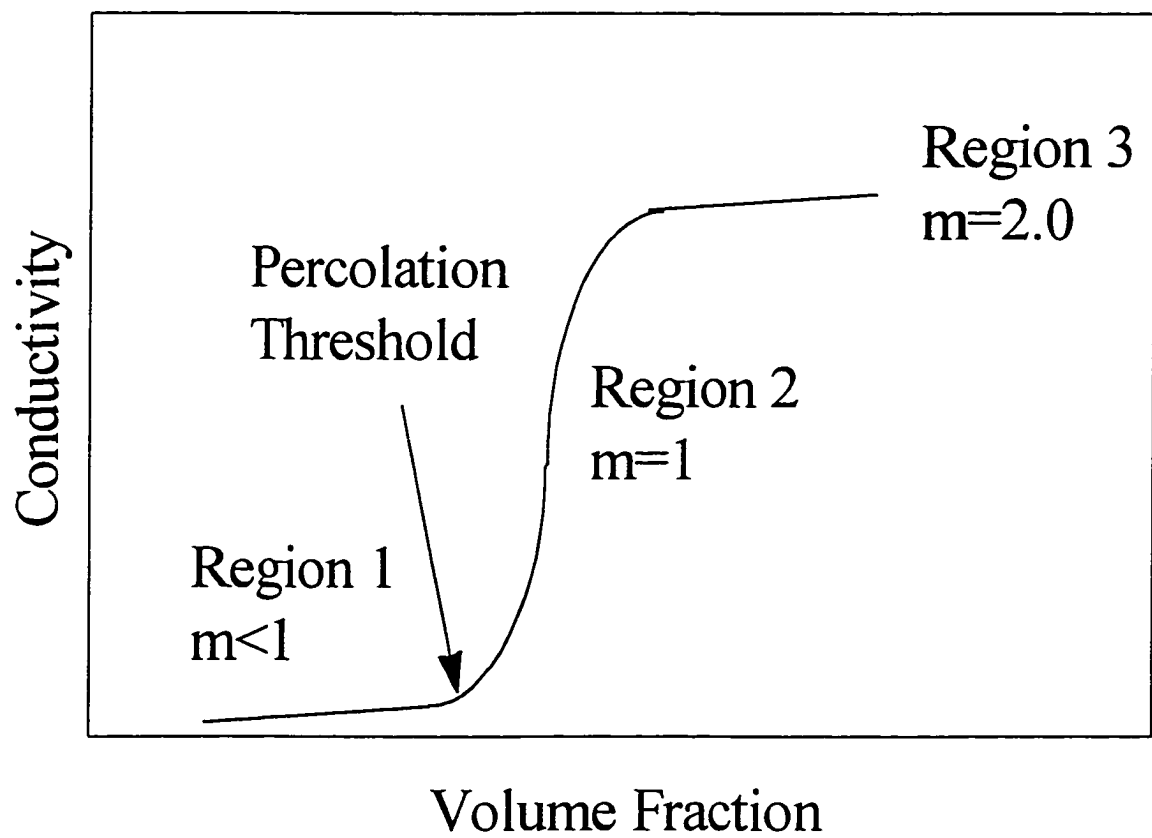
Statistical percolation focuses on the quantity of the filler and filler packing. In this approach, three distinct regions are defined as in Figure 1-8. Region I is where the volume fraction is less than V_c and the average number of contacts per particle, m , is less than one. The conductivity is almost constant with increasing filler content in this region. The second region called the critical region, starts at V_c and the conductivity increases rapidly with increasing volume fraction. At V_c , m is equal to one and hence the probability of forming an infinite chain becomes non-zero. According to a statistical percolation model, the conductivity, σ , in the critical region is given by a power-law relationship as shown in Equation 1-7.⁵

$$\sigma = \sigma_0 (V - V_c)^{t_{per}} \quad [1-7]$$

V is the volume fraction of the conductive filler, and t_{per} is the empirically determined power-law index, which typically ranges from 1.5 to 1.6. Finally, the critical region ends when m is equal to 2 and the conductivity becomes approximately constant once again.

While statistical percolation does give the correct shape of the conductivity curve, it does not explain the difference in conductivity for different polymer - filler systems at the

Figure 1-8 Statistical Percolation Model



same volume fraction. This led to the development of thermodynamic percolation models based on the overall interfacial free energy, the surface tensions, and the interactions between the filler and the polymer. The thermodynamic model was derived for mixing of the polymer and filler while the polymer is a melt. The model assumes the kinetics of the adsorption of the polymer melt on the particulate surface are equal to the adsorption process in low viscosity fluids. Below the critical volume fraction, the filler particles are distributed unevenly in flat agglomerates. As the concentration of filler is increased, compressive forces caused by the surface tensions of the polymer and filler force the agglomerates together. The interfacial energy of the particles will force the filler to form a three-dimensional network as the phases come to thermodynamic equilibrium. Lux has shown that even though this type of model does give a stronger theoretical basis for conductivity than statistical percolation models, the predictions do not match experimental results.³⁰

Mamunya et.al., recognizing that both the polymer and the filler affect conductivity, extended the statistical percolation theory of conduction to include a material factor that is a function of the volume fraction of filler to account for the interactions between the filler and the matrix.³¹ The expression for the material factor is given by Equation 1-8.

$$\begin{aligned}
 t_{\text{eff}} &= t_1 + t_2 \\
 t_2 &= t_1 s e^{u \log(\Phi)} \\
 \Phi &= \frac{(V - V_c)}{(V_m - V_c)}
 \end{aligned}
 \tag{1-8}$$

For most particle filled systems, $S=28V_c$, $t_1=1.7$, $u=0.35$, and V_m is defined as the filler packing density coefficient which is equal to the weight of the filler divided by the volume of the filler as determined by vibration compression. The final expression for the conductivity of the composite is given by Equation 1-9.

$$\sigma = \sigma_p + (\sigma_f - \sigma_p) \left[\Phi^{1.7(1+28V_c\Phi^{0.35})} \right] \quad [1-9]$$

Where σ_f and σ_p are the conductivity of the filler and matrix, respectively. This model is empirical and the parameters for each polymer - filler pair must be determined experimentally, thus limiting the predictive value. While it has been acknowledged that the morphology affects the conductivity of the composite material, little quantitative work has been done to show this dependence.

Theories and models based on statistical and thermodynamic percolation, while describing the shape of the conductivity curve, do not fully explain conduction in polymer composites. A structure - oriented percolation model of conduction has been proposed for ceramic - metal conductive composites using an effective medium approach.³² A theoretical network of spheres replaces the real conductive network, with some spheres having a conductive core and an insulating surface, while others have an insulating core and a conductive surface. The volume fraction of each type of sphere is determined through a core volume fraction. The spheres are randomly placed in a matrix forming conductive pathways. This model has been successful in predicting the behavior of randomly mixed composites where the microstructure is known.

Another type of structure oriented model is to use a fractal approach. Most percolation models tend to neglect the distribution of the filler particles in the polymer-matrix or try to treat the problem using Euclidean geometry. The particles inside the polymer-matrix are assumed to be randomly mixed, which leads to an inhomogeneous disordered medium. Zhang et. al. used fractal analysis to describe the conductivity of the composites.³³ The filler particles are assumed to form aggregates inside the polymer-matrix which are of a fractal dimension. The fractal dimension reflects the connectedness of the filler and is directly correlated to the probability of forming a continuous conductive network. The expression for conductivity is given by the Equation 1-10.

$$\begin{aligned}\sigma &= \sigma_c^g \sigma_s^{(1-g)} \\ \sigma_c &= V\sigma_f + (1 - V)\sigma_p \\ \frac{1}{\sigma_s} &= \frac{V}{\sigma_f} + \frac{(1 - V)}{\sigma_p}\end{aligned}\tag{1-10}$$

The distribution function (g), given by Equation 1-11, relates the probability of the filler forming a conductive network to the fractal exponent (L').

$$g = V^a L'\tag{1-11}$$

Where “a” is an experimentally determined material parameter. The fractal exponent can be determined from small-angle scattering experiments.

1.4 PROJECT OVERVIEW

Research reported to date on conductive composites has focused on the characterization of physical properties and filler dispersion. Studies on the effect of the filler concentration and particle geometry on the thermal, electrical, and mechanical properties are very common and many models have been proposed to describe the property changes of these systems. The morphology of the polymer also influences the percolation threshold because it partially dictates particulate dispersion. While many studies have looked at the influence of dispersion and segregation of the filler particles on physical properties, little work has been done on the influence of the particulates on polymer structure and morphology. The polymer-filler interface influences particle-particle contact and tunneling resistance, yet few studies exist on surface modification of particulates for conductive composites. This dissertation expands our understanding of the interaction between the matrix polymer and the filler in electrically conducting thermoplastic composites by addressing, in limited scope, the following questions:

- How does the presence of the filler affect the polymer?
- How does particulate surface modification change the properties of the composite material?

Chapter 3 and 4 address the effect of the filler on the matrix and Chapter 5 addresses how particulate surface modification changes the physical properties. Chapter 3 reports a wide-angle x-ray scattering (WAXS) study of TTF-TCNQ – low density polyethylene (LDPE) composites. The experiments investigated the effect of TTF-TCNQ on the

preferential orientation of the LDPE crystallites in uniaxially stretched composite films.

The effect of nickel in filled LDPE composites on the crystallization kinetics of the LDPE crystallites has been discussed in Chapter 4. Finally, a method for increasing conductivity in particulate-filled LDPE composites via surface modification of the filler is presented in Chapter 5.

1.5 NOTATION

σ	Electrical Conductivity
V	Volume Fraction
V_c	Percolation Threshold
t_{per}	Power Law Index
n_e	Electron Density
q	Electron Charge
m_e	Electron Mass
τ	Collision Time
mfp	Mean Free Path
η	Concentration of Charge Carriers
μ	Transfer Mobility
v_e	Electron Velocity
R_{cr}	Particle – Particle Contact Resistance
ρ_0	Intrinsic Resistivity of Filler
d	Contact Diameter
E	Energy
x	Distance
k_w, k_1, k_2	Wave Function
k_3, k_{\perp}	
b	Film Thickness

j	Current Density
f_1, f_2, f_3	Fermi Distribution Function
H	Height of the Tunneling Barrier
Z	Tunneling Probablilty
\hbar	Planks Constant
σ_0	Proportionality Constant
m	Number of Contacts Per Particle
t_{eff}	Effective Power Law Index
s	Mamunya's Constant
u	Mamunya's Exponential Factor
σ_f	Conductivity of Filler
σ_p	Conductivity of Polymer – Matrix
g	Distribution Function
a	Experimentally Determined Material Factor
L'	Fractal Exponent
V_m	Maximum Packing Fraction

1.6 REFERENCES

- 1 R.H. Norman, Conductive Rubbers and Plastics, Elsevier Publishing Company, New York, New York, 3, 1970.
- 2 R.A. Crossman, *Polym. Engr. Sci.*, **25**, 507 (1985).
- 3 F. Bueche, *J. of Appl. Phys.*, **44**, 532, (1973).
- 4 L.H. Sperling, Introduction to Physical Polymer Science, 2nd Edition, Wiley, New York, New York, 16, (1992).
- 5 J. Gurland, *Trans. Metallur. Soc. AIME*, **236**, 642, (1966).
- 6 J. Janzen, *Journal of Applied Physics*, **46**, 966 (1975).
- 7 S. Kirkpatrick, *Reviews of Modern Physics*, **45**, 574 (1973).
- 8 S.M. Aharoni, *Journal of Applied Physics*, **43**, 2463 (1972).
- 9 F. Lux, *Journal of Material Science*, **28**, 285 (1993).
- 10 E.P. Mamunya, V.V. Davidenko, and E.V. Lebedev, *Polymer Composites*, **16**, 319 (1995).
- 11 Janzen, J., *Journal of Applied Physics*, **46**, 966, (1975).
- 12 Bigg, D.M., *Journal of Rheology*, **28**, 501, (1994).
- 13 F. Gubbles, S. Blacher, Vanlathem E., R. Jerome, R. Deltour, F. Brouers, and P.H. Teyssie *Macromolecules*, **28**, 1559, (1995).
- 14 A. Malliaris, and D. T. Turner, *J. Appl. Phys.*, **42**, 614, (1971).
- 15 D. M. Bigg, *J. Rheol.*, **25**, 501, (1984).

- 16 T. Yamamoto, E. Kubota, A. Taniguchi, S. Dev, K. Tanaka, K. Osakada, *Chem. Mater.*, **4**, 570, (1992).
- 17 R. G. Ruschau, S. Yoshikawa, and R. E. Newnham, *J. Appl. Phys.*, **72**, 953, (1992).
- 18 T. J. Marks, *Angew. Chem. Int. Ed. Engl.*, **29**, 857, (1990).
- 19 A. R. Blythe, Electrical Properties of Polymers, Cambridge University Press, Cambridge, MA, 90-98, (1979).
- 20 M. Aldissi, Inherently Conducting Polymers, Noyes Data Corporation, Park ridge, NJ, 37-40, (1989).
- 21 C. Kittel, Introduction to Solid State Physics, 7th Edition, Wiley, New York, New York, 156, (1996).
- 22 H. Narmann, in Electronic Properties of Polymers, H. Kuzmany, and M. Mehring, editors, Springer-Verlag, NY, 3, (1992).
- 23 T. Thakur, *Macromolecules*, **21**, 661, (1988).
- 24 B. Wessling, in Electronic Properties of Polymers, H. Kuzmany, and M. Mehring, editors, Springer-Verlag, NY, 487, (1992).
- 25 H. S. Nalwa, *Polymer*, **32**, 802, (1991).
- 26 C. M. Jenden, R. G. Davidson, and T. G. Turner, *Polymer*, **34**, 1649, (1993).
- 27 Ferrao, J.R., and Williams, J.M., Introduction to Synthetic Electrical Conductors, Academic Press, Inc., New York, New York, 9, (1987).

- 28 C. W. Chien, in Macromolecules, H. Beniot, and P. Rempp, editors, Pergamon Press, Elmsford, NY, 233, (1982).
- 29 L. Nicodemo, L. Nicolais, G. Romero, and E Scafora, *Polym. Eng. Sci.*, **18**, 293, (1978).
- 30 F. Lux, *Polym. Engr. Sci.*, **33**, 334, (1993).
- 31 E.P. Mamunya, V.V. Davidenko, and E.V. Lebedev, *Polym. Compos.*, **16**, 319, (1995).
- 32 K. Yoshida, *J. Phys. Soc. Jap.*, **59**, 4087,(1990).
- 33 M. Q. Zhang, J. R. Xu, H. M. Zeng, Q. Huo, Z. Y. Zhang, F. C. Yun, and K. Friedrich, *J. Mater. Sci.*, **30**, 4226, (1995).

CHAPTER 2

EXPERIMENTAL PROCEDURES

2.1 INTRODUCTION

The work described in this dissertation characterized the effects of filler concentration, processing, and filler surface modification on the properties of electrically conducting low density polyethylene (LDPE) composites. This chapter systematically describes the procedures used for preparation of composite films, morphological experiments, and physical property evaluation.

2.2 COMPOSITE FILM PREPARATION

2.2.1 Solution Casting

LDPE was dissolved in decalin, xylene, or chlorobenzene at 110°C. The filler was added and the mixture was allowed to reheat to 110°C. After re-heating, the mixture was stirred for 2 minutes and cast onto a 70°C mercury surface. LDPE quickly formed a gel, which did not allow the filler particles, even very dense nickel particles, to settle from solution. The composite dried under a chemical hood for 48 hr. The composite film was removed from the mercury surface and allowed to dry for another 48 hr at

25°C under the hood. Residual solvent was then removed by placing the sample in a vacuum oven at 70°C for an additional 48 hr. The film thickness was measured using a micrometer and varied from 0.6 to 0.9 mm.

2.2.2 Powder Mixing

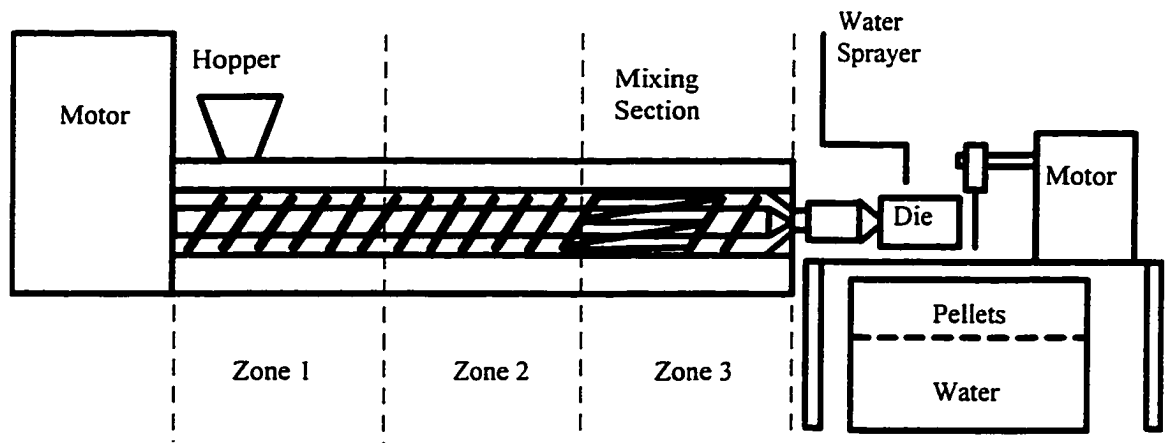
Composite films were produced by manually powder mixing the components for 5 minutes in a sealed container. The mixed powder was then compression molded into a 1¼ inch diameter pellet using a mold temperature of 120°C and mold pressure of 5000 psi. The pellet was then placed in a platen press, heated to 120°C, then compressed to the desired thickness of approximately 1 millimeter.

2.2.3 Extrusion

A Killion KL-100 Extruder single-screw extruder with one part of the screw having a back mixing section was used to produce the composite films. The temperatures of three zones were 150°C, 150°C, 160°C back to front and the die head temperature was 120°C. In order to achieve uniform mixing, the material was passed through the extruder 3 times. During the first two passes the extrudate was sent through a pelletizer (Figure 2-1(a)). On the third pass, a water-cooled calendaring system was used, as depicted in Figure 2-1(b).

Figure 2-1 Extrusion Processing; a) Pelletizer; b) Calendaring

a



b

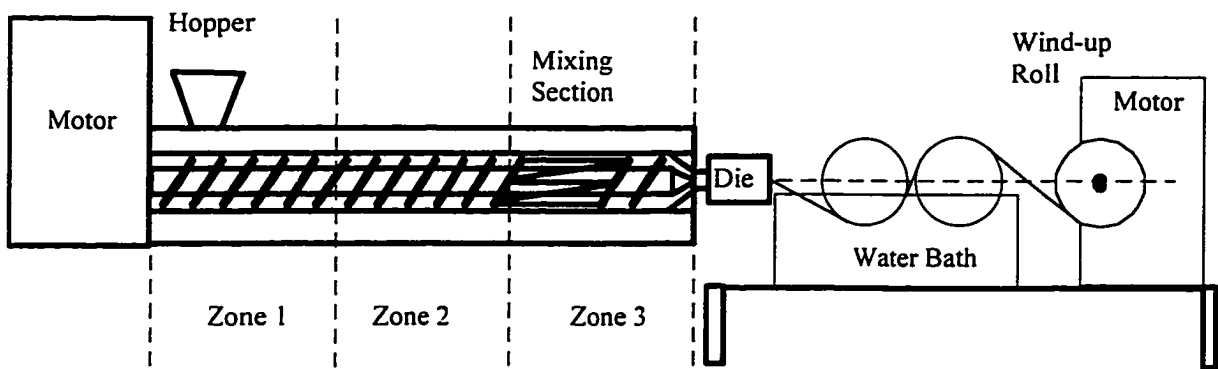
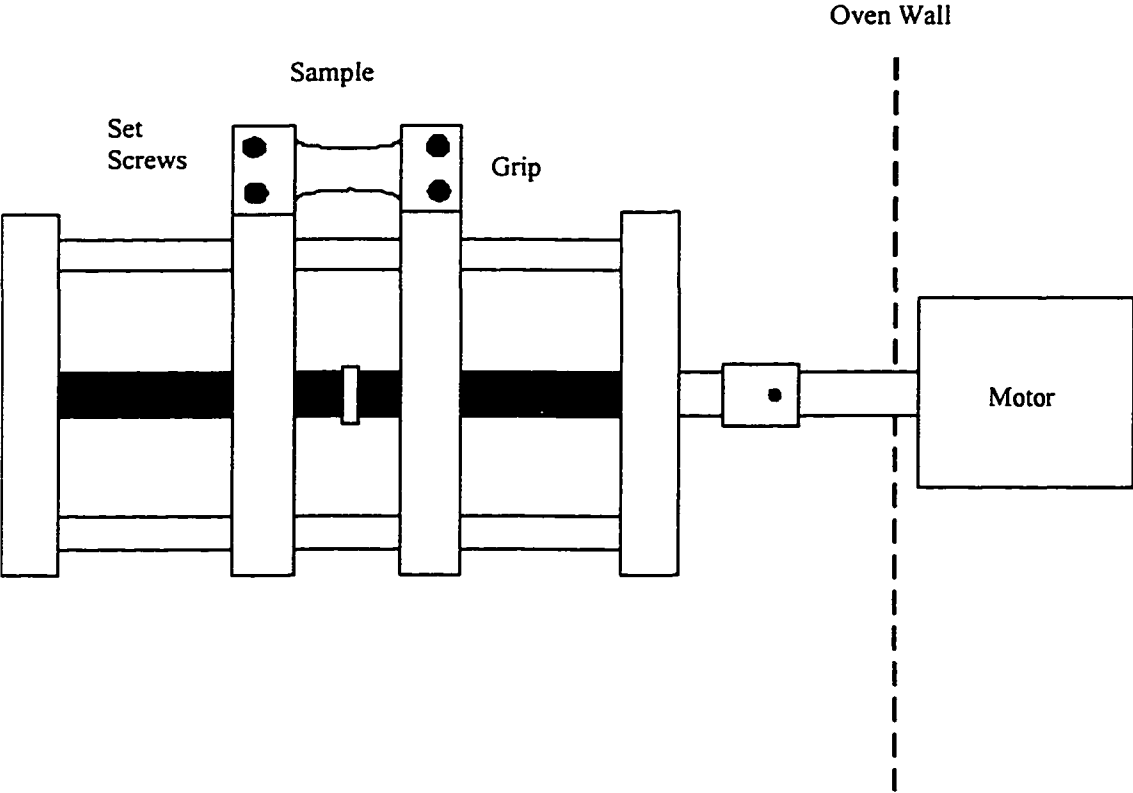


Figure 2-2 Stretcher



2.2.4 Uniaxial Orientation

A motor driven stretching apparatus built at The University of Oklahoma was used to uniaxially orient solution-cast samples parallel to the casting surface. Brittle failure of the highly filled samples was overcome by heating all samples to approximately 80°C before stretching. The samples were cooled under stress to room temperature by forced air.

2.3 MORPHOLOGICAL STUDIES

2.3.1 Orientation Characterization through Wide Angle X-Ray Scattering (WAXS)

Orientation was measured as a function of draw ratio by wide angle x-ray scattering (WAXS). When an x-ray beam is diffracted by a polymer, rings of diffracted x-ray intensity form, which correspond to the d-spacing of a specific crystallographic plane (i.e. correspond to a specific diffraction angle). In unoriented materials, the crystal planes are randomly distributed in space and there is no change in intensity with azimuthal angle, χ , as in Figure 2-3(a). However, if the crystallographic planes are preferentially oriented, then maximums in intensity with χ are observed (Figure 2-3(b)). By measuring the x-ray intensity as a function of the azimuthal angle at a constant scattering angle (a specific d-spacing or intensity ring), a quantitative assessment of the polymer chain orientation can be made.

Full characterization of the reticulate doped composites required measurements at different filler concentrations, different draw ratios, and two different scattering angles

Figure 2-3 WAXS Patterns; a) Unoriented Samples; b) Oriented Samples

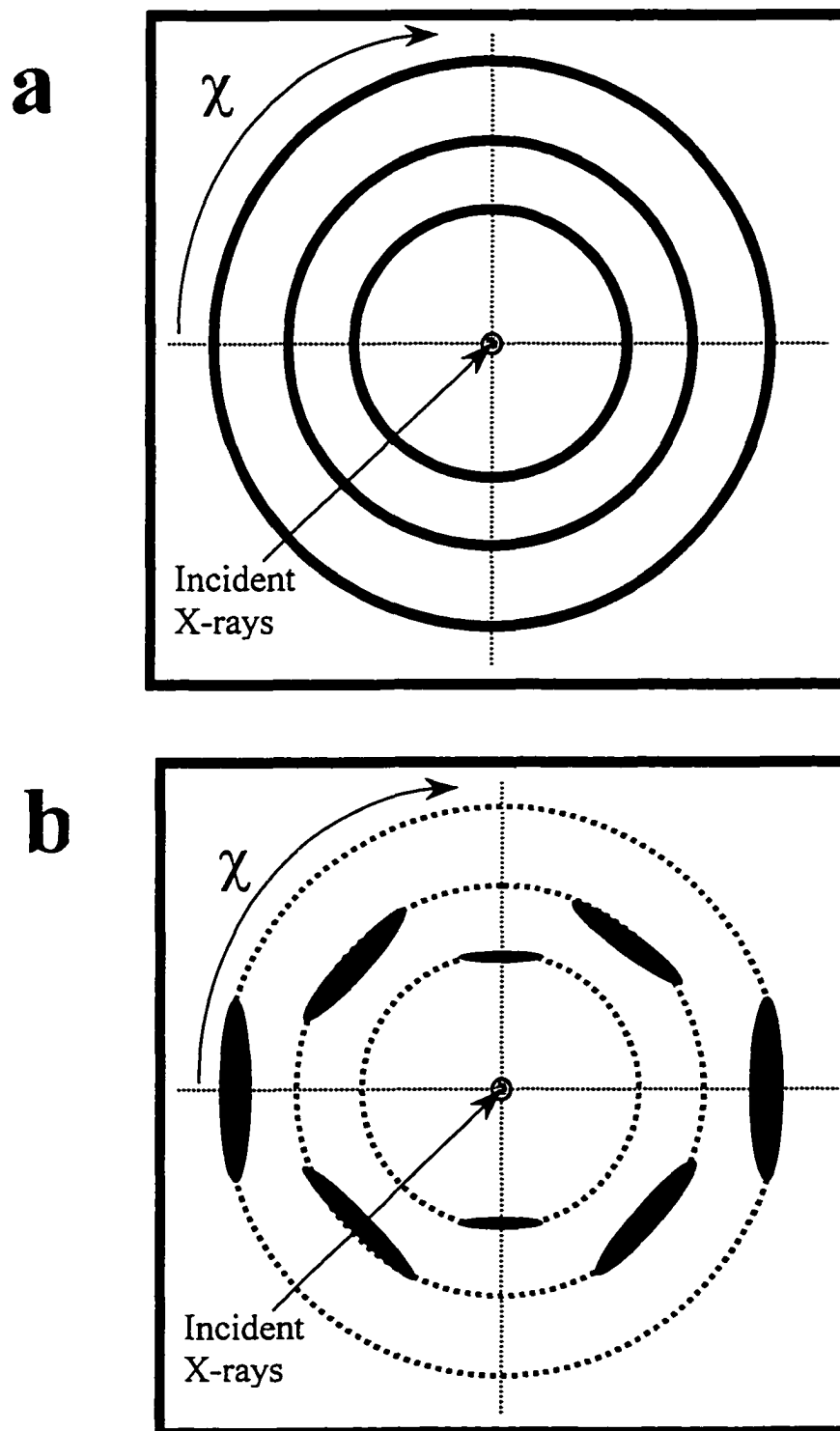
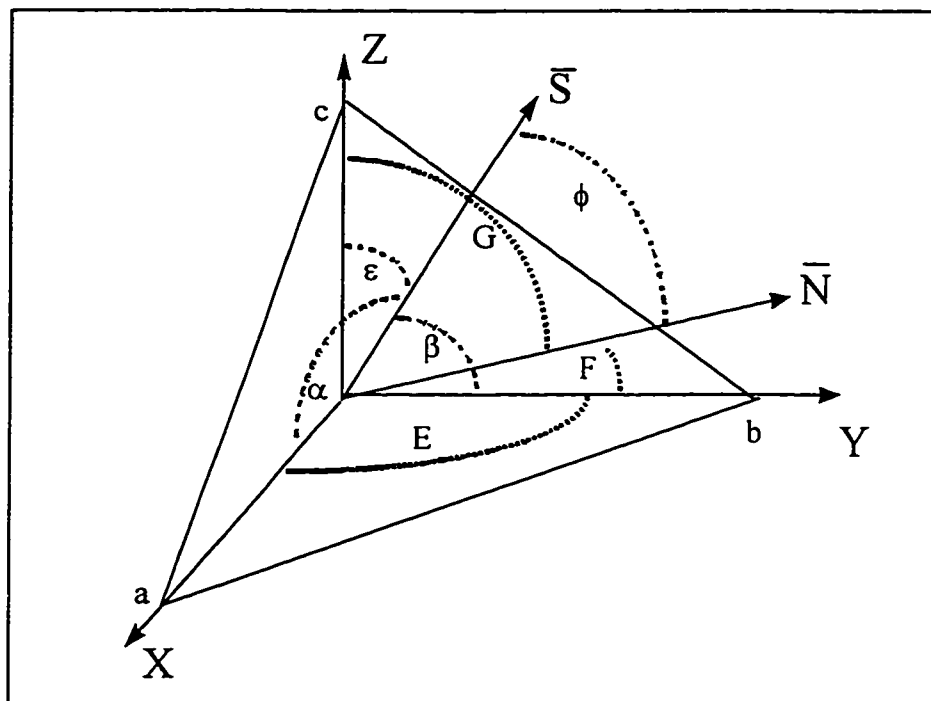
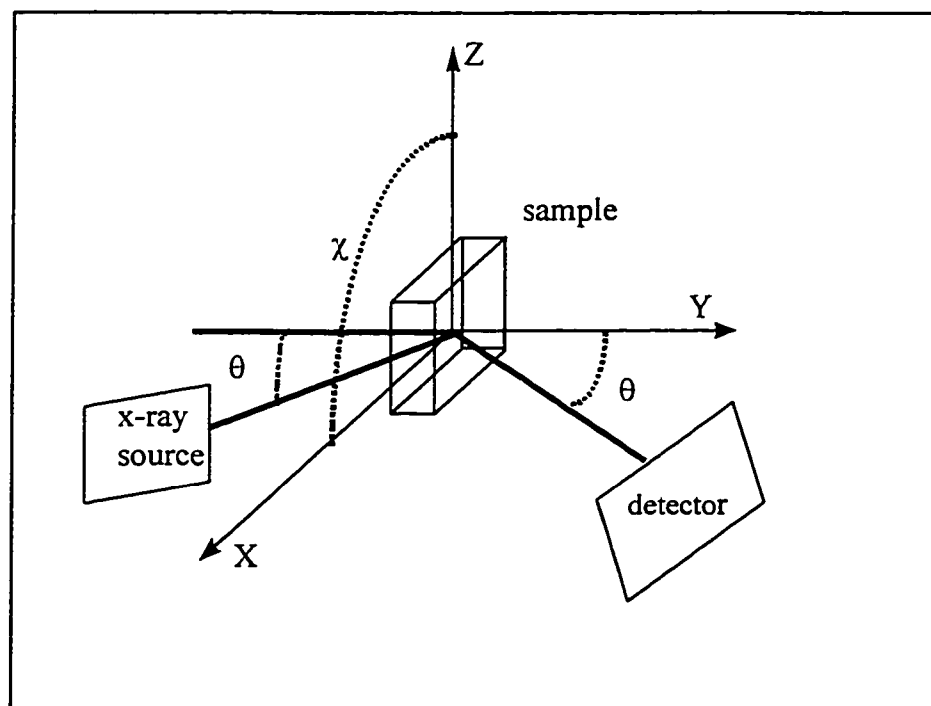


Figure 2-4 a) WAXS Coordination System; b) WAXS Experimental Geometry

a



b



(2Θ). By carrying out these studies at Stanford Synchrotron Radiation Laboratory (SSRL), high photon flux synchrotron radiation allowed characterization to be performed quickly. The WAXS measurements were obtained using the coordination system defined in Figure 2-4(a). The Z axis is defined as the crystalline chain axis (the c-axis) and the angles α , β , and ϵ are the angles between the stretching direction, \underline{S} , and the X, Y, and Z axes, respectively.¹ In Figure 2-4(a), the points a, b, and c form a crystalline reflection plane that has a unit vector, \underline{N} , normal to the plane surface. The angle of orientation (ϕ) is the angle between \underline{N} and a unit vector, \underline{S} , in the stretching direction.

$$\underline{S} = \cos(\alpha) \bar{i} + \cos(\beta) \bar{j} + \cos(\epsilon) \bar{k} \quad [2-1]$$

$$\begin{aligned} \underline{N} &= \cos(E) \bar{i} + \cos(F) \bar{j} + \cos(G) \bar{k} \\ \underline{N} &= e \bar{i} + f \bar{j} + g \bar{k} \end{aligned} \quad [2-2]$$

The coefficients of \underline{N} are denoted e, f, and g to simplify the expressions below and are determined from the reflection plane [hkl] and the crystal structure. The angle ϕ is given by Equation 2-3.

$$\cos(\phi) = \underline{N} \bullet \underline{S} = e \cos(\alpha) + f \cos(\beta) + g \cos(\epsilon) \quad [2-3]$$

Squaring and averaging Equation 2-3 gives Equation 2-4.

$$\begin{aligned} \langle \cos^2(\phi) \rangle &= e^2 \langle \cos^2(\alpha) \rangle + f^2 \langle \cos^2(\beta) \rangle + \\ &g^2 \langle \cos^2(\epsilon) \rangle + 2ef \langle \cos(\alpha) \cos(\beta) \rangle \\ &+ 2fg \langle \cos(\beta) \cos(\epsilon) \rangle + 2eg \langle \cos(\alpha) \cos(\epsilon) \rangle \end{aligned} \quad [2-4]$$

To determine the average value of $\langle \cos^2(\phi) \rangle$ experimentally, the scattered intensity at a given 2θ was averaged over the azimuthal angle (χ), given by Equation 2-5.

$$\langle \cos^2(\phi) \rangle = \cos^2(\theta) \langle \cos^2(\chi) \rangle \quad [2-5]$$

As shown in Figure 2-2(b), the sample was rotated in the azimuthal direction with the detector fixed at an angle 2θ to determine $\langle \cos^2(\phi) \rangle$ according to the expression above.

The second term on the right side of Equation 2-5 was determined from Equation 2-6.

$$\langle \cos^2(\chi) \rangle = \frac{\int_0^{\pi/2} I(\chi) \cos^2(\chi) \sin(\chi) d\chi}{\int_0^{\pi/2} I(\chi) \sin(\chi) d\chi} \quad [2-6]$$

where I is the intensity of the scattered x-rays. In practice, the integrals were replaced by sums as shown in Equation 2-7.²

$$\langle \cos^2(\chi) \rangle = \frac{\sum_0^{\pi/2} I(\chi) \cos^2(\chi) \sin(\chi)}{\sum_0^{\pi/2} I(\chi) \sin(\chi)} \quad [2-7]$$

Equation 2-4 has a total of six unknowns, hence without further simplifications, at least five crystal planes would be required to determine the orientation functions in each direction. The orthogonality of the system provides the sixth equation.

$$\cos^2(\alpha) + \cos^2(\beta) + \cos^2(\epsilon) = 1 \quad [2-8]$$

The angles α , β , and ϵ are evaluated from Equation 2-4. If the pure axial crystal plane reflections can be obtained then only three planes need to be studied and Equation 5 simplifies as shown in Equation 2-9.

$$\begin{aligned} \langle \cos^2(\phi_{h00}) \rangle &= \cos^2(\alpha) \\ \langle \cos^2(\phi_{0k0}) \rangle &= \cos^2(\beta) \\ \langle \cos^2(\phi_{00l}) \rangle &= \cos^2(\epsilon) \end{aligned} \quad [2-9]$$

Another simplification can be made for particular crystal structures allowing fewer than five reflection planes to be required. Because PE has an orthorhombic crystal structure the cross product terms in Equation 2-4 are zero as shown in Equation 2-10 and only two reflection planes were required for characterization.

$$\begin{aligned} \langle \cos^2(\phi) \rangle &= e^2 \langle \cos^2(\alpha) \rangle + \\ &+ f^2 \langle \cos^2(\beta) \rangle + g^2 \langle \cos^2(\epsilon) \rangle \end{aligned} \quad [2-10]$$

PE [110] and [200] reflection planes, at 21.4° and 23.7°, respectively, were used for characterization of the crystalline orientation.^{3,4} The values of e , f , and g for the [110] reflection plane are 0.554, 0.832, and 0, while those of [200] are 1, 0, and 0, respectively.

The orientation of the composite films was quantitatively characterized as $\cos^2(\epsilon)$, where ϵ is the angle between the stretching direction, \underline{S} , and the polymer chain axis, shown as the \underline{Z} axis in Figure 2-7(a). The value of $\cos^2(\epsilon)$ can be between 0 and 1. If the orientation of the chain axis is perpendicular to the stretching direction, then $\cos^2(\epsilon)$

is 0. If the chain axis is parallel to the stretching direction, then $\cos^2(\epsilon)$ is 1. When the chain axis is randomly distributed, then $\cos^2(\epsilon)$ is 1/3.

2.3.2 Optical Microscopy

A Nikon Optical Microscope at a magnification of 800X was used to observe the large-scale structure of fillers in composites.

2.3.3 Atomic Force Microscopy (AFM) and Scanning Tunneling Microscopy (STM)

AFM and STM was done using a Multimode NanoScope III SPM (Digital Instruments). STM was done in both standard height mode and current imaging tunneling spectroscopy (CITS) mode with mechanically cut Pt-Ir tips. A CITS image is a collection of scanning tunneling spectroscopy (STS) plots that correspond to a data point in an STM image. An STS curve is a plot of the tunneling current at a specific surface position obtained as a function of the bias voltage applied to the sample at a fixed separation from the scanning tip. CITS reveals the conductivity distribution in the scanned area. Samples of both the nickel and PPy coated nickel were prepared by evenly pressing a small amount of flake on a thick layer of Parafilm®. A conducting path between the flakes and the bottom steel sample holder was constructed with silver glue. This sandwich structure (flakes - parafilm - steel disc) ensured the images obtained were only a function of the surface morphology of the flakes.

2.3.4 Scanning Electron Microscopy

Images were obtained from The University of Oklahoma Electron Microscopy Laboratory using an ETEC Autoscan SEM with GW Type 113 back scatter. The images were taken at a magnification of 300X. Samples were prepared by cutting a thin slice from the cross section of the composite films with a Stanley Blade®.

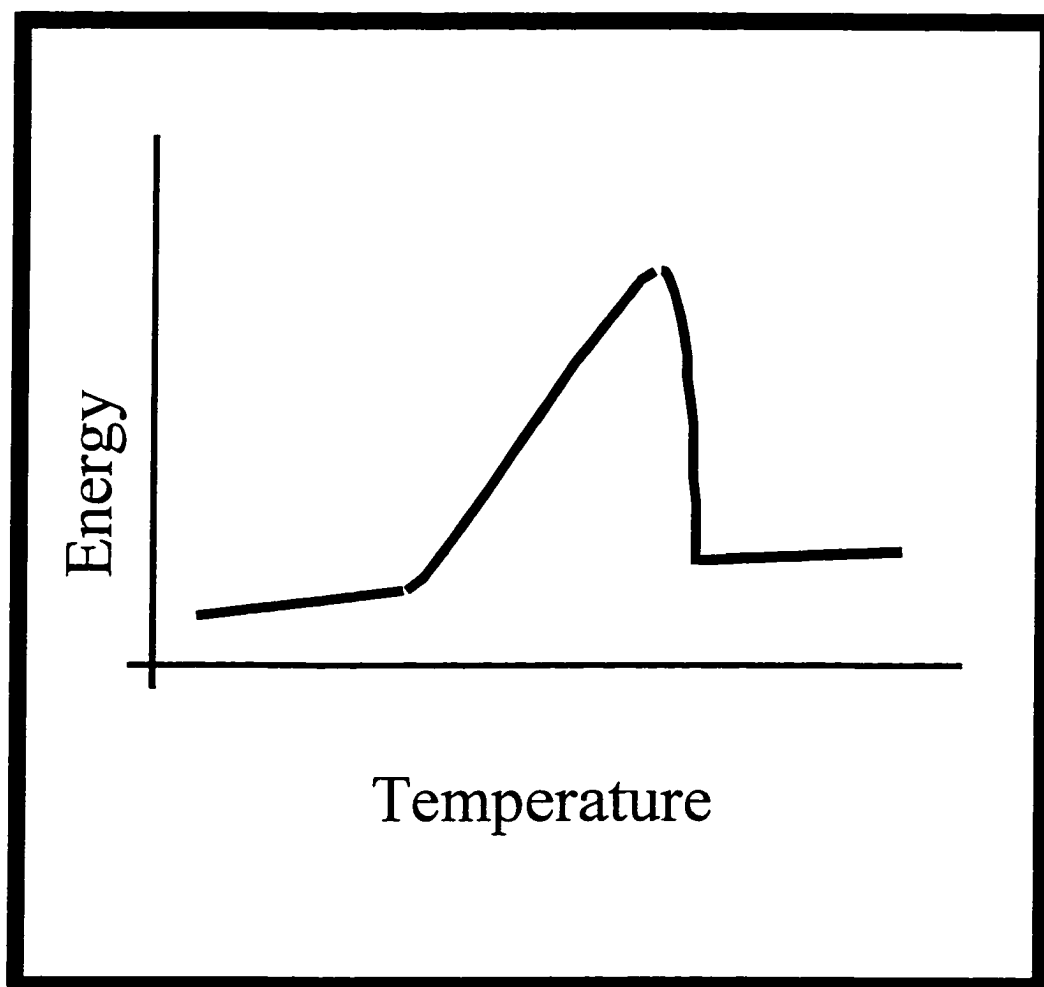
2.3.5 Fractional Crystallinity

The crystallinity was determined by differential scanning calorimetry measurements using a Perkin-Elmer DSC II calorimeter at a scanning rate of 10° per minute and a computerized data acquisition system designed at the University of Oklahoma. Appendix B is the procedure used to calibrate the DSC-II using the computerized data acquisition system. The heat of melting (ΔH_f) for a sample of known polymer mass and a purely crystalline polymer (ΔH_f^0) indicated crystallinity (χ) by Equation 2-11.⁵

$$X = \frac{\Delta H_f}{\Delta H_f^0} \quad [2-11]$$

Heat of melting for a sample, shown schematically in Figure 2-5, was determined experimentally by integrating the baseline subtracted DSC output over the temperature range in which the sample melts.⁶ The literature value of the heat of melting for pure crystalline LDPE, ΔH_f^0 , was assumed to be 282 J/g.⁷

Figure 2-5 Schematic Diagram of DSC Melting Curve



2.4 ISOTHERMAL CRYSTALLIZATION

Isothermal crystallization experiments were conducted using a Perkin-Elmer DSC II differential scanning calorimeter with a computerized data acquisition system developed at the University of Oklahoma. The sample was heated to 117°C and held at that temperature for 5 minutes to ensure complete melting. The sample was then quickly cooled at a rate of 320°/minute to a specific isothermal crystallization temperature (Figure 2-6(a)). In order to isolate heat evolution due to crystallization from that of sample cooling, for each isothermal crystallization temperature a companion cooling curve was measured as shown in Figure 2-6(b). The difference between the upper and lower temperature for the companion cooling curve was the same as the difference between 117°C and the isothermal crystallization temperature, and the lower temperature for the companion cooling curve was 117°C. The companion cooling curve was then subtracted from the isothermal crystallization curve giving the result shown in Figure 2-6(c). Prior to subtraction, the companion-cooling curve was adjusted for the difference in composite heat capacity, C_{PC} , as shown by Equations 2-12 and 2-13:⁸

$$C_{PE} = 1.98 + 3.70 \times 10^{-3} T \quad [2-12]$$

$$C_{pc} = C_{PE} (1 - w) + wC_N \quad [2-13]$$

where the temperature, T , is in °C, w is the weight fraction, and C_{PE} is the heat capacity for LDPE. The heat capacity for nickel, C_N , was assumed to be 0.456 J/g°C.⁹ The crystallinity as a function of time for a sample of known polymer mass, m_p , was determined by Equation 2-14, and shown for LDPE at 100°C in Figure 2-7.¹⁰

Figure 2-6 DSC Output for LDPE at 100°C; a) Raw Data; b) Cooling Curve; c) Corrected Data with Features Due Totally to Crystallization

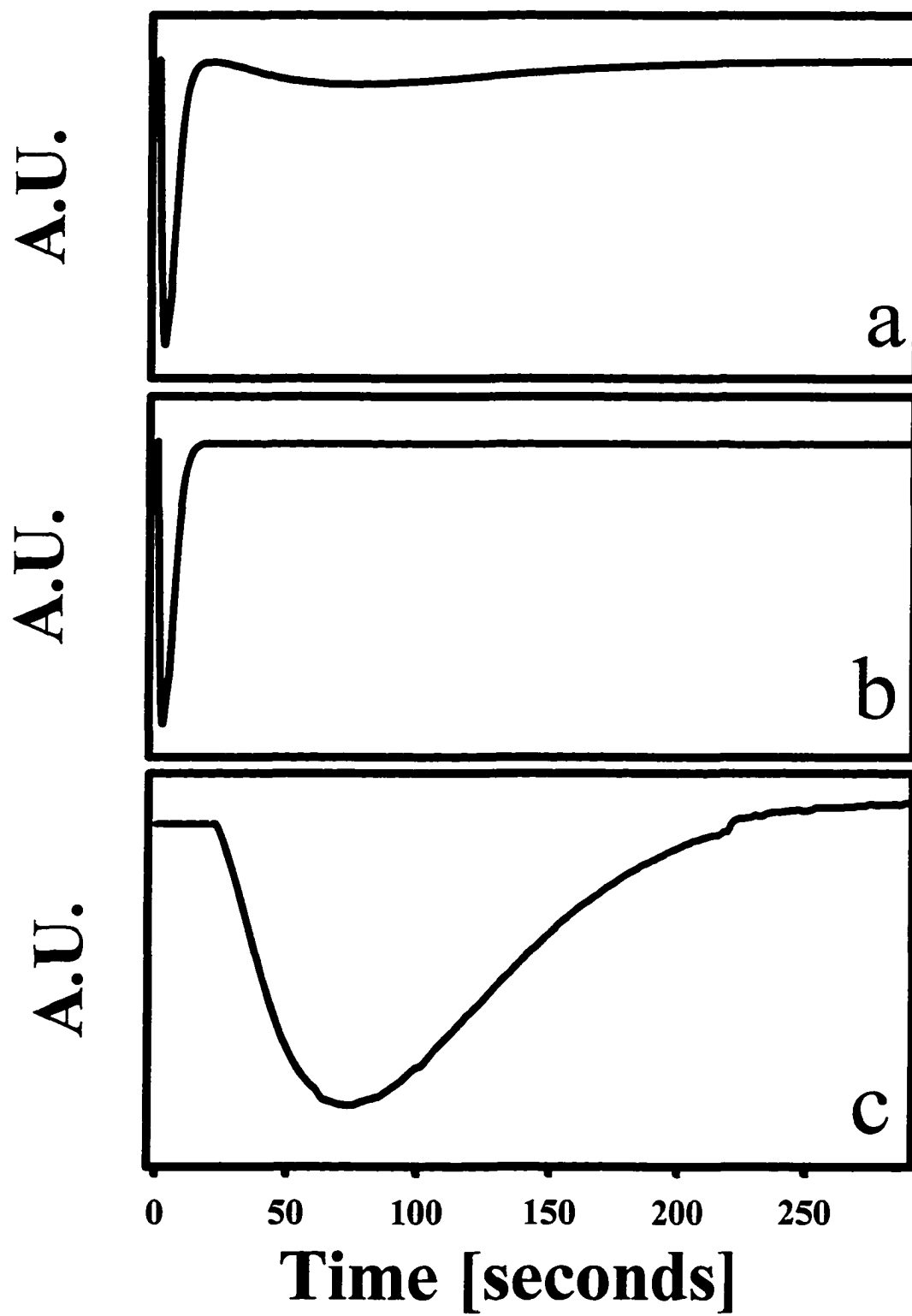
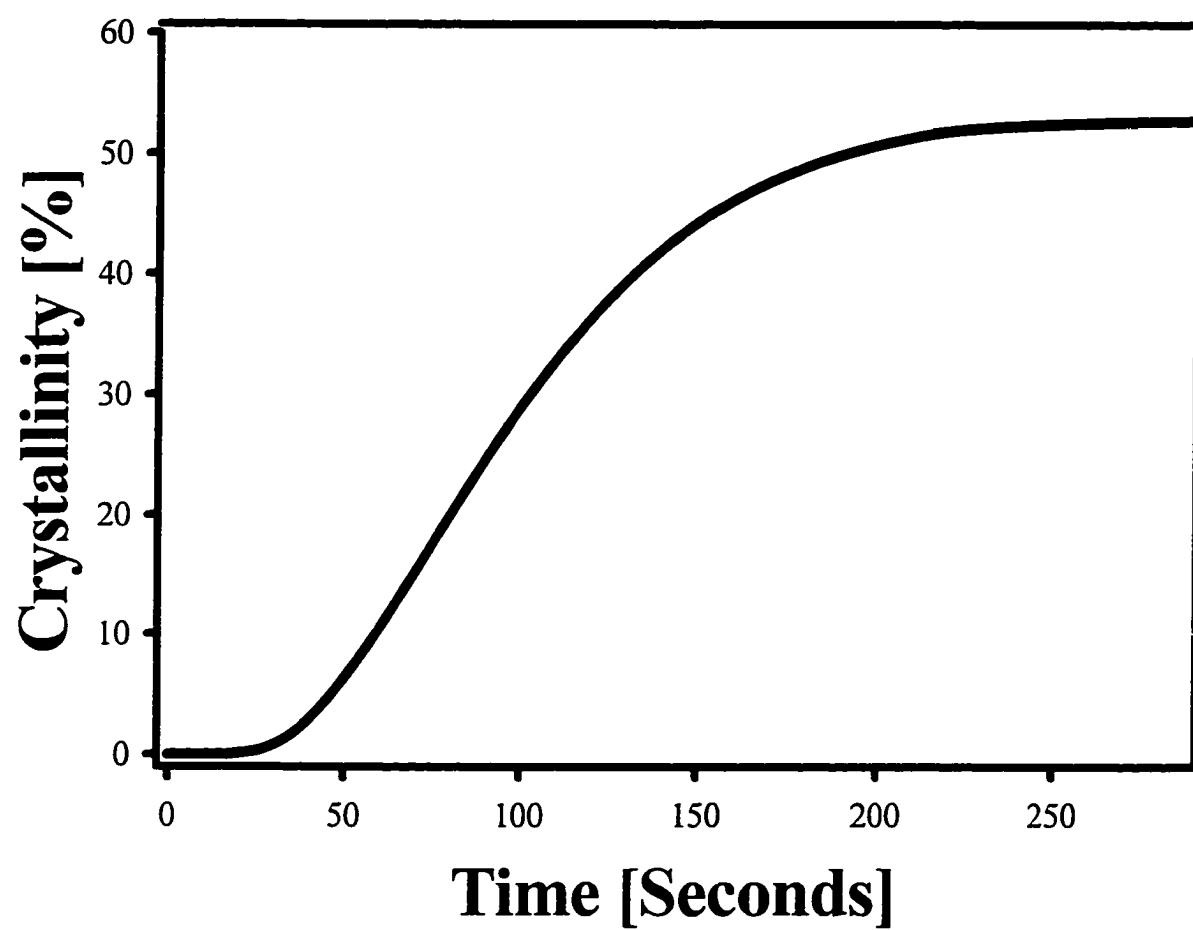


Figure 2-7 Crystallinity as a Function of Time for LDPE at 100°C



$$X(t) = \frac{A(t) \times r_{\text{dsc}} \times 100}{\Delta H_f^0 \times m_p \times f_{\text{dsc}}} \quad [2-14]$$

Where r_{dsc} is the DSC range setting in cal/min, and f_{dsc} is the DSC calibration constant determined from the indium crystallization peak. The area under the crystallization curve, $A(t)$, as a function of time was determined experimentally by integrating the cooling curve subtracted DSC output over the time period in which the sample crystallizes.

2.5 PHYSICAL PROPERTY EVALUATION

2.5.1 Conductivity Measurements

Depending on the filler loading of the composites, one of two methods was used to measure DC electrical conductivity. The conductivity at high filler loading was measured using four-point probe geometry, as outlined in the American Standard for Testing and Materials (ASTM) Standard D-4496 for moderately conductive materials. Copper electrodes were attached using a silver conductive epoxy (TRA-CON, BA-2902). The current was sent through the outer electrodes using a Keithley 610C electrometer as a current source and the voltage was measured using a Keithley 176 multimeter. The resistance, R , of the composite was determined from the linear portion of the current versus voltage curve by linear regression. The resistivity was calculated using Equation 2-15,

$$\rho = \frac{1}{\sigma} = \frac{Ra_R b_R}{c_R} \quad [2-15]$$

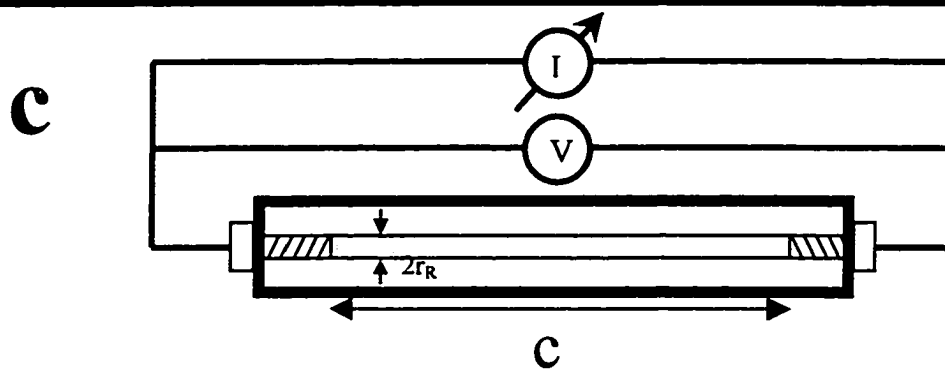
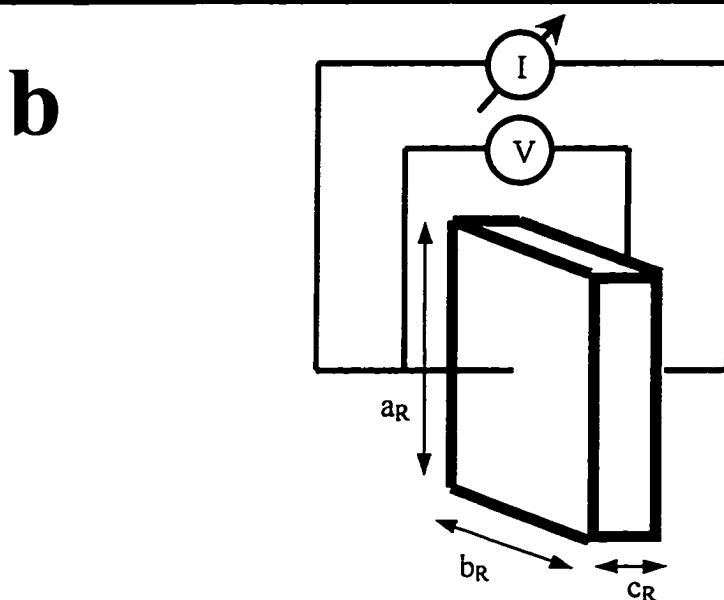
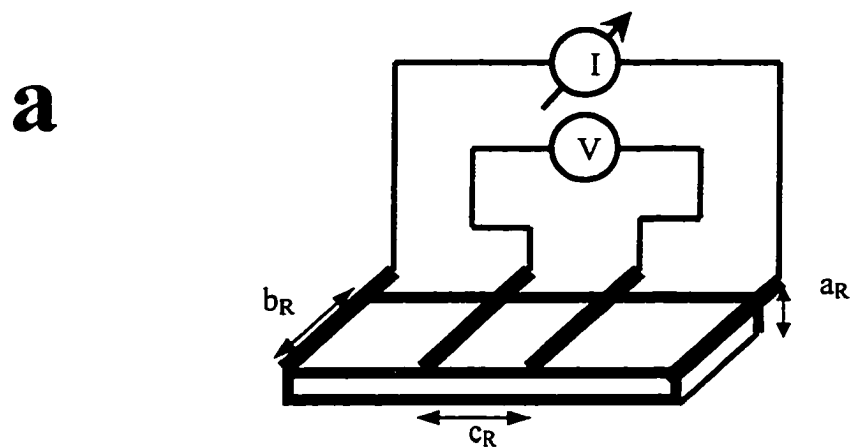
where a_R is the film thickness, b_R is the width, and c_R is the length as shown in Figure 2-8(a).

The conductivity of the composite films with low filler loading was measured using the sandwich method as outlined in ASTM standard D-257 for insulating materials. Thin composite films were placed in a Keithley Model 6105 Resistivity Chamber with a guard ring to bleed off surface current and one pound of contact pressure. A voltage was induced across the sample using a Keithley 247 High Voltage Power Source and the induced current was measured using a Keithley 610C Electrometer. The same algorithm was used to calculate the resistance as for the four-point probe geometry. Equation 2-15 was used to determine the resistivity, but with the dimension parameters a_R being the height, b_R , the width, and c_R , the distance between electrodes, as shown in Figure 2-8(b).

A different method was used to measure the powder conductivity of the filler; Figure 2-8(c) shows the geometry for the conductivity measurements of the fillers. Vibrational packing facilitated the maximum possible packing in the sample cell. A current was induce through the sample with an Instek model PS-6010 DC power supply and the voltage drop across the sample cell was measure using a Keithley 197A multimeter. Equation 2-16 yielded the conductivity of the fillers,

$$\rho = \frac{1}{\sigma} = \frac{R\pi r_R^2}{c_R} \quad [2-16]$$

Figure 2-8 Geometry for Different Conductivity Measurements; a) Four-point Probe; b) Sandwich; c) Powder Conductivity



r_R being the diameter and c the length of the conductivity chamber as shown in Figure 2-8(c).

2.5.2 Thermal Conductivity Ratio

The ratio of the composite thermal conductivity to the polymer thermal conductivity, k_c/k_p , was determined from the cooling curves for the melts and given by equating the dimensionless parameters of the heat transfer equation as given in Equation 2-17.¹¹

$$\frac{\alpha_c t_c}{b_c^2} = \frac{\alpha_p t_p}{b_p^2} \quad [2-17]$$

where t is the time required for thermal equilibrium for a specified temperature change, b_c and b_p are the sample thicknesses, and the thermal diffusivity of each phase, α_i , is given by Equation 2-18.

$$\alpha_i = \frac{k_i}{\rho_i C_i} \quad [2-18]$$

where k_i is the thermal conductivity, ρ_i is the density, and C_i is the heat capacity of the i^{th} phase. In each case, the thickness was determined from the mass of the polymer and the geometry of the system.

2.5.3 Tensile Properties

The tensile properties of the composites were measured with an Instron TT-C-L tensile tester with a specially designed computerized data acquisition system at a

stretching rate of 2.5 mm/min. The samples were produced with a ASTM Standard D-1708 die.

2.5.4 Stress Relaxation Measurements

The stress relaxation properties of the composites were measured with an Instron TT-C-L tensile tester with a specially designed computerized data acquisition system. An initial strain rate of 2.1 percent induced at a rate of 2.54 cm/min was used. The samples were produced with an ASTM Standard D-1708 die.

2.6 NOTATION

X, Y, Z	Cartesian Coordinates
\underline{S}	Vector in the Stretching Direction
\underline{N}	Vector Normal to the Crystalline Plane
α	Angle between \underline{S} and the X axis
β	Angle between \underline{S} and the Y axis
ε	Angle between \underline{S} and the Z axis
a, b, c	Points Forming a Crystal Plane
E	Angle between \underline{N} and the X axis
F	Angle between \underline{N} and the Y axis
G	Angle between \underline{N} and the Z axis
e, f, g	$\cos(E), \cos(F), \cos(G)$
h, j, l	Miller Indices
ϕ	Angle between \underline{S} and \underline{N}
θ	Diffraction Angle
χ	Azmuthal Angle
ρ	Resistivity
σ	Electrical Conductivity
R	Resistance
r_R	Radius of Powder Conductivity Cell
a_R	Height of Sample for Conductivity Measurements

b_R	Width of Sample for Conductivity Measurements
c_R	Length of Sample for Conductivity Measurements
α_c	Thermal Diffusivity of the Composite
α_p	Thermal Diffusivity of the Polymer
b_c	Thickness of the Composite Sample
b_p	Thickness of the Polymer Sample
t_c	Cooling Time of the Composite
t_p	Cooling Time of the Polymer
α_i	Thermal Diffusivity of the i^{th} Phase
k_i	Thermal Conductivity of the i^{th} Phase
ρ_i	Density of the i^{th} Phase
C_i	Heat Capacity of the i^{th} Phase
X	Fractional Crystallinity
ΔH_f	Experimentally Determined Heat of Fusion
ΔH_f^0	Heat of Fusion for Pure Crystalline Polyethylene
C_{PE}	Heat Capacity of Polyethylene
C_N	Heat Capacity of Nickel
C_{PC}	Heat Capacity of the Composite
t	Time
$X(t)$	Fractional Crystallinity as a Function of Time
$A(t)$	Area as a Function of Time

m_p	Mass of Polymer in a Sample
r_{dsc}	DSC Range Setting
f_{dsc}	DSC Calibration Constant

2.7 REFERENCES

- 1 M. Kakudo, and N. Kasai, X-Ray Diffraction by Polymers, Elsevier Publishing Company, New York, New York, 33, 153, 341-349, 1973.
- 2 L. E. Alexander, X-Ray Diffraction Methods in Polymer Science, Robert E. Krieger Publishing Company, Malbar, Florida, 249, 478, 1969.
- 3 T.J. Kistenmacher, T.E. Phillips, and D.O. Cowan, *Acta Cryst*, **B30**, 763 (1974).
- 4 C.W. Bunn, *Transactions of the Faraday Society*, **35**, 482 (1939).
- 5 A. Gupta, D. M. Simpson, and I. R. Harrison, *Plast. Eng.*, **49**, 33, (1993).
- 6 E. m. Barrall, II, and J. F. Johnson, in Techniques and Methods of Polymer Evaluation: Vol. 2: Thermal Characterization, edited by P. E. Slade and L. Tl Jenkins, Marcell Dekker, Inc., New York, 2, 1970.
- 7 Evaluation: Vol. 2: Thermal Characterization, edited by P. E. Slade and L. Tl Jenkins, Marcell Dekker, Inc., New York, 2, 1970.
- 8 R. B. Bird, R. C. Armstrong, and O. Hassager, Dynamics of Polymer Liquids: Vol. 1, Fluid Mechanics, 2nd Ed., John Wiley & Sons, New York, 209, 1987.
- 9 J. R. Welty, C. E. Wicks, and R. E. Wilson, Fundamentals of Momentum, Heat, and Mass Transfer, 3rd Edition, John Wiley & Sons, New York, NY, 753, 1984.
- 10 P.E. Slade, and L.T. Jenkins, Techniques and Methods of Polymer Evaluation, Volume 2, Thermal Characterization Techniques, Marcel Dekker, Inc., New York, NY, 26, 1970.

- 11 R. B. Bird, W. E. Stewart, and E. N. Lightfoot, Transport Phenomena, John Wiley & Sons, New York, 356, 1960.

CHAPTER 3

WIDE ANGLE X-RAY SCATTERING STUDY OF CRYSTALLINE ORIENTATION IN RETICULATE DOPED POLYMER COMPOSITES

3.1 INTRODUCTION

Reticulate doping consists of casting a composite film from a solution containing a polymer and a charge-transfer complex (CTC) and allowing the conductive, free radical salt to recrystallize as the solvent is removed from the polymer. In this study, a highly branched, low molecular weight polyethylene (PE) was doped with the CTC tetrathiafulvalene-tetracyanoquinodimethane (TTF-TCNQ). Wide angle x-ray scattering (WAXS), conductivity, optical microscopy, stress relaxation, and differential scanning calorimetry (DSC) measurements were used to show the effect of the addition of filler and uniaxial orientation on the mechanical and electrical properties of the composites.

3.2 BACKGROUND AND LITERATURE REVIEW

One novel method for producing conductive thermoplastic composites is reticulate doping of polymers with an organic charge transfer complex (CTC).¹ Reticulate doping consists of casting a composite film from a solution of both the polymer and CTC and allowing the conductive salt to microcrystallize in the polymer matrix forming conductive pathways.² Most CTC form long rod shaped crystals with high aspect ratios, thus conducting electricity at very low filler concentrations.^{3,4} Ulanski *et. al.* determined that recrystallization required for optimum conditions depends the viscosity of the solution and the solvent evaporation rate.⁵ Since both the viscosity and evaporation rate are temperature dependent, there is an optimum temperature for casting of the composite films for each charge transfer complex - polymer pair. At the optimum casting conditions, reticulate doped polymers conduct electricity at very low filler concentrations. In order to ensure recrystallization with some tetracyanoquinodimethane (TCNQ) salts, the composite must also have TCNQ⁰ added to the composite.⁶ These systems have a maximum conductivity at the ratio $[\text{TCNQ}^0]/[\text{TCNQ}_{\text{salt}}]=1$. Because the filler concentration is low, the mechanical properties of the composite are similar to those of the unfilled polymer matrix. Deformation of the matrix by cold drawing at an elongation as low as 6 percent destroyed the microcrystalline structure of the CTC and decreased the conductivity of the composite by two orders of magnitude.⁷ The greatest disadvantage to some organic conductors is the tendency to lose in conductivity in ambient conditions or over time. The conductivity of the CTC - polymer composites

remained constant for over one year because the insulating matrix protected the salt from the environment.⁸

Studies of the conductivity of solution cast films as a function of casting temperature, solvent, and concentration of CTC in the solution have been carried out for free-radical salts such as tetrathiothetracene-tetracyanoquinodimethane (TTT-TCNQ), tetrathiafulvalene-TCNQ (TTF-TCNQ), N-methyl phthalazinum (TCNQ)₂ (mPht(TCNQ)₂), N-propyl phthalazinium (TCNQ)₂ (PrPht(TCNQ)₂) and 2,2'-Bipyridylamine (TCNQ)₂ (BIPA(TCNQ)₂) in amorphous polymers, such as polycarbonate (PC) and polymethacrylate (PMMA), as well as semicrystalline polymers such as polyethylene (PE) and polypropylene (PP).⁹ The AC conductivity, thermopower, and magnetic properties of TTT-TCNQ and TTF-TCNQ films have been studied in order to obtain greater insight into charge transfer conduction mechanisms in reticulate doped polymers.^{10,11} In addition, Finter *et. al.* have tested a modified method for reticulate doping of polymers by in-situ complex formation and crystallization directly in the matrix as a method for producing films of insoluble charge transfer complexes.¹²

Often secondary shaping methods are required in order to obtain the necessary shape for a polymer composite application. Many of these processes change the morphology of the cast film and cause orientation of the polymer, which affects the relationship between CTC and the supporting matrix. This study looks at the effect of orientation via uniaxial stretching on the properties of reticulate doped polymer composites.

Uniaxially stretching a polymer composite aligns the filler particles in the stretching direction and creates internal stresses. The alignment of the anisotropic conductive filler increases conductivity in the stretching direction, due to an increased number of particle-particle contacts. However, the centers of the particles also become separated, hence a plot of conductivity in the longitudinal direction versus draw ratio generally shows a maxima due to these two competing effects. To further complicate this behavior, the internal stress can affect the efficiency of electron transfer from one particle to another, especially at low strains. Our experiments were not able to separate these complicated phenomena, rather they indicated how these effects combine to change the conductivity in the stretching direction.

Composites of TTF-TCNQ supported by a highly branched, low molecular weight polyethylene (PE) were produced with varying filler concentrations and draw ratio. TTF-TCNQ, shown in Figure 1-5(a), was chosen as the CTC. TTF-TCNQ has a very high single crystal conductivity of approximately 500 S/cm, is well characterized and scatters at angles that do not overlap with scattering from PE in selected regions.^{13,14} PE was chosen because it is often used as the supporting matrix in conductive thermoplastic composites. PE was a highly branched, low molecular weight polymer with a density of 0.906 g/cc. The weight average molecular weight was 35,000 g/mole and the polydispersity index was 4.5. The melting point of the material was approximately 90°C and the melt flow index was 2250 grams per 10 minutes at 190°C. This particular grade of PE, while having a lower melting point and crystallinity than most commercial

grades of low density polyethylene, was chosen as the matrix because of its solubility in chlorobenzene at high polymer concentrations. WAXS experiments were done in conjunction with conductivity measurements, optical microscopy, stress relaxation measurements, and differential scanning calorimetry (DSC) in order to more fully understand the effects of TTF-TCNQ on the matrix morphology and bulk properties of reticulate doped polymer composites.

3.3 EXPERIMENTAL PROCEDURES

TTF was synthesized and purified by the procedure outlined by Narita and Pittman and summarized in Appendix C.¹⁵ TTF was complexed with TCNQ (Aldrich) by crystallization from a solution of acetonitrile (Aldrich). Composite films were produced by making a 10 mM solution of TTF-TCNQ in chlorobenzene (Aldrich). PE (Aldrich) was dissolved by adding 10 milliliters of chlorobenzene for every gram of PE at 100°C. The procedure for solution casting outlined in Section 2.2.1 was followed for film production. The physical property measurements for conductivity (2.3.1), tensile modulus (2.4.3), stress relaxation (2.4.4), and fractional crystallinity (2.3.5) were carried out for each sample concentration. The procedures used in WAXS and optical microscope images are described in sections 2.3.1 and 2.3.2, respectively.

3.4 RESULTS AND DISCUSSION

As expected, reticulate doping of polymers allows conductive pathways to be formed at very low volume fractions due to the formation of microcrystallites inside the matrix.^{16,17,18} Figure 4 shows the percolation diagram for the unstretched PE composites. The conductivity profile should follow a sigmodal curve where the percolation threshold is the point of the upturn in the diagram. The lack of an upturn in Figure 3-4 indicates that the critical volume fraction is below 2.5 percent by volume (4.5 percent by weight). The percolation threshold for the TTF-TCNQ composites is much lower than that of conventional fillers such as carbon black and metal powders, which have critical volume fractions of 10 percent and 30 percent, respectively.^{19,20} The critical region ends when the conductivity is no longer a strong function of volume fraction which, for the TTF-TCNQ - PE system, is between 5.0 and 10.0 percent by volume (8.8 and 17.0 percent by weight).

Figure 3-2 contains two photos from a Nikon Optical Microscope of the TTF-TCNQ both at 320X (a) showing the long rod shaped particles and at 800X (b) showing the branching from one particle. Optical microscopy showed that there was a large distribution of aspect ratios of the TTF-TCNQ for a given volume fraction and both the maximum and average aspect ratios were drastically affected by the volume fraction of filler. The maximum aspect ratio, shown in Figure 3-3(a), was largest for the TTF-TCNQ cast onto a surface with no matrix and consistently decreased as a function of TTF-TCNQ volume fraction in the reticulate doped composites. The average aspect

ratio, shown in Figure 3-3(b), decreased rapidly in presence of the matrix, but was constant at high filler loading. Metal fibers with a similar aspect ratio still required at least 5 percent by volume in order to create a continuous conductive network, a much higher volume fraction than found in this study for TTF-TCNQ.²¹ There was a significant amount of branching of the TTF-TCNQ particles which probably decreases the percolation threshold by acting as an interconnect for TTF-TCNQ.

Experimentally obtained diffraction patterns for TTF-TCNQ and PE are shown in Figures 3-4 and 3-5, respectively. Table 1 contains the literature values for the unit cell parameters, density, and heat of fusion (ΔH_f) for both components. The unit cell parameters obtained from the diffraction pattern closely matched those from the literature, confirming that the filler was TTF-TCNQ. Figure 3-6 shows 2Θ from 20° to 25° , the region of interest for the orientation studies, for both the TTF-TCNQ and the PE and indicates that there is no significant scattering of the TTF-TCNQ at either $[110]$ or $[200]$ PE reflection planes.

Figures 3-7 show pole figures at a diffraction angle of 21.4° for 10 percent by volume TTF-TCNQ at draw ratios of 1.0 and 2.0, respectively. For perfectly unoriented materials the relative intensity would be constant. The slight increase in intensity with χ in Figure 3-7(a) indicates a slight preferential orientation in the unstretched composites, while in Figure 3-7(b), the sharper increase in intensity with azimuthal angle, χ , shows much higher PE crystalline orientation. Figure 3-8 shows the orientation as a function

Figure 3-1 Percolation Diagram for TTF-TCNQ filled PE

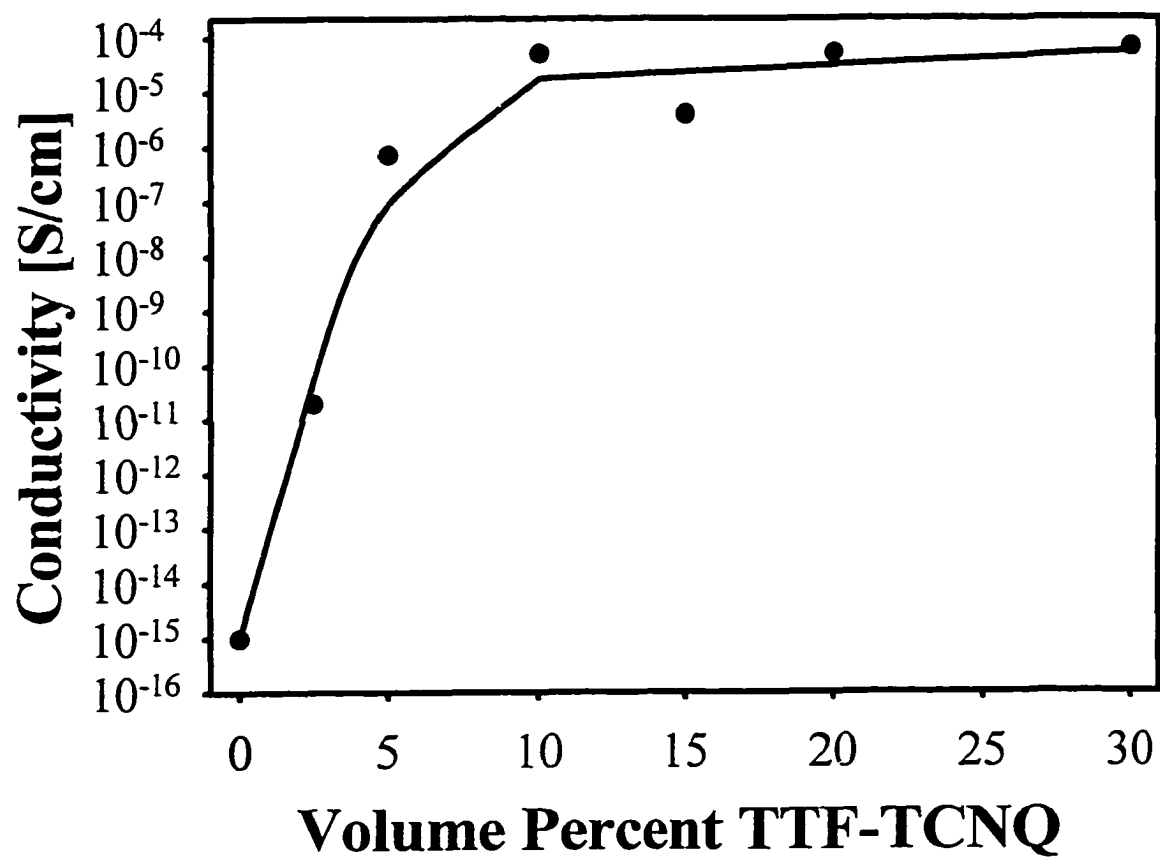


Figure 3-2 Optical Microscope Image of TTF-TCNQ Particles; a) 320X Magnification;
b) 800X Magnification

a



b

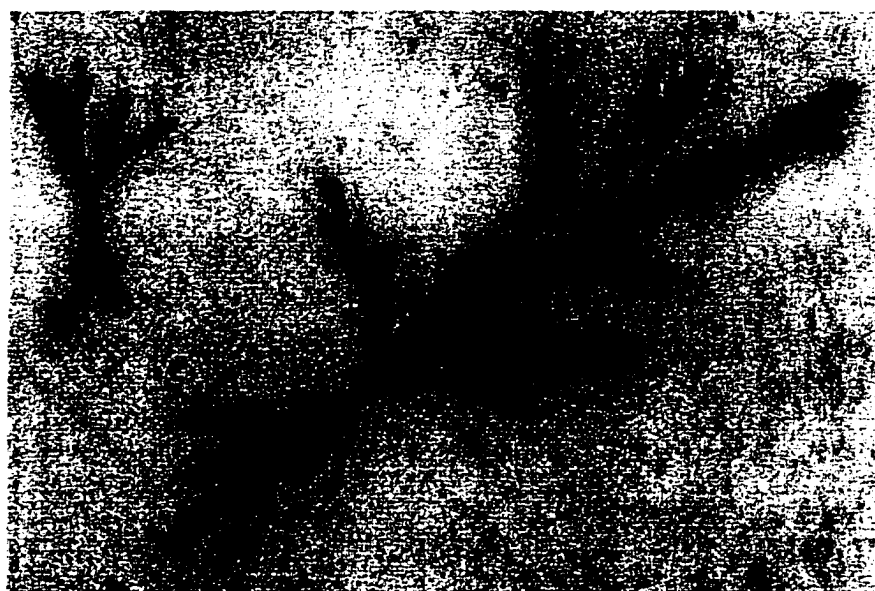


Figure 3-3 a) Maximum Aspect Ratio of TTF-TCNQ as a Function of TTF-TCNQ Concentration; b) Average Aspect Ratio of TTF-TCNQ as a Function of TTF-TCNQ Concentration

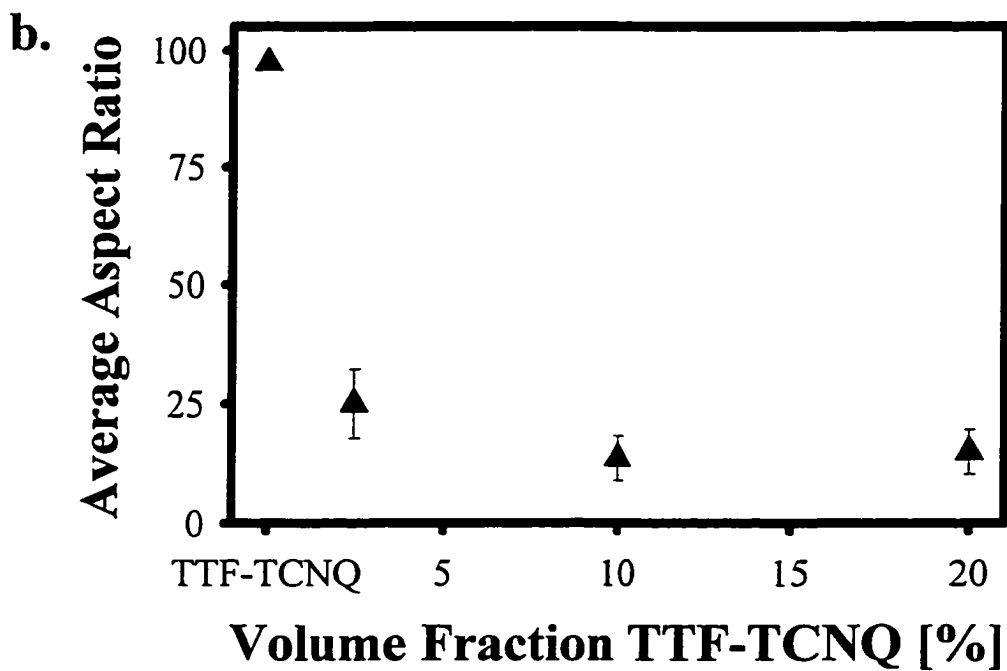
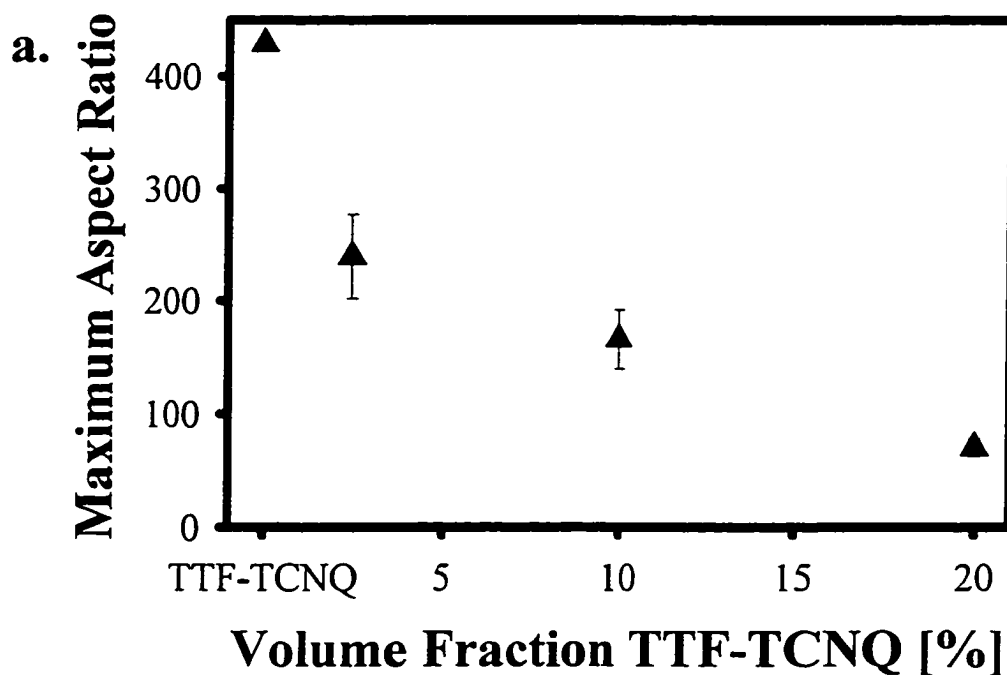


Figure 3-4 Diffraction Pattern for TTF-TCNQ

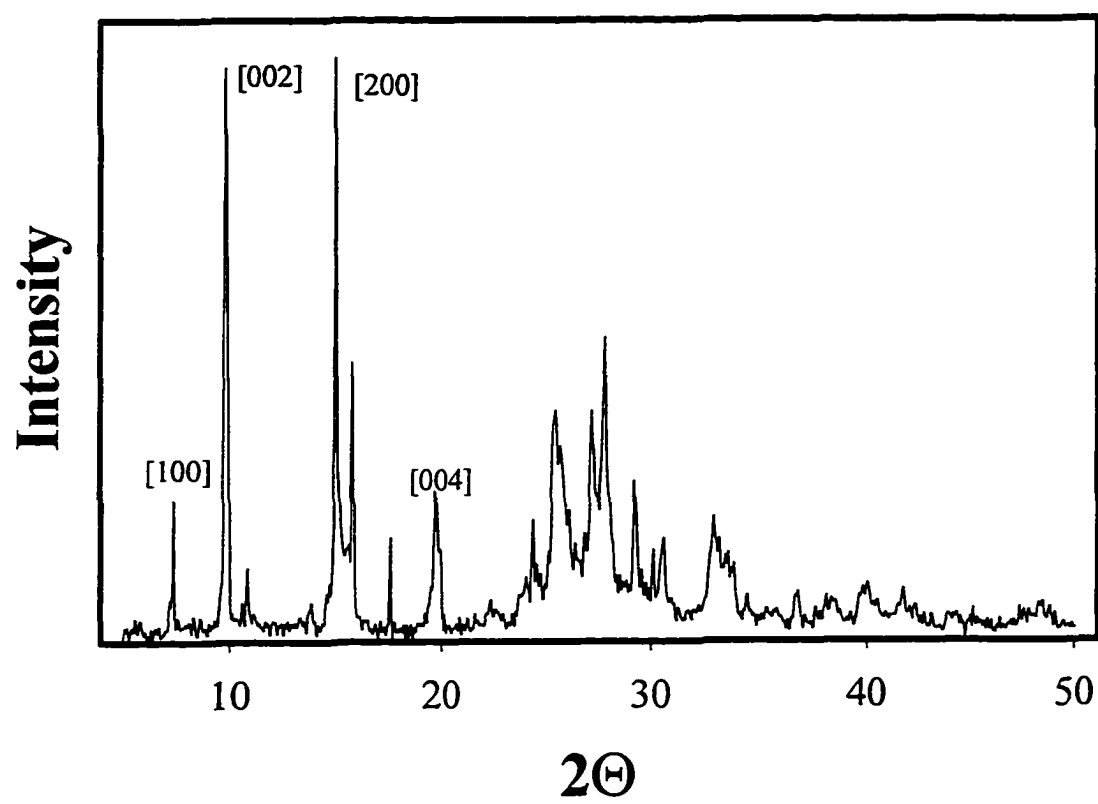


Figure 3-5 Diffraction Pattern for PE

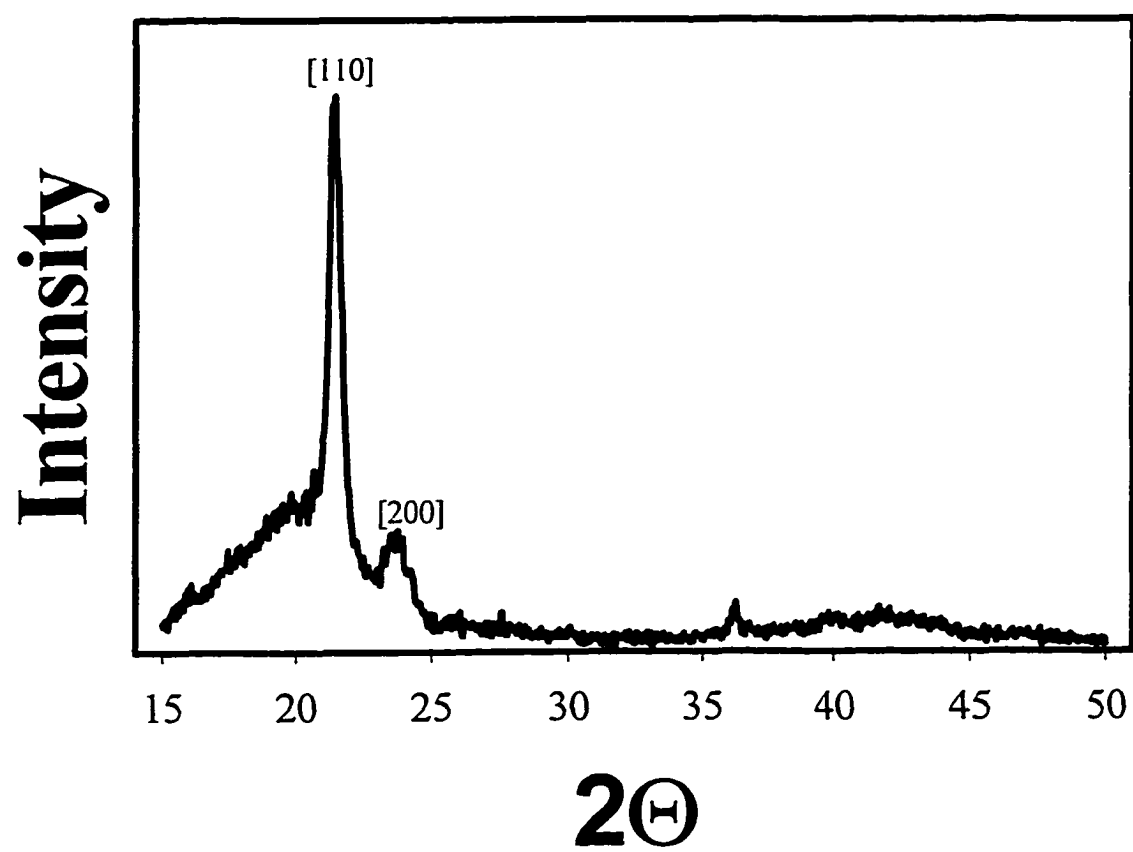


Table 3-1 Crystallographic Parameters and Physical Properties

Material	Unit Cell Parameters					Density		ΔH_f [J/g]
	Cell	a	b	c	Angle	Amorp. [g/cc]	Cryst. [g/cc]	
Polyethylene	Orthorhombic	7.4	4.9	2.5		0.851	1.002	282
TTF-TCNQ	Monoclinic	12.3	3.8	18.5	104.5		1.620	336

of TTF-TCNQ volume fraction for the unstretched samples. In composites with TTF-TCNQ concentrations of 0, 2.5, and 5 percent by volume, the PE crystallites were slightly oriented perpendicular to the casting surface. In samples with higher filler concentrations in the plateau region of conductivity, the crystallites were oriented slightly parallel to the casting surface. Reticulate doping has been shown to form long rod shaped crystals with the conducting phase forming a two-dimensional network parallel or at small angles to the casting plane.^{11,22} This network oriented the PE crystallites parallel to the casting surface as indicated by the shift in initial orientation from slightly perpendicular to slightly parallel to the casting surface.

Figure 3-9 shows the orientation of the PE crystallites as a function of draw ratio for 0, 2.5, 10, and 20 percent by volume TTF-TCNQ. As expected, crystalline orientation in the stretch direction increased with increasing draw ratio. The increase in orientation resulting from uniaxial stretching decreased with increasing filler concentration, i.e. the slope of the lines in Figure 3-9 were lower for higher TTF-TCNQ concentrations. One explanation for this behavior is that the addition of TTF-TCNQ to the polymer causes a decrease in the relaxation time. To test this hypothesis, stress relaxation measurements were performed.

Stress relaxation measurements were done at room temperature, while stretching was done at approximately 80°C. Thus, the relaxation measurements are not directly comparable to the stretching conditions, but give some insight into the effect of TTF-

Figure 3-6 WAXS comparison for TTF-TCNQ and PE

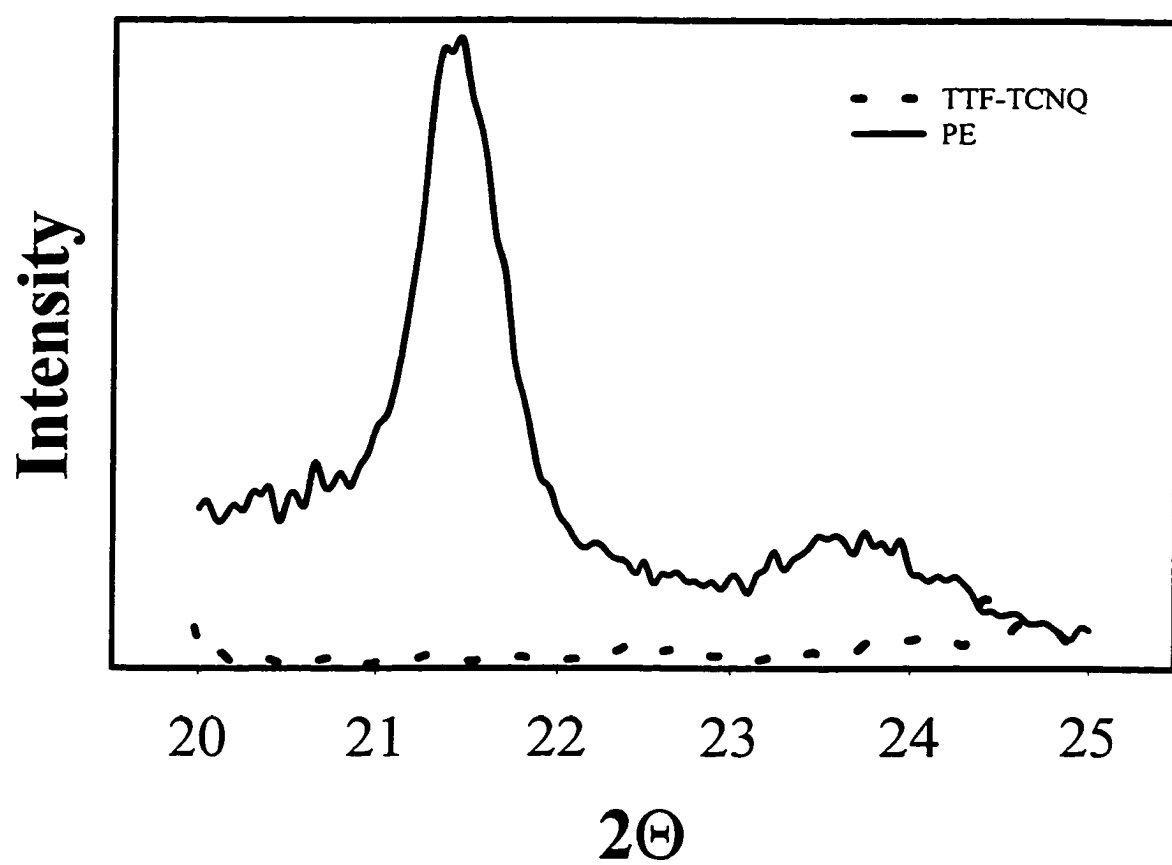


Figure 3-7 Chi Scan at 21.4° for a 10 % by Volume TTF- TCNQ Composite; a) Unstretched; b) Stretched to $\lambda=2.0$ (The solid lines have been added to guide the eye and are not intend to indicate any functional form of the intensity.)

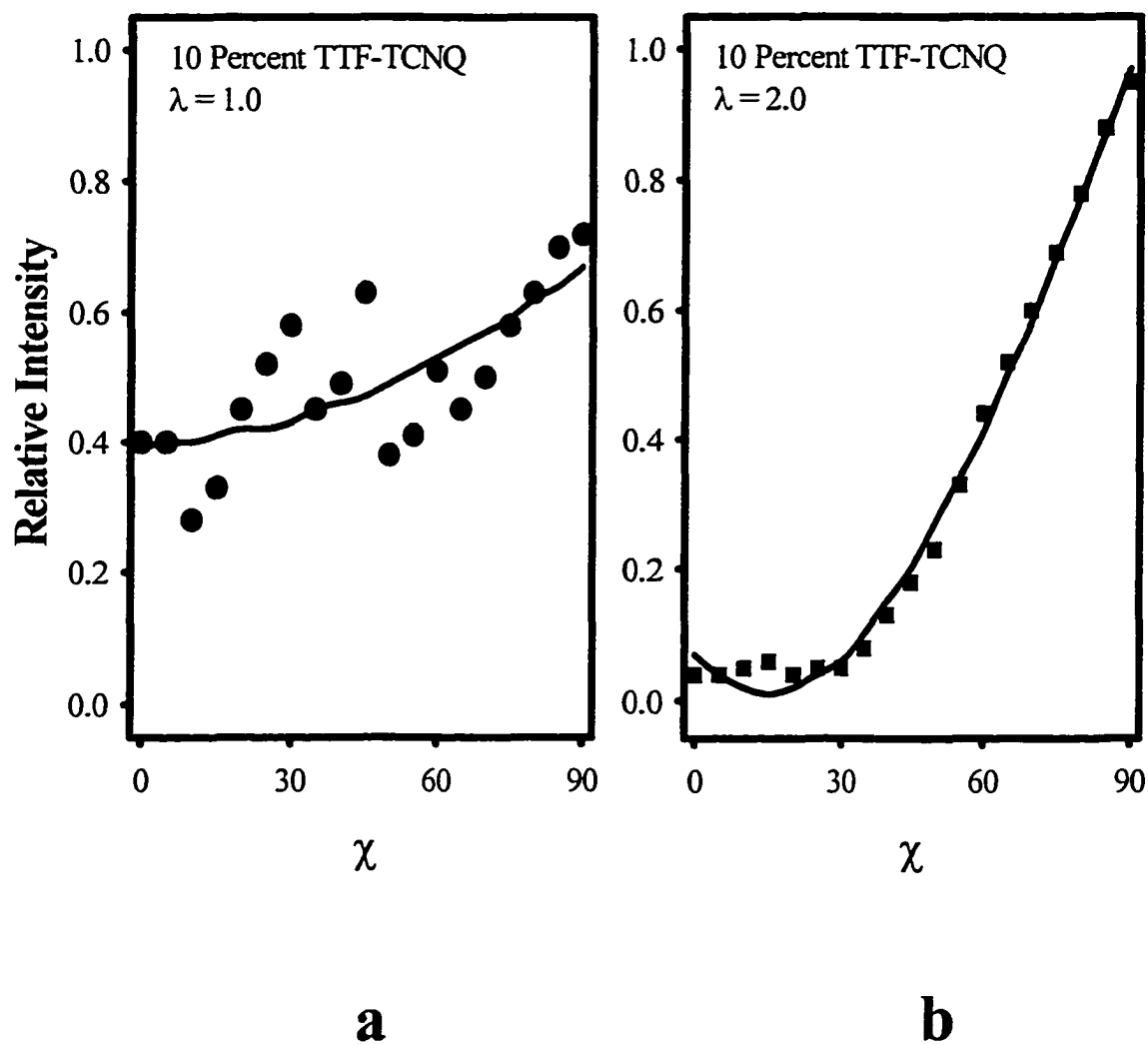
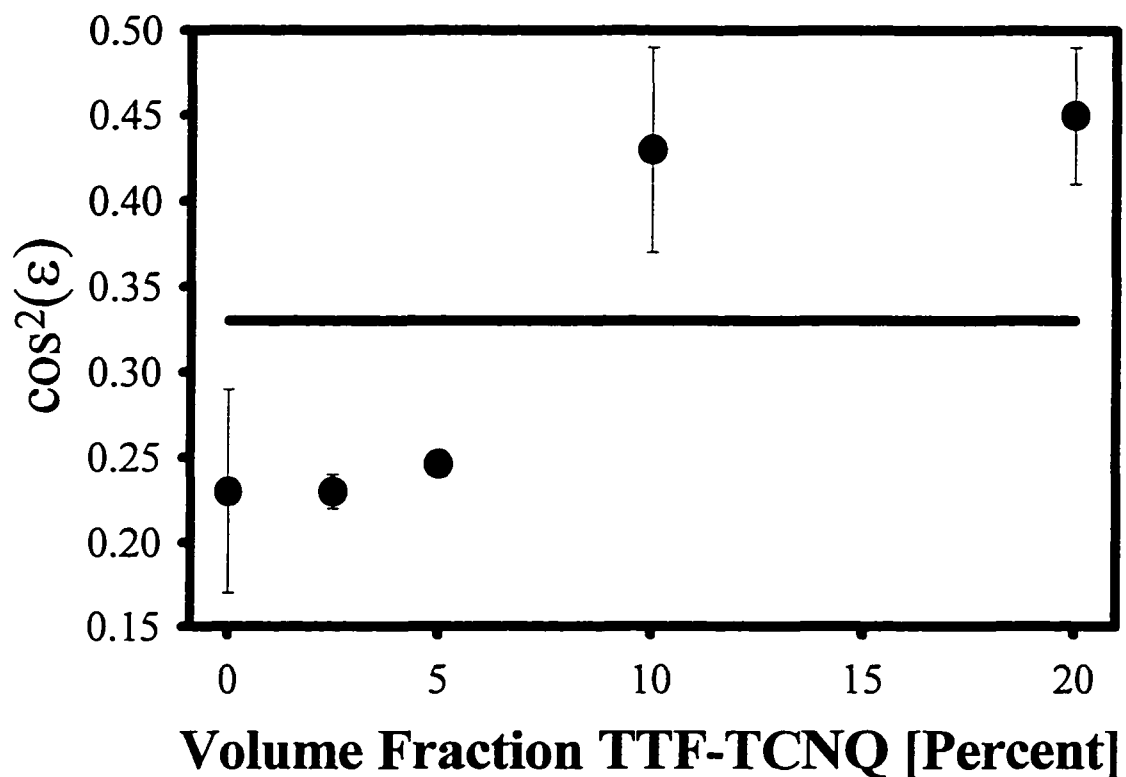


Figure 3-8 Orientation of Unstretched TTF-TCNQ filled PE as a Function of Filler Volume Fraction; The line drawn at $\cos^2(\epsilon) = 1/3$ represents a sample with no net polymer chain orientation; $\cos^2(\epsilon) < 1/3$ represents a sample with preferential orientation perpendicular to the casting surface; $\cos^2(\epsilon) > 1/3$ represents a sample with preferential orientation parallel to the casting surface



TCNQ on the relaxation process. Figure 3-10 is a plot of the first 30 seconds of the relaxation measurements for several different concentrations of TTF-TCNQ. The downward shift indicates faster relaxation for increasing TTF-TCNQ. This effect was quantified by fitting the experimental data to relaxation models to determine the relaxation time constants as a function of filler volume fraction. The simple Maxwell model shown in Equation 3-1, with one relaxation time, τ , was used to model the data, but this model had an average correlation coefficient of 0.845 and clearly did not fit the data.

$$\frac{E(t)}{E(0)} = e^{-\frac{t}{\tau}} \quad [3-1]$$

The failure of the one parameter model was not unexpected since polymeric materials have several different relaxation processes occurring simultaneously at different rates, such as segmental motion, chain coiling and uncoiling, and chain alignment.²³ Models with only one time constant are usually only valid over a very limited range of time and real polymer systems often require the characterization of several time constants.²⁴ The Maxwell - Wiechert model, shown in Equation 3-2, was used to model the data.

$$\frac{E(t)}{E(0)} = \sum_0^{\infty} E_i e^{-\frac{t}{\tau_i}} \quad [3-2]$$

An acceptable fit with an average coefficient of determination of 0.970 was obtained

Figure 3-9 Orientation of Stretched TTF-TCNQ-Filled PE as a Function of Draw Ratio and Filler Volume Fraction

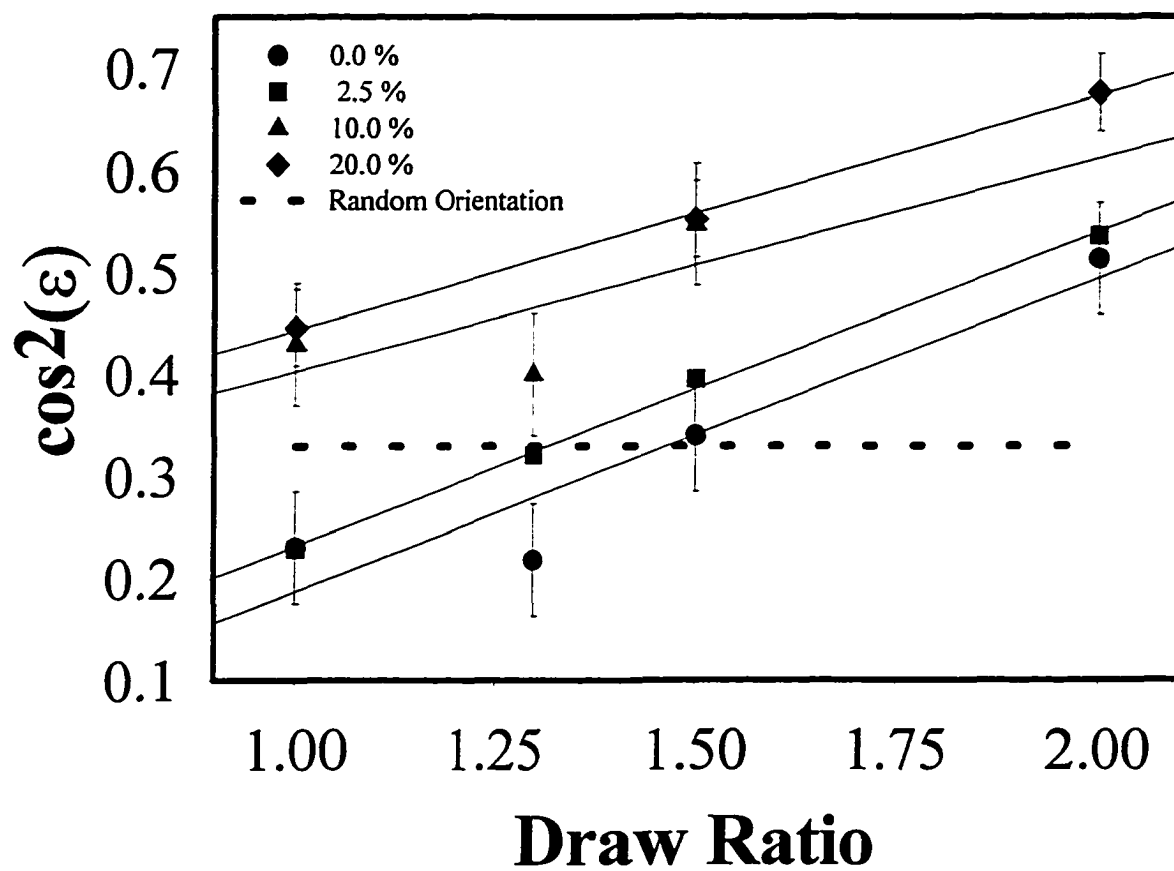
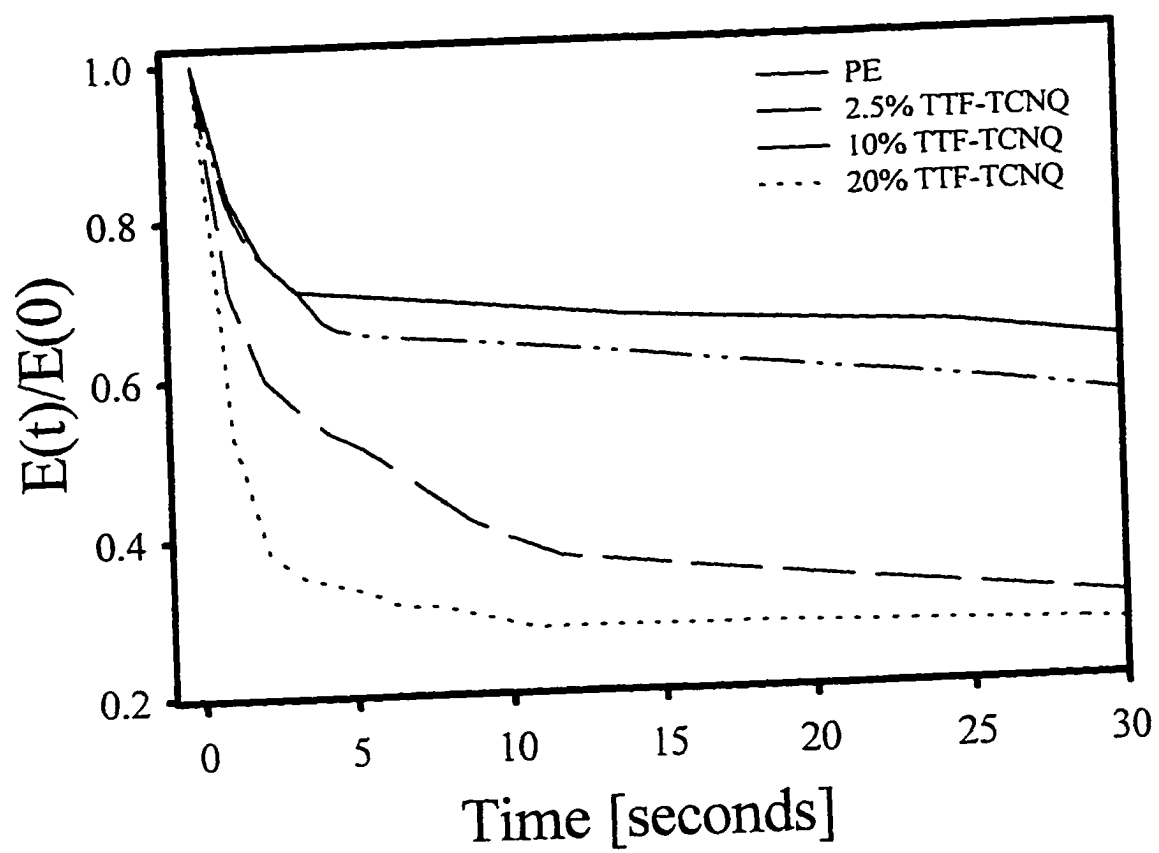


Figure 3-10 Stress Relaxation of TTF-TCNQ-Filled PE as a Function of Filler Loading



with two terms and the equation was truncated after the second term as shown in Equation 3-3.²⁵

$$\frac{E(t)}{E(0)} = E_0 e^{\frac{-t}{\tau_0}} + E_1 e^{\frac{-t}{\tau_1}} \quad [3-3]$$

E_i are the dimensionless relaxation moduli and τ_i are the relaxation times. E_0 and E_1 were 0.49 ± 0.03 and 0.34 ± 0.04 , respectively, with no significant changes with volume fraction of TTF-TCNQ. The tensile modulus was 115 ± 16 MPa and was also not affected by the presence of the filler. Therefore, the constant tensile modulus is consistent with the observed constant relaxation moduli.

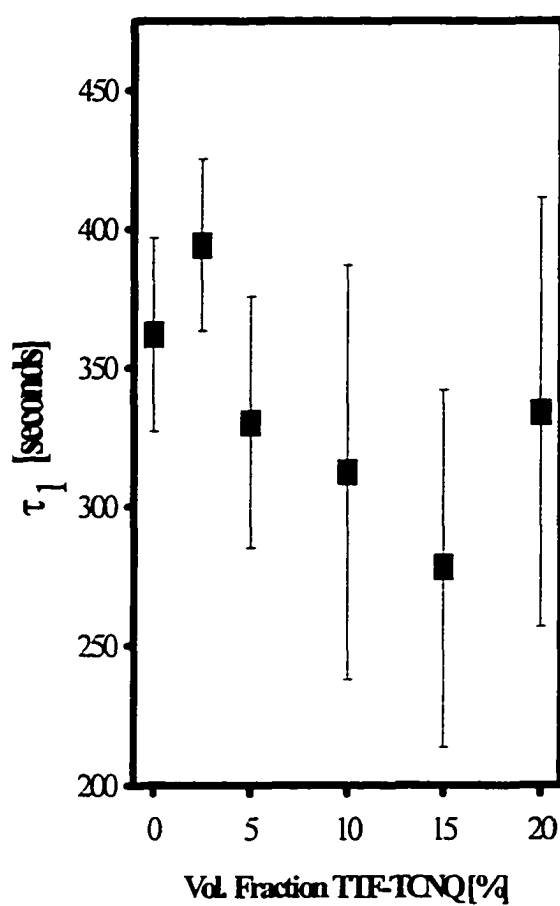
Relaxation times, however, were not constant with volume fraction indicating that perhaps different relaxation times might account for the difference in orientation of stretched found in WAXS experiments. Figure 3-11(a) shows the relaxation time corresponding to the slower process, τ_1 , may slightly decrease with increasing volume fraction, but the errors in measurement make it difficult to draw this conclusion with certainty. Figure 3-11(b) shows that the relaxation time corresponding to the faster process, τ_0 , definitely decreased with increasing volume fraction and remained constant at filler loadings above the critical region. Figure 3-11 indicates that relaxation of the unfilled PE or low volume fraction filled polymers was slower than that of the highly filled polymer. Therefore the initial hypothesis was confirmed: the addition of TTF-TCNQ causes a decrease in the relaxation time and may be the cause of the decrease in PE crystallite orientation in WAXS measurements.

Stretching the composites led to an initial increase in conductivity followed by a 5 order of magnitude drop in conductivity, measured in four-point probe geometry, as shown in Figure 3-12. Initial stretching caused an increase in conductivity most likely as a result of TTF-TCNQ particles forming more linear conductive pathways. As draw ratio increased further, the conductive rods were either broken by the stress or the rods were pulled apart leading to fewer conductive pathways and a decrease in conductivity.

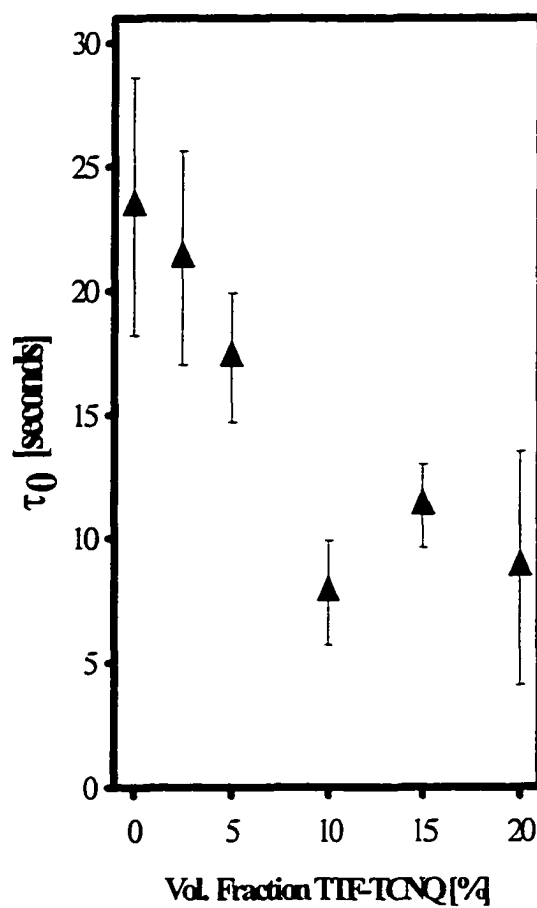
The fractional crystallinity of the unstretched material was determined by DSC to be 22.7 ± 1.6 percent and was unaffected by volume fraction of filler. Because this fractional crystallinity was extremely low for a polyethylene, the crystallinity was calculated from WAXS experiments to confirm the DSC results. The fractional crystallinity from WAXS using the parameter $B=3.25$ as reported by Kakudo and Kasai was 19.9% for the unfilled material which is well within the normal differences found by these two methods.²⁶

Figure 3-13 shows the baseline subtracted DSC curves for the 2.5 percent TTF-TCNQ composites as a function of draw ratio. As expected, the crystallinity did increase with draw ratio, but the addition samples of TTF-TCNQ inhibited crystallization during stretching as shown in Figure 3-14. The incremental increase in crystallinity due to stretching declined with TTF-TCNQ volume fraction until the concentration was above the critical region, where no increase in crystallinity with stretching was observed.

Figure 3-11 a) Slower Relaxation Time as a Function of Volume Fraction TTF-TCNQ; b) Faster Relaxation Time as a Function of Volume Fraction TTF-TCNQ



a



b

Figure 3-12 Composite Conductivity as a Function of Volume Fraction TTF-TCNQ and Draw Ratio (parallel to stretching direction)

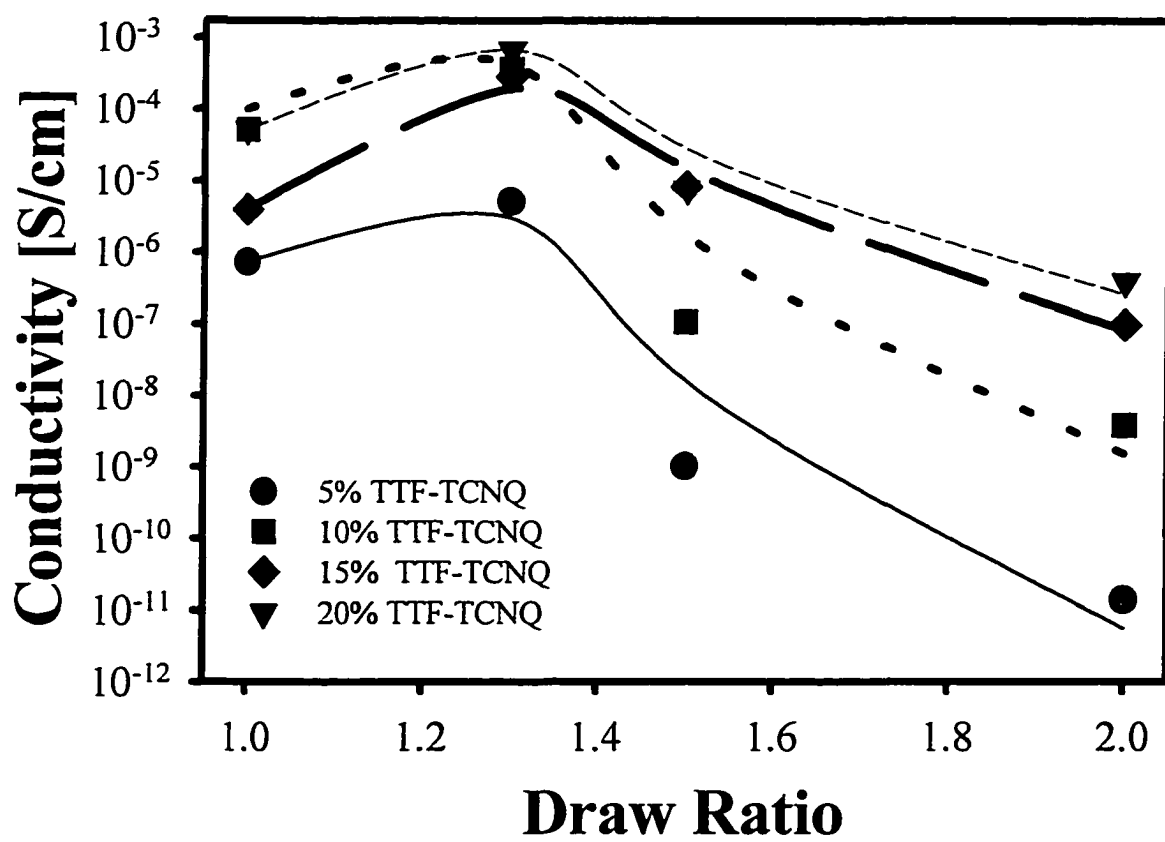
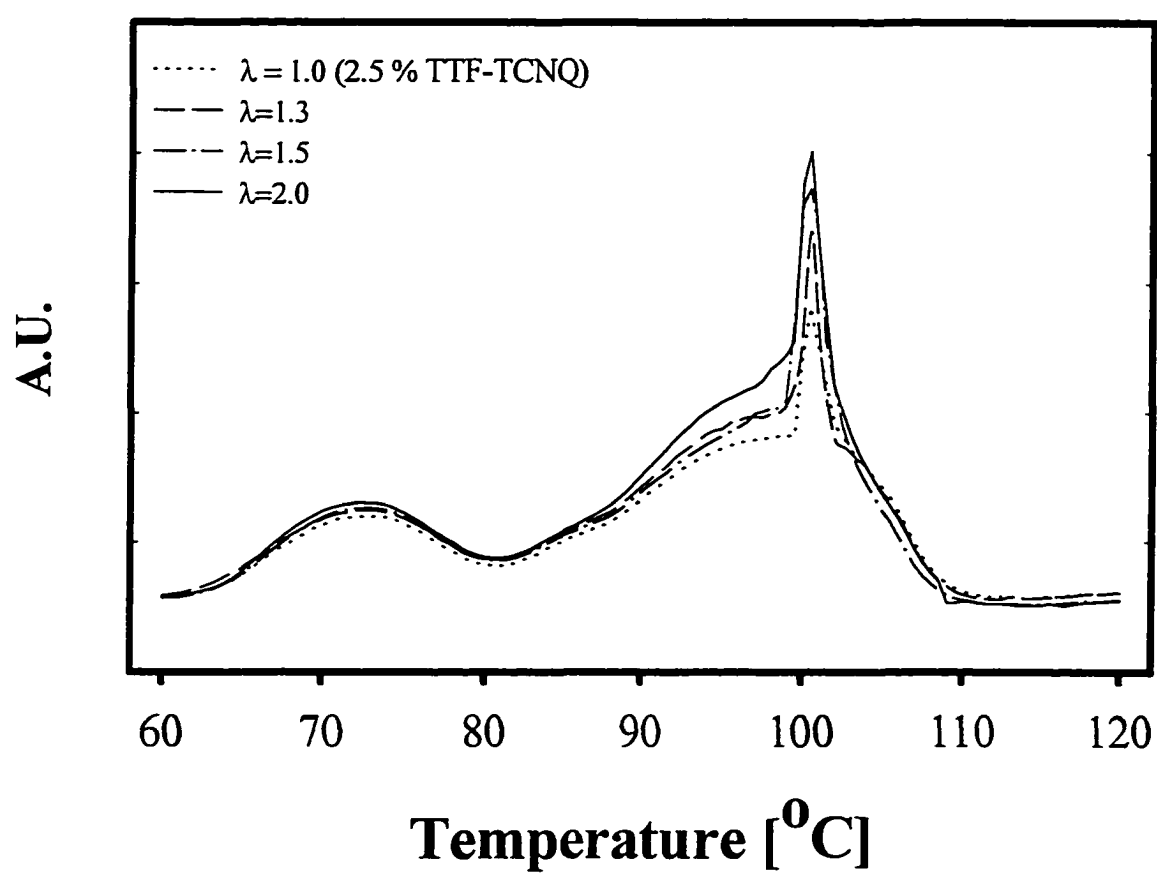


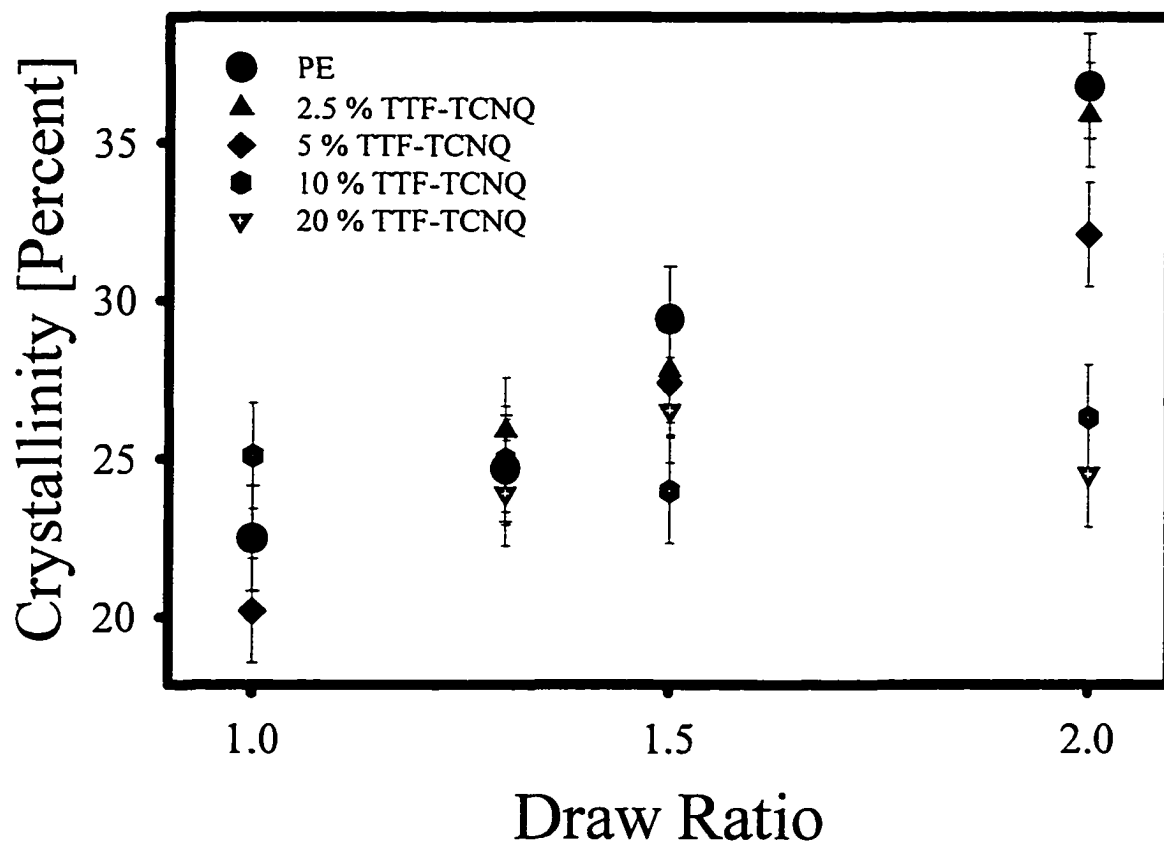
Figure 3-13 Baseline Subtracted DSC Curves for Stretched, 2.5% TTF-TCNQ Composite Films as a Function of Draw Ratio



3.5 CONCLUSIONS

Solution cast films of PE showed orientation of the crystallite lamella perpendicular to the casting surface, but the addition of TTF-TCNQ microcrystallizing inside the matrix forced PE crystals to preferentially form parallel to the casting surface. Uniaxial stretching parallel to the casting surface increased the orientation of the crystallites along the stretching direction. The incremental increase in orientation with stretching was decreased with higher filler loading. The conductivity of the composites decreased by approximately 5 orders of magnitude by stretching to a draw ratio of 2.0. In addition, the fractional crystallinity of the PE was not affected by the volume fraction of TTF-TCNQ. The incremental increase in fractional crystallinity attained by stretching decreased in the critical region, and above the critical region the fractional crystallinity was constant for all draw ratios tested.

Figure 3-14 Fractional Crystallinity of TTF-TCNQ-Filled PE as a Function of Draw Ratio



3.6 NOTATION

ε	Angle between \underline{S} and \underline{Z} ; see Figure 2-4(a)
χ	Azimuthal Angle
\underline{S}	Vector in the Stretching Direction
\underline{Z}	Cartesian Coordinate
λ	Draw Ratio (length/initial length)
ΔH_f	Heat of Fusion
t	Time
$E(t)$	Relaxation Modulus
$E(0)$	Young's Modulus
E_i	Dimensionless Relaxation Modulus
τ_i	Relaxation Times
E_0	Dimensionless Relaxation Modulus Corresponding to the Faster Relaxation Process
τ_0	Relaxation Time Corresponding to the Faster Relaxation Process
E_l	Dimensionless Relaxation Modulus Corresponding to the Slower Relaxation Process
τ_l	Relaxation Time Corresponding to the Slower Relaxation Process

3.7 REFERENCES

- 1 J. Ulanski, *Synthetic Metals*, **41**, 923, (1991).
- 2 J. Ulanski, J.K. Jeszka, M. Kryszewski, and A. Tracz, *Pure and Applied Chemistry*, **56**, 355 (1984).
- 3 J. Ulanski, *Synthetic Metals*, **41**, 923 (1991).
- 4 J. R. Ferraro, and J. M. Williams, Introduction to Synthetic Electrical Conductors, Academic Press, Inc., New York, New York, 112, 1987.
- 5 J. Ulanski, J. K. Jeszka, M. Kryszewski, and A. Tracz, *Pure and Appl. Chem.*, **56**, 355, (1984).
- 6 O. K. Kim, R. B. Fox, *J. Polym. Sci., Polym. Chem.*, **20**, 2765, (1982).
- 7 J. Ulanski, and M. Kryszewski, *Pol. J. Chem.*, **69**, 651, (1995).
- 8 O. K. Kim, *J. Polym. Sci., Polym. Let.*, **21**, 575, (1983).
- 9 J. Ulanski, *Synthetic Metals*, **39**, 13 (1990).
- 10 J. K. Jaszka, A. Tracz, and M. Kryszewski, *Synthetic Metals*, **55**, 109 (1993).
- 11 J. K. Jaszka, *Synthetic Metals*, **59**, 151 (1993).
- 12 J. Funter, C. W. Mayer, *Synthetic Metals*, **41**, 951 (1991).
- 13 R. V. Germmer, D. O. Cowan, T. O. Poehler, A. N. Bloch, R. E. Pyle, and R. H. Banks, *J. Org. Chem.*, **40**, 3544 (1975).
- 14 T. J. Kistenmacher, T. E. Phillips, and D. O., Cowan, *Acta. Cryst.*, **B30**, 763 (1974).
- 15 M. Narita, and C. U. Pittman, Jr., *Synthesis*, 489 (1976).

- 16 W. B. Genetti, R. J. Lamirand, and B. P. Grady, *J. Appl. Polym. Sci.*, **70**, 1785, (1998)
- 17 J. Ulanski, A. Tracz, and M. Kryszewski, *J. Phys., D*, **18**, 451 (1985).
- 18 A. Tracz, and J. K. Jeszka, *Synthetic Metals*, **41**, 1831 (1991).
- 19 S. M. Aharoni, *J. Appl. Phys.*, **43**, 246, (1972).
- 20 K. Miyasaka, K. Watanabe, E. Jojima, H. Aida, M. Sumita, K. Ishikawa, *J. Mater. Sci.*, **17**, 1610 (1982).
- 21 D. E. Davenport, in Polymer Science and Technology: Conductive Polymers, R. B. Seymour , editor, Plenum Press, New York, New York, 39, 1981.
- 22 J. K. Jeszka, *Synthetic Metals*, **45**, 15 (1991).
- 23 R. J. Stokes, and D.F. Evans, Fundamentals of Interfacial Engineering, Wiley, New York, NY, 675, 1997.
- 24 L. E. Nielsen, and R. F. Landel, Mechanical Properties of Polymers and Composites, 2nd Ed., Marcel Dekker, Inc. New York, NY, 69, 1994.
- 25 J. J. Aklonis, and W. J. MacKnight, Introduction to Polymer Viscoelasticity, 2nd Ed., Wiley, New York, NY, 150, 1983.
- 26 M. Kakuda, and N. Kasai, X-Ray Diffraction by Polymers, Elsevier Publishing Company, New York, NY, 33, 153, 341-349, 1973.

CHAPTER 4

ISOTHERMAL CRYSTALLIZATION OF NICKEL FILLED LOW DENSITY POLYETHYLENE

4.1 INTRODUCTION

The effect of nickel filler on the crystallization kinetics of low-density polyethylene (LDPE) crystallites has been quantified and compared to the filler's effect on electrical and thermal properties. The crystallization kinetics were changed by the addition of nickel in two ways; the nucleation time for a given isothermal crystallization temperature was reduced and the crystallization rate increased. Crystallization rates were compared by fitting the data to the Avrami equation. The Avrami exponent was not affected by the addition of nickel, indicating the change in crystallization rate was due to increased crystal growth rate rather than nucleation. The increase in crystal growth rate was consistent with the increase in composite thermal conductivity caused by the addition of nickel. However, an anomalous jump, not present in the bulk thermal conductivity, occurred between 7.5 and 10 percent nickel by volume for all temperatures studied. This jump coincided with the end of the critical region in electrical

conductivity. The cause of this jump is not absolutely clear; however, we believe the shift is due to the formation of a continuous network of nickel particles causing an increase in the local heat dissipation.

4.2 BACKGROUND AND LITERATURE REVIEW

4.2.1 Isothermal Crystallization

Semi-crystalline polymers, such as low and high density polyethylene (LDPE, HDPE), polypropylene (PP), and polyethylene terephthalate (PET) play an important role as commodity thermoplastics because of the unique physical properties that result from the combination of amorphous and crystalline regions. These thermoplastics have very high production rates and are used in applications such as fibers, films, packaging, plastic parts, and bottles. The study of polymer crystallization is important because the strength and elasticity depend on the fractional crystallinity, and processing parameters, such as mold pressure and cooling time, are dependent on the overall crystallization rate.^{1,2,3}

Thermodynamics predicts crystallization of small molecules very well and equilibrium conditions usually dictate the final state of the material. In polymers, the final state is usually far from equilibrium and the crystallization process is a competition between kinetic factors involved in the organization of polymer chains and the requirements of thermodynamic equilibrium. In isothermal crystallization, the

transformation from an amorphous melt begins after some specific time period, the nucleation time, during which no measurable crystallization occurs. During nucleation, growth centers form, and these growth centers provide templates for crystallization. After a growth center has formed, the polymer begins to crystallize through lamella formation in a spherulite structure. Crystal growth continues until a spherulite impinges upon another growing spherulite, another phase, or the polymer no longer has enough chain mobility for continued growth.

A theoretically derived equation for first order, heterogeneous nucleation with three-dimensional crystal growth is presented in Equation 4-1.⁴

$$\ln\left[\frac{1}{1-X_r}\right] = \frac{4}{3}\pi\frac{\rho_s}{\rho_m}N_0G^3t^3 \quad [4-1]$$

Where,

$$X_r(t) = \frac{X(t)}{X(\infty)} \quad [4-2]$$

N_0 is the total number of heterogeneous particles added to the system, G is the constant linear crystal growth rate, t is the time, and ρ_s and ρ_m are the crystalline and melt densities. For systems with one-dimensional and two-dimensional growth, the power of t and G are 1 and 2, respectively. In real polymer systems, the assumptions used in deriving Equation 1 are seldom accurate, but the derivation does give insight into the variables that effect crystallization. Avrami proposed a semi-empirical equation where the nucleation and linear growth rates are embodied in the crystallization rate constant,

K, and the dimensionality is characterized by the Avrami exponent, n, as shown in Equation 4-3.⁵

$$X_r(t) = 1 - e^{-Kt^n} \quad [4-3]$$

The Avrami exponent is rarely a whole number and is a function of both the nucleation mechanism and the dimensionality of growth, so dimensionality cannot be fully determined from kinetic data alone. Some commonly accepted guidelines state that n varies from 1 to 4 and is related to the dimensionality since the regions from 1 to 2, 2 to 3, and 3 to 4, generally indicate 1, 2, and 3 dimensional growth, respectively. After rapid crystalline growth, a pseudo-equilibrium level of crystallization is obtained. However, if the polymer remains at the isothermal crystallization temperature indefinitely, secondary crystallization will occur over very long times at an extremely slow rate.

The addition of fillers and additives to polymers has motivated new studies on the effect these modifiers have on crystallization. Glass, carbon, aramid, and cellulose fibers have been studied.^{6,7,8} In some cases, the fibers acted as nucleating agents by enhancing the nucleation density and speeding the crystallization process, while in other cases the fibers impinged upon the growing crystal, thus stopping growth in one or more dimensions. This effect is polymer specific, as the same fiber can cause an enhancement in the nucleation density in one polymer and have no influence in another.⁹ Particle size also plays a role; studies on particulate composites with fillers

such as carbon, titanium dioxide, and calcium carbonate have shown that particles under 5 μm in diameter acted as nucleating agents, while larger particles impinge growing crystals thus dampening the overall crystallization rate.^{10,11}

Although metal filled systems have been studied extensively for property changes such as enhanced thermal and electrical conductivity, rheological and mechanical properties and density,^{12,13,14} little work has been done on the effect metal has on the crystallization kinetics of semi-crystalline thermoplastic composites. Maiti et. al. studied the crystallization kinetics of polypropylene (PP) in nickel-PP composites, but this work was limited to volume fractions below 3.4 percent by volume where mechanical properties are exponentially decaying.¹⁵ All experiments on this nickel-PP system were done below the region where a continuous network of nickel particles had formed; i.e. below the percolation threshold. We are aware of no studies on metal-thermoplastic systems to determine the effect of a metal on the crystallization kinetics at concentrations equal to or above the percolation threshold. Recently, our research has focused on the characterization of conductive thermoplastic composites and has shown that in films of nickel-filled LDPE the fractional crystallinity increased with increasing filler loading under the conditions used to prepare the films.^{16,17} This work prompted us to examine the effect of the filler on the crystallization kinetics of nickel-filled LDPE composites.

4.2.2 Thermal Conductivity

The effect of fillers on the thermal conductivity of composite systems has been well documented.^{18,19} The thermal conductivity of a composite, k_c , increases with increasing filler loading. Equation 4-4 is an empirical relationship correlating thermal conductivity of a composite, k_c , to the thermal conductivities of both the filler and the polymer, k_f and k_p , the volume fraction, V , the maximum packing fraction, V_m , and the particle geometry.²⁰

$$\frac{k_c}{k_p} = \frac{1 + ABV}{1 - B\Psi V} \quad [4-4]$$

Where

$$B = \frac{\frac{k_f}{k_p} - 1}{\frac{k_f}{k_p} + A} \quad [4-5]$$

and

$$\Psi = 1 + \frac{1 - V_m}{V_m^2} V \quad [4-6]$$

Bigg has shown that the value of A , a factor related to the geometry of the system, is related to the aspect ratio for anisotropic filler particles.²¹ Progelhof, Thorne, and Ruesch have completed a review of the thermal conductivity of composite materials.²²

This work shows that in metal-filled polymer matrix composites, the network of metal particles increases the crystallization rate by increasing heat transfer during this

exothermic process. Differential-scanning calorimetry (DSC) was used to measure the isothermal crystallization rate of nickel-filled LDPE with varying nickel concentrations. In addition, the electrical and thermal conductivities were measured and compared to changes in crystallization kinetics.

4.3 EXPERIMENTAL PROCEDURES

Films of randomly cut nickel flake (Alfa Aesar), with a maximum diameter of 44 μm and an average thickness of 0.37 μm , supported by LDPE were produced by extrusion (Section 2.2.3) with varying concentrations of filler. The crystallization rate (Section 2.3.6.1), fractional crystallinity (Section 2.3.5), electrical conductivity (Section 2.5.1), and thermal conductivity ratios (Section 2.5.2) were measured as a function of nickel content. The network formation as a function of volume fraction was qualitatively examined by scanning electron microscopy (Section 2.3.4).

The melt temperature of LDPE was $105.4 \pm 1.2^\circ\text{C}$ and isothermal crystallization experiments were done at varying temperatures between 95° and 104°C . The data was fit to the Avrami equation, Equation 4-3, with the Jandel Scientific software package, Sigmaplot®, using the Marquardt-Levenberg nonlinear “best fit” algorithm.

4.4 RESULTS AND DISCUSSION

4.4.1 Electrical Conductivity

Figure 4-1 shows the percolation diagram for the nickel-filled LDPE composites and indicates that the percolation threshold of nickel is between 5 and 7.5 percent nickel by volume. This critical volume fraction is lower than in most metal-filled systems because the flakes are randomly cut and anisotropic; therefore the flakes have a higher number of contacts per particle.^{23,24} The plateau region, where a continuous network of conductive filler particles has formed, began at approximately 10 percent by volume.

4.4.2 Scanning Electron Microscopy (SEM)

SEM was used to qualitatively observe the formation of the network of nickel particles as the volume fraction of nickel increased. Micrographs (300X), shown in Figure 4-2, visually follow the percolation diagram, that is, at low volume fraction the particles are randomly distributed in the material and have a low number of contacts per particle. At the percolation threshold, indicated by the 5 and 7.5 percent nickel images, the number of contacts per particle drastically increases. At 10 and 20 percent by volume, i.e. the plateau region of electrical conductivity, almost every particle is connected to other particles in a network. SEM images also confirm the randomness of the nickel flakes' shape. The large distribution of flake sizes allows more efficient packing, thus reducing the percolation threshold. Upon closer inspection at higher

Figure 4-1 Percolation Diagram for Nickel Filled LDPE

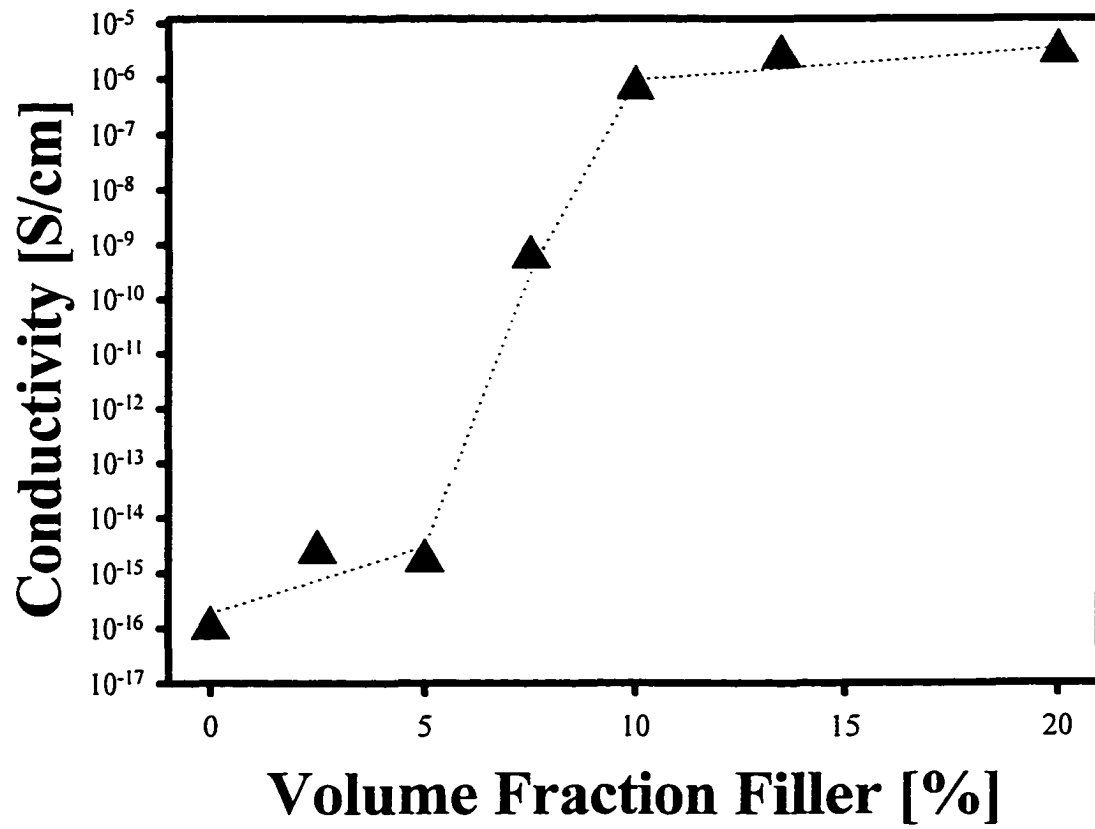
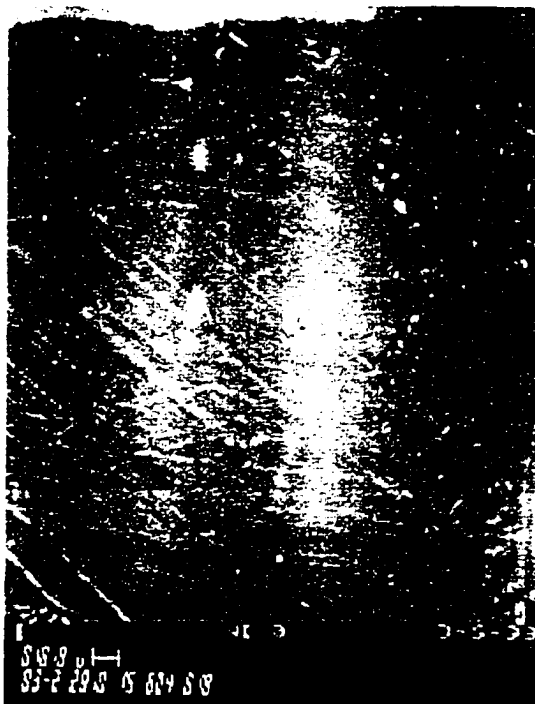


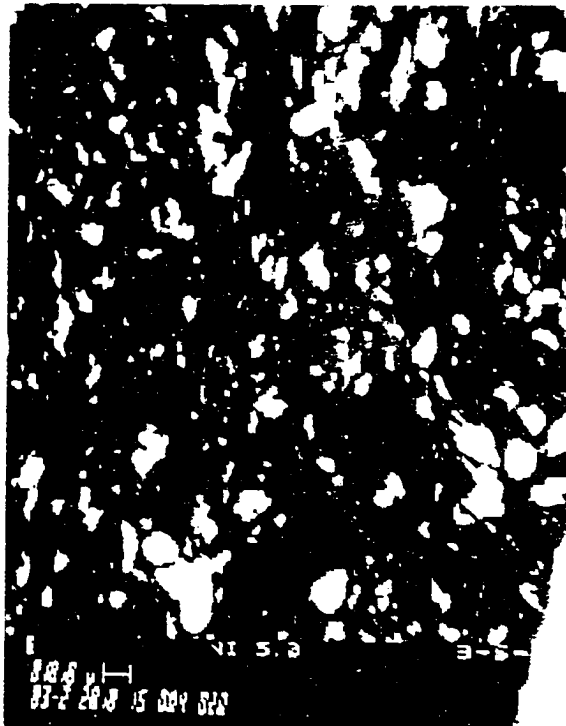
Figure 4-2 SEM Images for Nickel Filled LDPE at a Magnification of 300X



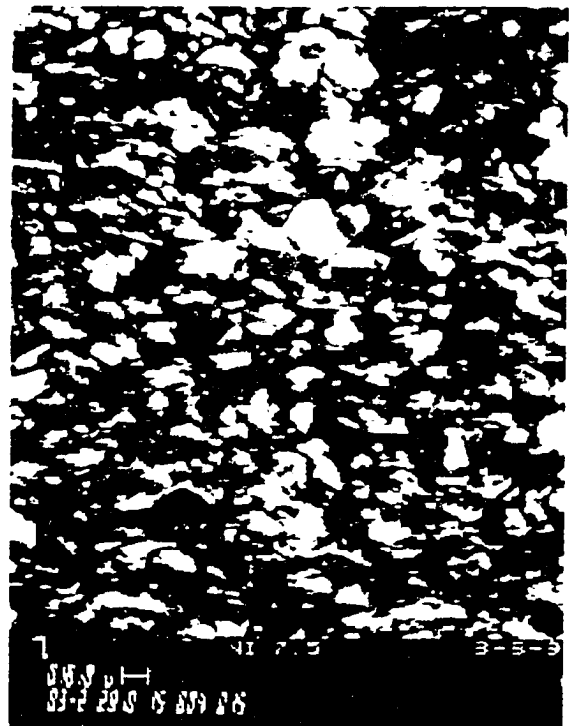
Polyethylene



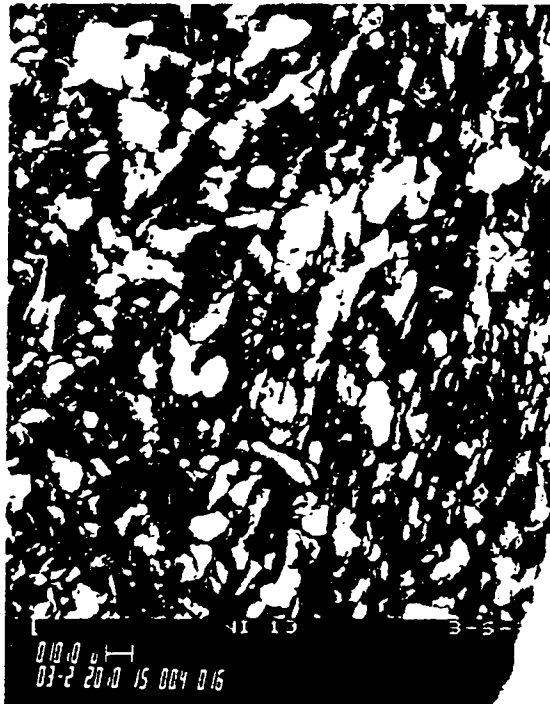
2.5 % Nickel



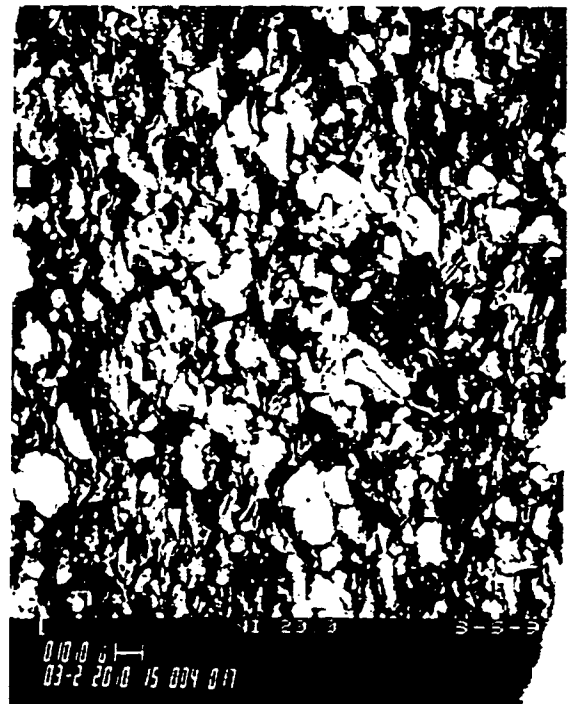
5 % Nickel



7.5 % Nickel

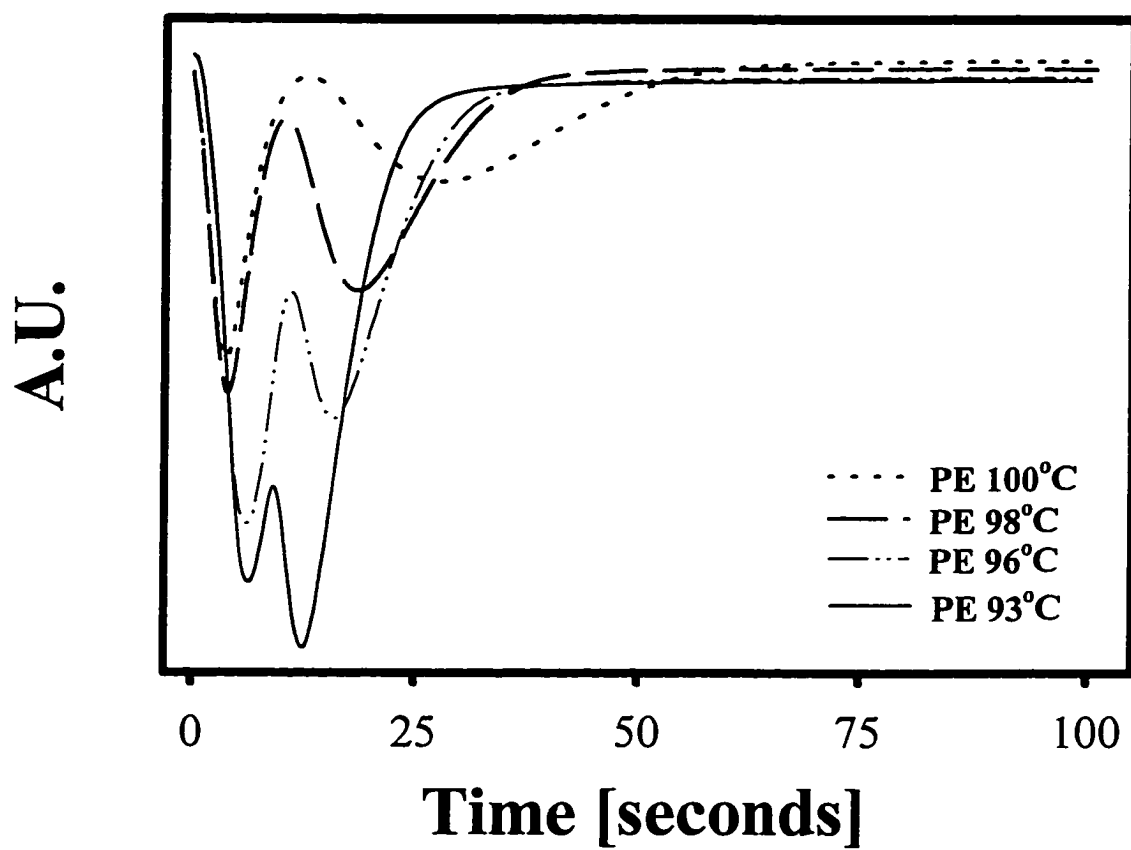


10 % Nickel



20 % Nickel

Figure 4-3 Uncorrected Crystallization Curves for PE at Various Temperatures



magnification (not shown), hook shaped regions at the edge of the flakes come together during processing to make more efficient interconnects and increase the bulk conductivity of the composites.

4.4.3 Isothermal Crystallization

Figure 4-3 shows the uncorrected isothermal crystallization curves for the material with the longest cooling time required, pure polyethylene, at temperatures of 93°, 96°, 98°, and 100°C. As the isothermal crystallization temperature decreases, the time required for cooling begins to overlap with the beginning of crystallization and isothermal crystallization is not achieved. Only a small amount of crystallization occurs for temperatures above 95°C; before the sample reaches the isothermal crystallization temperature, thus, this study was limited to temperatures between 95° and 104°C.

Figure 4-4 shows the isothermal crystallization rate of LDPE as a function of time for 2.5, 5, 10, and 20 percent nickel by volume at a 100°C. The nucleation time, i.e. the time corresponding to the onset of crystallinity, decreases as the concentration of filler increases. The higher slope between 0 and 90 percent relative crystallinity for materials with more nickel indicates a faster crystallization rate. Finally, at higher nickel contents, the curves terminate more abruptly. The first two effects can be explained by an increase in thermal conductivity of the composite, while the abrupt termination is probably due to impingement by nickel particles.

Crystal growth is an exothermic process, and any set of conditions that increase the heat transfer rate would be expected to increase the rate of nucleation and the linear

growth rate, G . The Avrami crystallization rate constant was used to quantify the increase in the rate of crystallization as shown in Figure 4-5. As expected, for a given nickel loading there was a slight increase in the Avrami rate constant, K , with temperature, but this change was much smaller than that due to the increase in filler volume fraction. In fact, K increases sharply between 7.5 and 10 percent nickel by volume, which is the same volume fraction that corresponds to the beginning of the plateau region in electrical conductivity.

The thermal conductivity ratio, calculated from Equations 2-13 and 2-14 (Figure 4-6(a)), also increased monotonically with increasing filler loading. The data was fit using Equation 4-4; the best-fit value of A was 12.05 with V_m being set at 0.52. V_m was fixed at this value because the nickel flakes were randomly oriented and anisotropic.²¹ According to the correlation given by Bigg, this value of A corresponds to an average aspect ratio of approximately 8.²⁰ In Figure 4-6(b), the ratio $(K_c/K_p)^{1/3}$ represents the ratio of linear growth rates for the composite and polymer, G_c/G_p . At low volume fractions, the growth rate ratio follows the thermal conductivity, but G_c/G_p increases much more rapidly than the thermal conductivity above the critical region. In fact, complete network formation appears to cause a very steep jump in growth rate. The continuous network of nickel particles at high concentrations may cause increased local heat transfer as the energy is more efficiently dissipated. In other words, as the concentration of filler is increased, local temperature gradients caused by the heat of fusion of the polymer chains will be reduced.

Figure 4-4 Crystallization as a Function of Volume Fraction for 2.5, 5, 10, and 20 Percent Nickel Filled LDPE

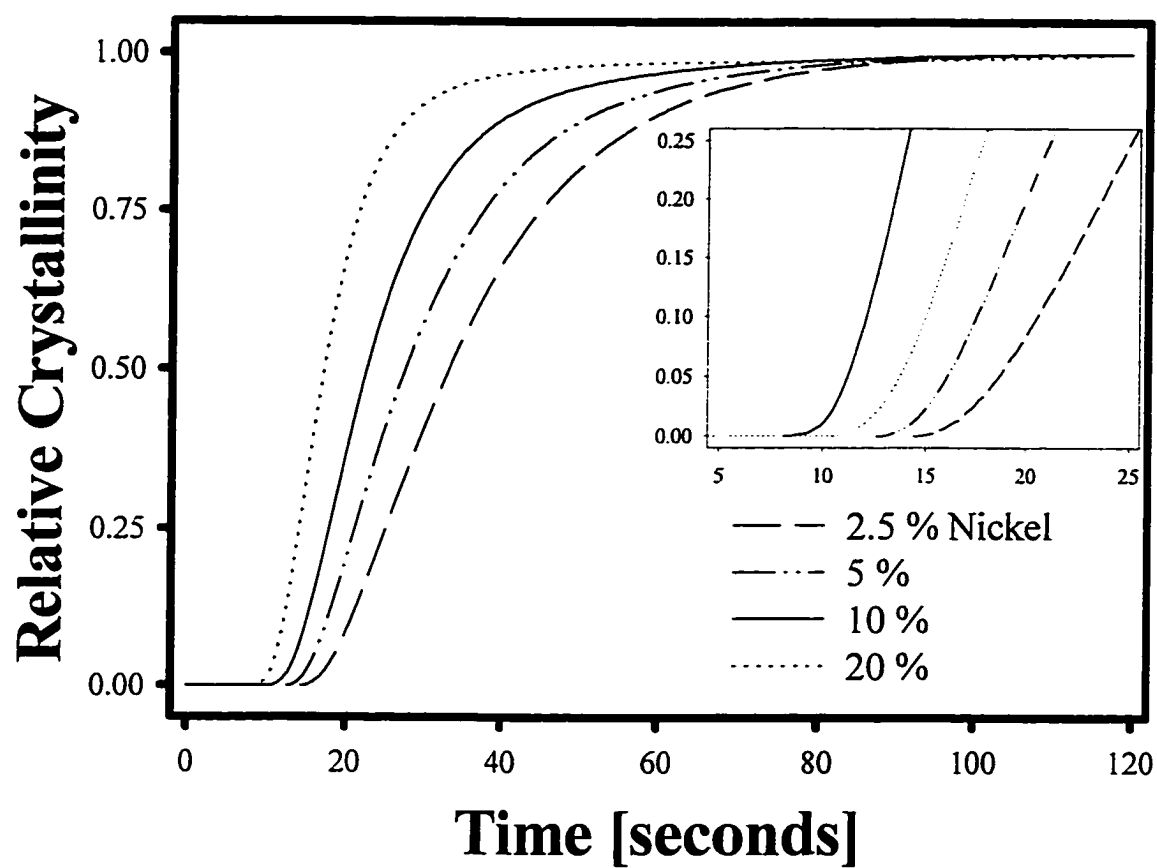


Figure 4-5 Avrami Rate Constant, K , as a Function of Temperature and Nickel Content in Nickel Filled LDPE

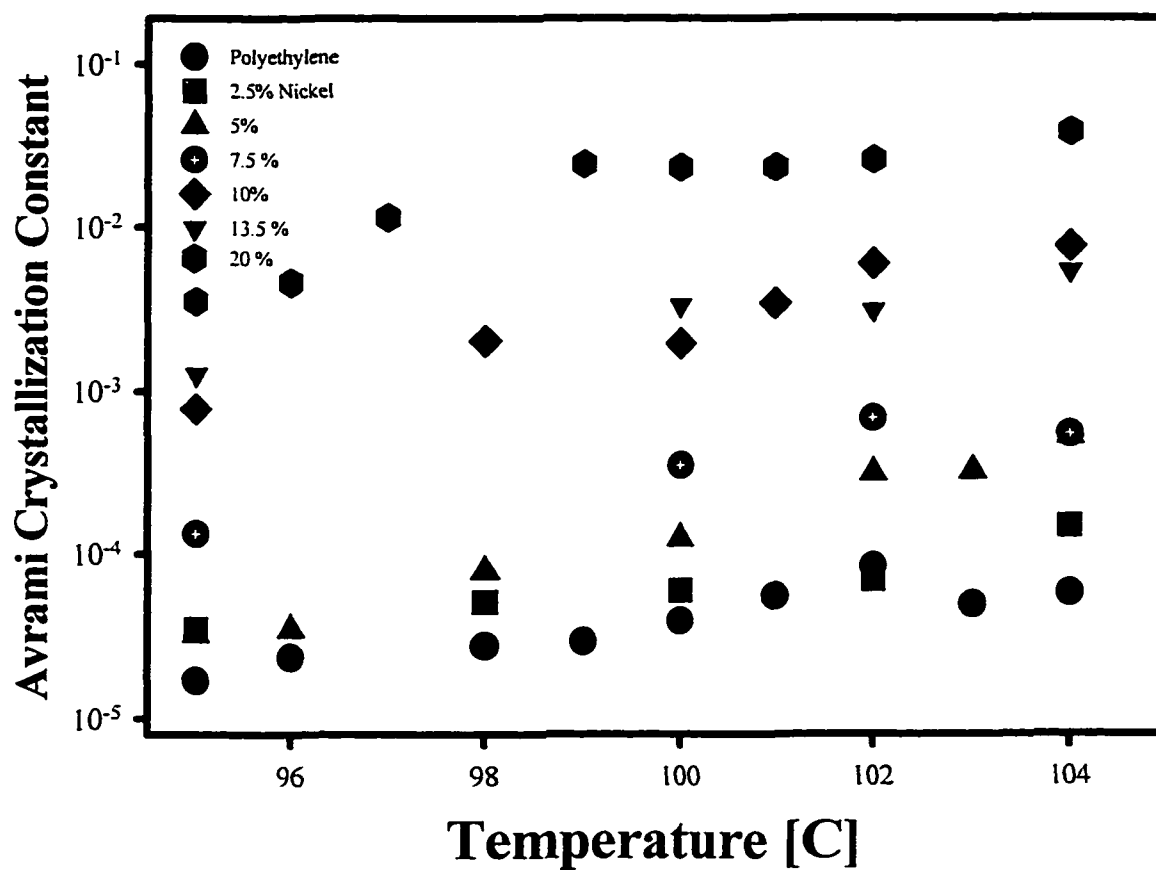


Figure 4-7 shows the crystallization kinetics for a composite made with silica, which has a similar thermal conductivity to the thermal conductivity of the polymer. The addition of silica decreased the overall crystallization rate; actually slightly impeding crystallization. As expected, without the increased thermal conductivity, no increase in crystallization rate was observed.

The Avrami exponent, shown in Figure 4-8, was not sensitive to nickel volume fraction, thus indicating that the dimensionality was not changed by the presence of the filler. Since the Avrami exponent depends on the mechanism of nucleation, the invariance of n with the addition of nickel indicates that nucleation was not the source of the increased crystallization rate. In fact, for particulates with sizes similar to the nickel used in this study, the overall crystallization rate is usually slowed by the addition of filler consistent with the results presented for the silica-filled composites. Therefore, the increase in crystallization rate is due to an increase in the linear growth rate, G . Because crystallization is exothermic, the improved heat transfer provided by the nickel particles is the cause of this increase in linear growth rate. This work demonstrates that the increase in crystallization rate is greatest for materials where a continuous network of high thermal conductivity filler has formed.

4.4.4 Fractional Crystallinity

This study of crystallization kinetics in metal-filled composites was motivated by

Figure 4-6 Heat Transfer Effects; a) Thermal Conductivity Ratio, k_c/k_p ([▲] Experimental Data; [---] Nielsen's Model; b) Avrami Rate Constant Ratio, $(K_c/K_p)^{1/3}$, which Corresponds to the Ratio of the Linear Growth Rates, G_c/G_p ([■] Experimental Data; [---] Nielsen's Model (for isothermal crystallization at 100°C)

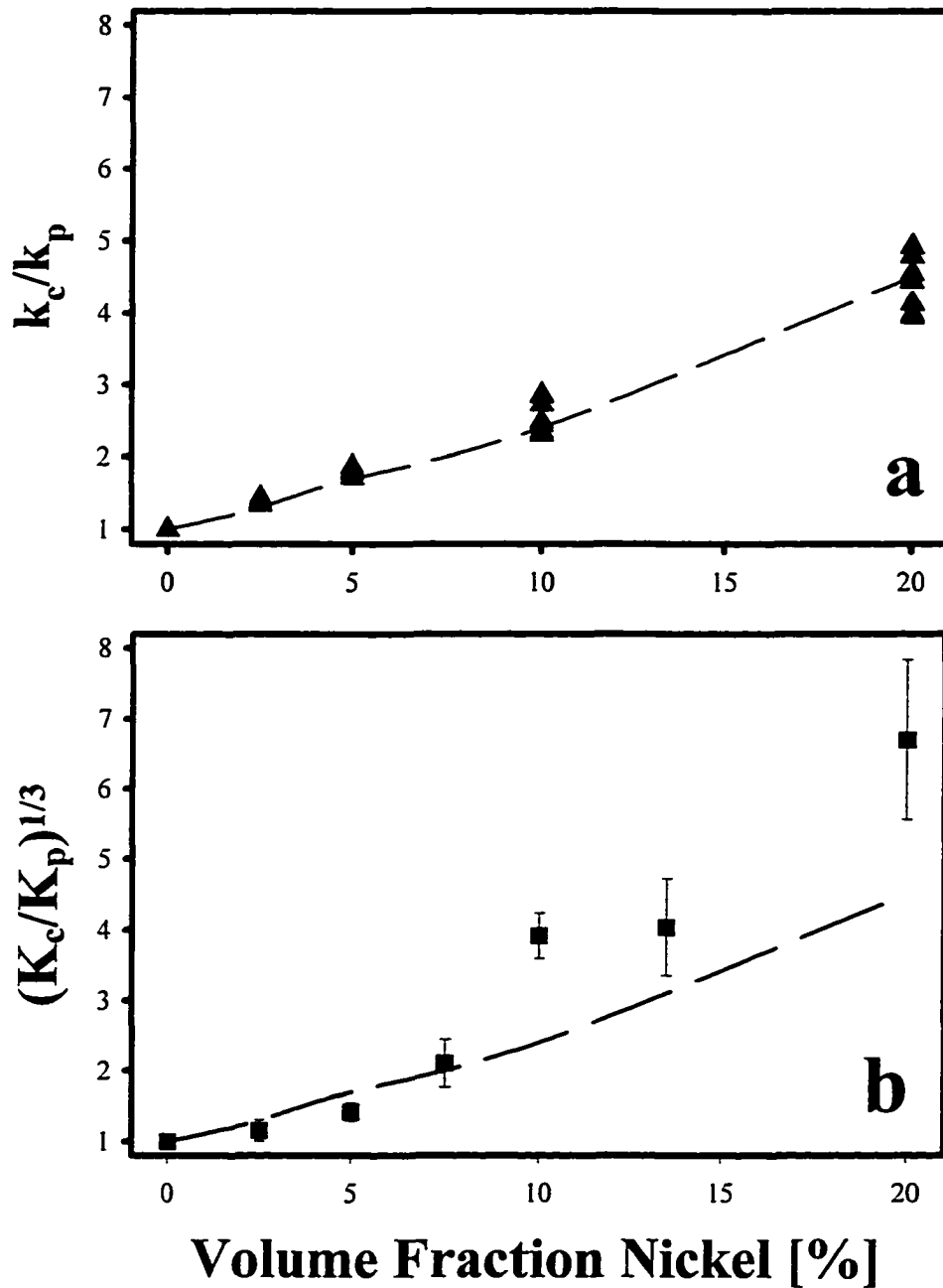


Figure 4-7 Crystallization as a Function of Volume Fraction for 5, 10, 15, and 20 Percent Silica Filled LDPE (isothermal crystallization temperature was 100°C)

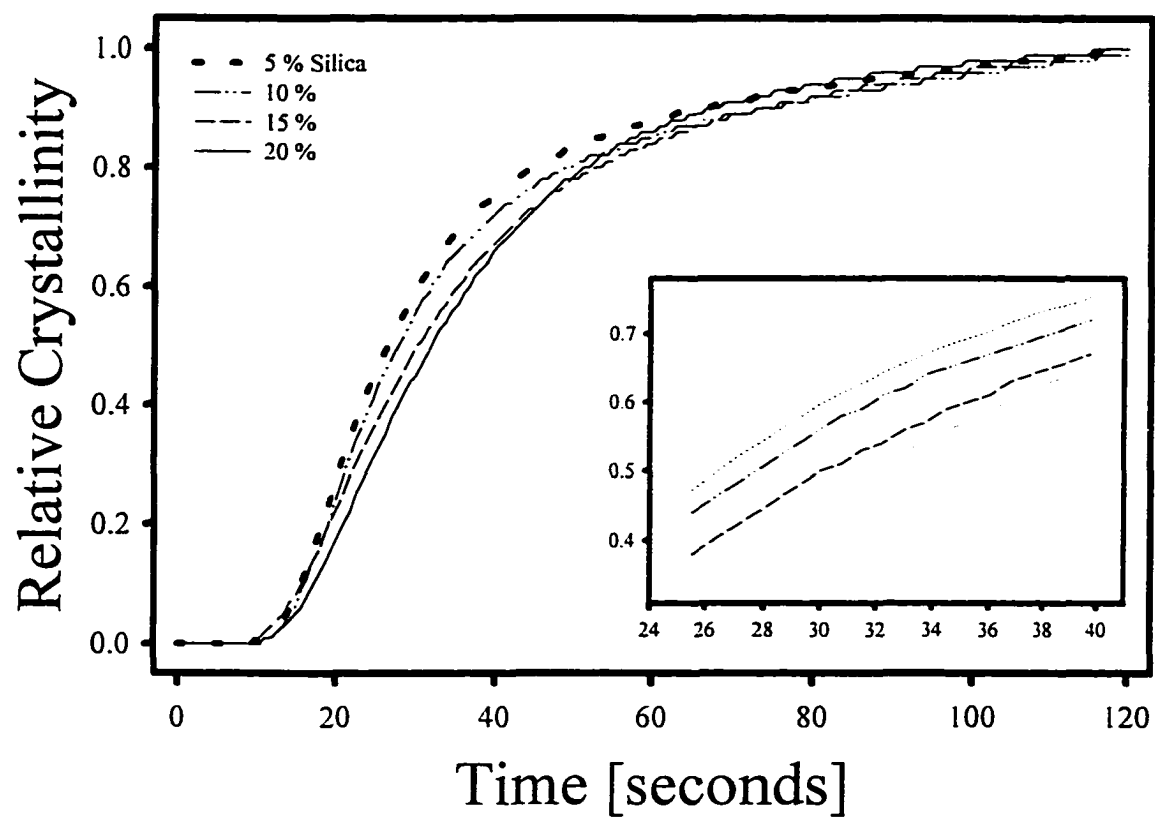
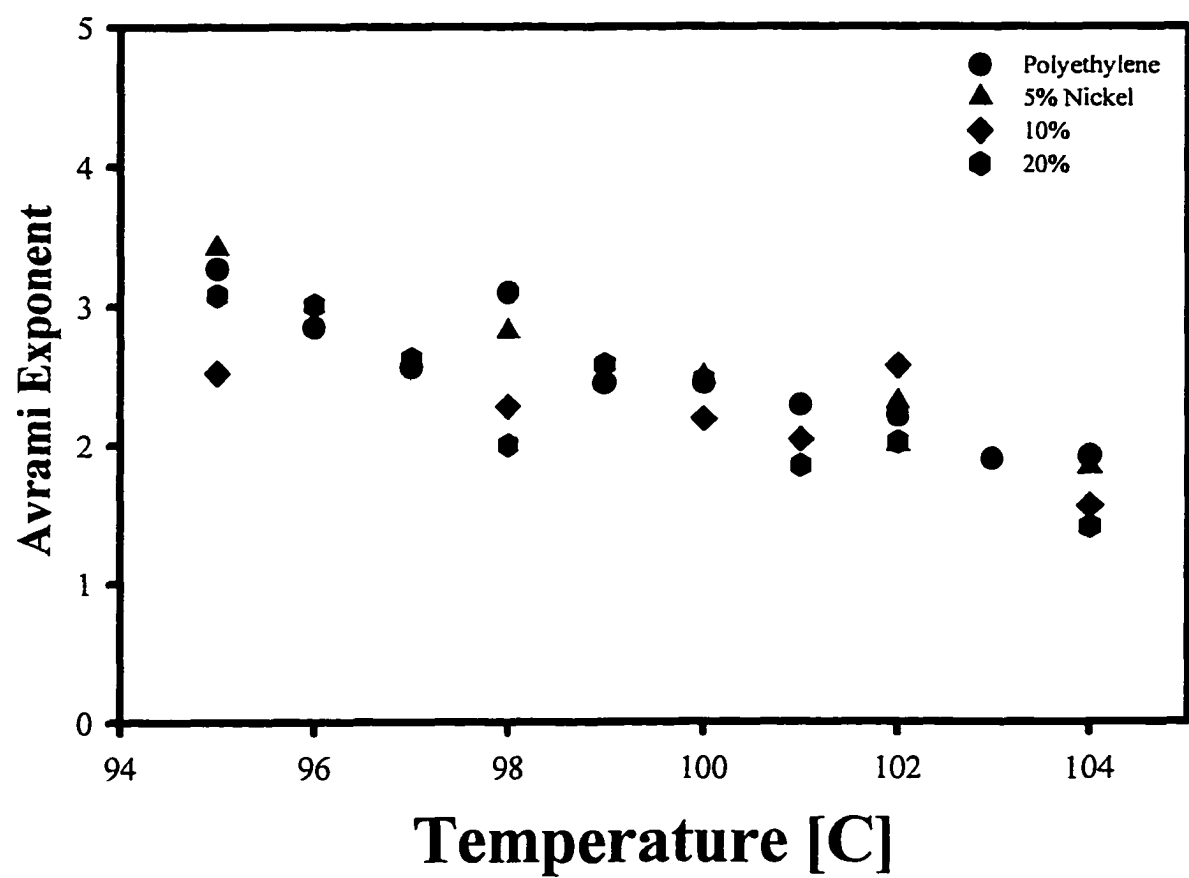


Figure 4-8 Avrami Exponent, n , as a Function of Temperature and Concentration in Nickel Filled LDPE



the increase in the fractional crystallinity in extruded composite films [see Figure 4-9(a)]. As shown in Figure 4-9(b), the addition of nickel to the LDPE did not have a significant effect on the fractional crystallinity in these high temperature, isothermal crystallization experiments; instead, the crystallization rate increased. This difference is almost certainly due to the difference in the rapid cooling, non-isothermal conditions of film extrusion versus the isothermal conditions of a DSC crystallization experiment. Both observations are almost certainly due to the same underlying phenomena: the increased heat transfer of the composite relative to the polymer resulting from the addition of the nickel particles.

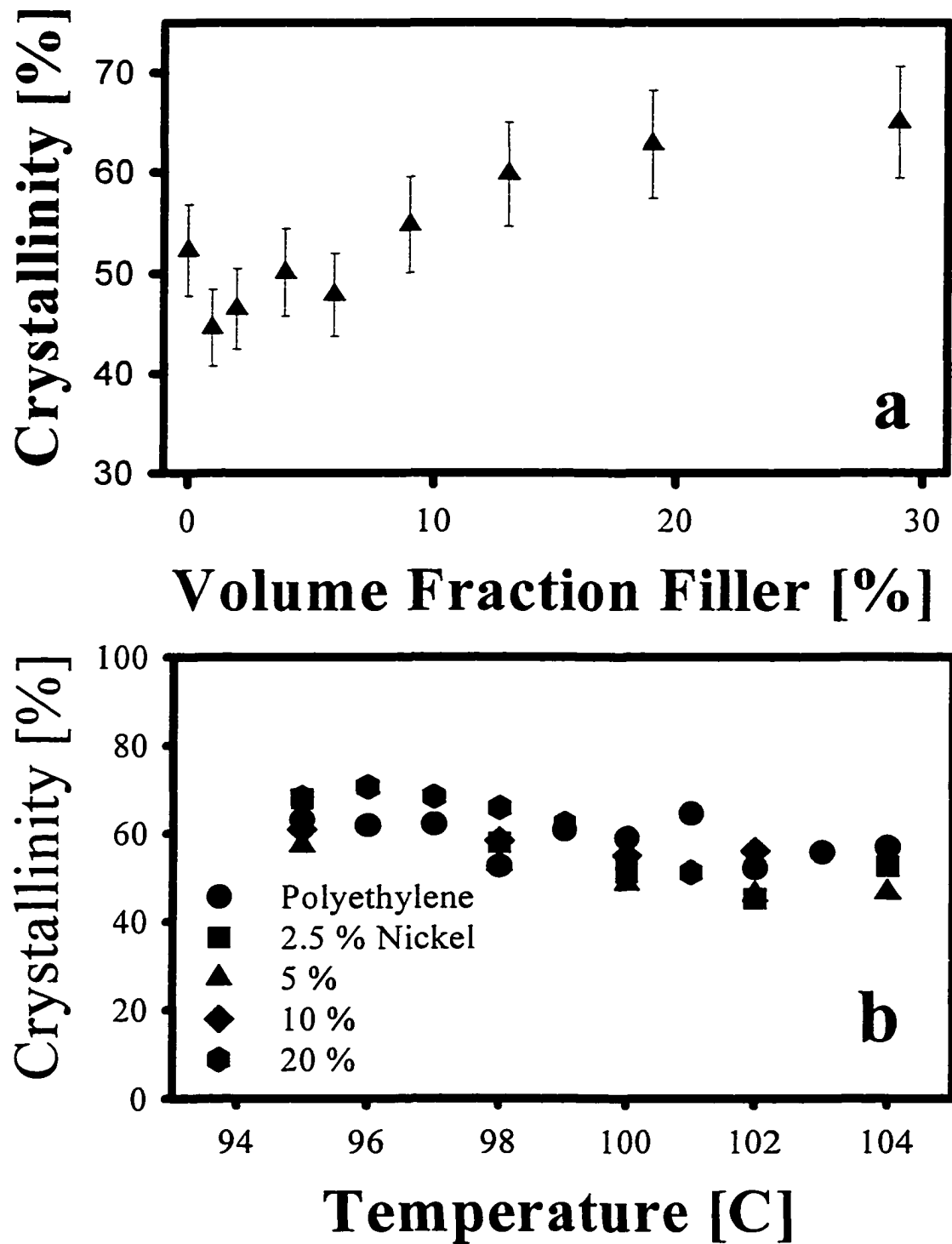
The fractional crystallinity actually decreased slightly with increasing temperature in the isothermal crystallization experiments. From thermodynamics, the fractional crystallinity should increase with increasing isothermal crystallization temperature. However, crystallization kinetics were followed in the initial time period of crystallization and only a quasi-equilibrium was reached. Since secondary crystallization was not examined, the counter-intuitive lower fractional crystallinity at higher crystallization temperatures might have resulted.

4.5 CONCLUSIONS

We have shown that the network of nickel particles described by percolation statistics, used to characterize the electrical conductivity, is also important in determining crystallization kinetics. A large jump in electrical conductivity over a very

short range of concentration occurs when the first continuous pathways of nickel particles form; complete network formation corresponds to the plateau region in electrical conductivity. In crystallization, complete network formation causes a sharp increase in linear crystal growth rate, much larger than the bulk thermal conductivity would predict. We believe that complete network formation causes the energy released during crystallization to be more effectively removed in a microscopic sense. The continuous network of nickel particles dissipates the heat of crystallization, thus allowing crystallization to occur more rapidly.

Figure 4-9 Fractional Crystallinity; a) As a Function of Nickel Concentration for Extruded LDPE Composite Films; b) As a Function of Temperature and Nickel Volume Fraction in Isothermally Crystallized LDPE Composite Films



4.6 NOMENCLATURE

X_r	Relative crystallinity
ρ_s	Crystalline density
ρ_m	Melt density
$X(t)$	Fractional crystallinity as function of time
t	Time
$X(\infty)$	Final fractional crystallinity
N_0	Number of particles added to the system
G	Linear growth rate
K	Avrami rate constant
n	Avrami exponent
k_c	Composite thermal conductivity
k_p	Polymer thermal conductivity
k_f	Filler thermal conductivity
V	Volume fraction
V_m	Maximum packing fraction
A	Neilson geometric constant
B	Empirical parameter defined by Equation 4-5
ψ	Empirical parameter defined by Equation 4-6

4.7 REFERENCES

- 1 J. D. Hoffman and R. L. Miller, *Polym.*, **38**, 3151, (1997).
- 2 W. Banks, M. Gordon, R. J. Roe, and A. Sharples, *Polymer*, **4**, 61, (1963).
- 3 V. Erukhimovitch and J. Baram, *Phys. Rev. B.*, **9**, 5854, (1994).
- 4 L. Mandelkern, Crystallization of Polymers, McGraw-Hill Book Company, New York, NY, 229, (1964).
- 5 A. Kumar and R. K. Gupta, Fundamentals of Polymers, McGraw Hill, New York, 349, 1998.
- 6 H. J. Tai, W. Y. Chu, L. W. Chen, and L. H. Chu, *J. Appl. Polym. Sci.*, **42**, 3111, (1991).
- 7 V. E. Reinsch, and L. Rebenfeld, *Polym. Comp.*, **13**, 353, (1992).
- 8 D. T. Quillin, M. Yin, J. A. Koutsy, and D. F. Caulfield, *J. Appl. Polym. Sci.*, **52**, 605, (1994).
- 9 N. A. Mehl, and L. Rebenfeld, *J. Appl. Polym. Sci.*, **57**, 187, (1995)
- 10 G. Groeminck, H. Berghmans, and N. Overbergh, *J. Polym Sci. Polym. Phys.*, **12**, 303, (1974).
- 11 S. Cheng and R. A. Shanks, *J. Appl. Polym. Sci.*, **47**, 2149, (1993).
- 12 D. M. Bigg, *Polym. Eng. Sci.*, **19**, 1188, (1979).
- 13 J. Gurland, *Trans. Met. Soc.*, **236**, 642, (1966).
- 14 S. M. Aharoni, *J. Appl. Phys.*, **43**, 2463, (1972).

- 15 S. N. Maiti, and P. K. Mahapatro, *J. Appl. Polym. Sci.*, **37**, 1889, (1989).
- 16 W. B. Genetti, W. L. Yuan, B. P. Grady, E. A. O'Rear, C. L. Lai, and D. T. Glatzhofer, *J Mater. Sci.*, **33**, 3085, (1998).
- 17 W.B. Genetti, B.P. Grady, and E.A. O'Rear, in Electronic Packaging Materials Science IX, Vol. 445, S.K. Groothuis, P.S. Ho , K. Ishida, and T. Wu, editors,,: Materials Research Society, Pittsburgh, PA, 153, 1997.
- 18 S. K. Bhattacharya, Metal-Filled Polymers: Properties and Applications, M. Dekkar, Inc., New York, 252, 1986.
- 19 Y. Agari, A. Ueda, M. Tanaka, and S. Nagai, *J. Appl. Polym. Sci.*, **40**, 929, (1990).
- 20 L. E. Neilsen, *Ind. Eng. Chem., Fundam.*, **13**, 17, (1974).
- 21 D. M. Bigg, *Polymer Composites*, **7**, 125, (1986).
- 22 R. C. Progelhof, J. L. Throne, and R. R. Ruetsch, *Polym. Eng. Sci.*, **16**, 615, (1976).
- 23 S.M. Aharoni, *Journal of Applied Physics*, **43**, 2463 (1972).
- 24 K. Miyasaka, K. Watanabe, E. Jojima, H. Aida, M. Sumita, K. Ishikawa, *Journal of Materials Science*, **17**, 1610 (1982).

CHAPTER 5

POLYMER MATRIX COMPOSITES: CONDUCTIVITY ENHANCEMENT THROUGH POLYPYRROLE COATING OF PARTICULATES

5.1 INTRODUCTION

The electrical resistance of polymeric materials loaded with conductive fillers can be divided into three major categories: the intrinsic resistance of the filler and matrix, the particle-particle contact resistance, and the tunneling resistance. A method for decreasing both the particle-particle contact and tunneling resistance in particulate filled low density polyethylene (LDPE) composites which involves modifying the particle surface by the addition of an ultrathin polypyrrole (PPy) film by admicellar polymerization has been developed. This method has been applied to nickel flakes, alumina, and glass fibers: which represent conductive, resistive, and insulating particulates, respectively. It is believed that these resistances are reduced by the formation of PPy “molecular wires” which occur as a result of chain entanglements at high filler loading. Coating the particulates with PPy leads to an increase in conductivity at concentrations above the percolation threshold without significantly

changing the thermal or mechanical properties of the composite. The inherent loss in conductivity with stretching was reduced by the PPy surface modification and the “molecular wire” theory can also explain this phenomenon.

5.2 BACKGROUND AND LITERATURE REVIEW

Due to the importance of the polymer-filler interactions on the physical properties of the polymer matrix composite, modification of the filler surface can lead to changes in the overall properties. Previous studies indicate that the surface of inorganic particulates, such as silica, alumina, titanium dioxide, or copper oxide, can be modified by the addition of conductive polymer films inducing changes in the overall conductivity and/or surface morphology.^{1,2,3} Because most conductive polymers are intractable, the films are formed by polymerization on the surface of the particulate by techniques such as electrochemical oxidation, chemical initiation or chemically initiated polymerization on surfaces with oxidative sites.^{4,5,6} The addition of ultrathin, electrically conductive polymer films changes the nature of the interaction between the particles, thus effecting the physical properties of the composite.

Others have reported changes in specific mechanical properties of particulate-filled polymer-matrix composites through the modification of the filler surface. For example, methacrylate and epoxy functional silane coupling agents have been used to modify clay, wollastonite, and quartz particulates in polyolefin composites.⁷ The composites with the coupling agents have higher moduli, stiffness, and strength-to-weight ratios

than composites made from the unmodified fillers. Mechanical strengths of polymer-matrix composites with inorganic particulate fillers, such as silica, have also been enhanced by the addition of an ultrathin coating added by admicellar polymerization. The ultrathin polymer film apparently makes the filler more compatible with the polymer host by building a bridge of physical bonds between the filler and the matrix.⁸ This study reports the increase in electrical conductivity above the percolation threshold due to the addition of an ultrathin conducting polymer film on the filler surface. To date, we are aware of no prior studies of increasing the conductivity of particulate filled polymer-matrix composites above the percolation threshold by this type of surface modification.

Many processing techniques, such as profile extrusion, film blowing, or calendaring, stretch or orient the polymer. As the conductive composites are stretched, the filler particles are pulled apart and the conductive pathways are broken, resulting in a decreased conductivity.⁹ In systems with anisotropic filler particles, the initial stretching induces a slight increase in conductivity as the filler particles become aligned then decreases exponentially as the filler particles are pulled apart.¹⁰

Ultrathin polymer films are often used to change the surface of a substrate in order to enhance properties such as adhesion to another material or corrosion resistance. Other possible applications for materials modified with ultrathin coatings include chromatographic packing, inorganic core ion exchange resin, and substrates for immobilized hydrophobic enzymes.¹¹ One recently introduced mechanism to add an ultrathin film to a substrate is termed admicellar polymerization.³ Polypyrrole (PPy)

has been shown to form ultrathin conductive films on the surface of both plate and particulate substrates through admicellar polymerization.¹² This paper expands this technology by modifying fillers that are conductive, resistive, and insulating and determining the effect on the conductivity of a thermoplastic composite made with the modified filler.

5.2.1 Admicellar Polymerization

Admicellar polymerization can be visualized as the two-dimensional surface analogue of emulsion polymerization with the micelle being replaced by a surfactant bilayer. There are four steps in this process: admicelle formation, monomer solubilization, initiation and polymerization, and washing. A schematic representation of the four steps is shown in Figure 5-1 and described briefly below.

5.2.1.1 Admicelle Formation

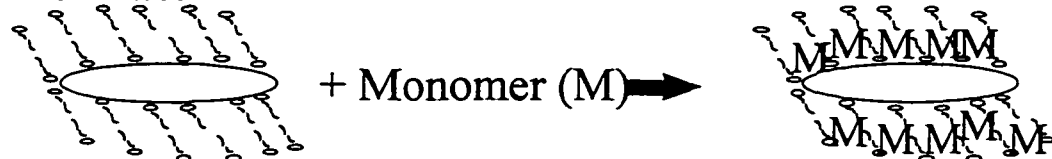
A bilayer of surfactant, called an admicelle, is adsorbed on the surface of the substrate in water. The pH of the solution is adjusted so that the head groups of a surfactant are attracted and held to the substrate surface. An adsorption isotherm is a plot of the surfactant adsorption as a function of concentration in solution at a constant temperature and is shown schematically in Figure 5-2. In Region I, only random adsorption of surfactant molecules occurs on the surface of the substrate. As concentration of surfactant increases, more structured adsorption occurs as the heads of

Figure 5-1 Schematic Diagram of the Admicellar Polymerization Process

1. Admicelle Formation



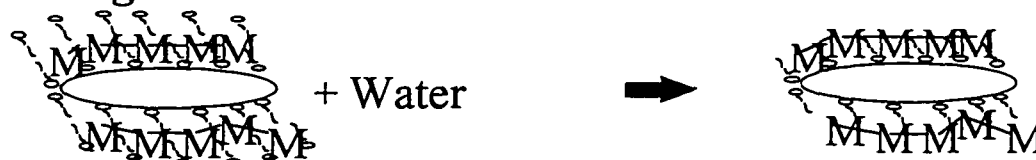
2. Solubilization



3. Polymerization



4. Washing



the surfactant are attracted to the surface and the tails draw towards each other, but uniform coverage of the surface is not attained in Region II. In Region III, a uniform bilayer of surfactant molecules has formed on the surface. In region IV, no more surfactant adsorbs to the surface of the substrate; in many cases the transition between Regions III and IV corresponds to the critical micelle concentration (cmc) where micelles first begin to form in solution. It is important that micelles do not form in solution so as to prevent emulsion polymerization. To perform an admicellar polymerization, the surfactant concentration must be below the critical micelle concentration, but sufficiently high to favor admicelle formation on the particle surface.

5.2.1.2 Solubilization

After the surfactant bilayer has formed on the substrate's surface, hydrophobic monomer is added to the solution. The monomer partitions to the adsorbed bilayer.

5.2.1.3 Polymerization

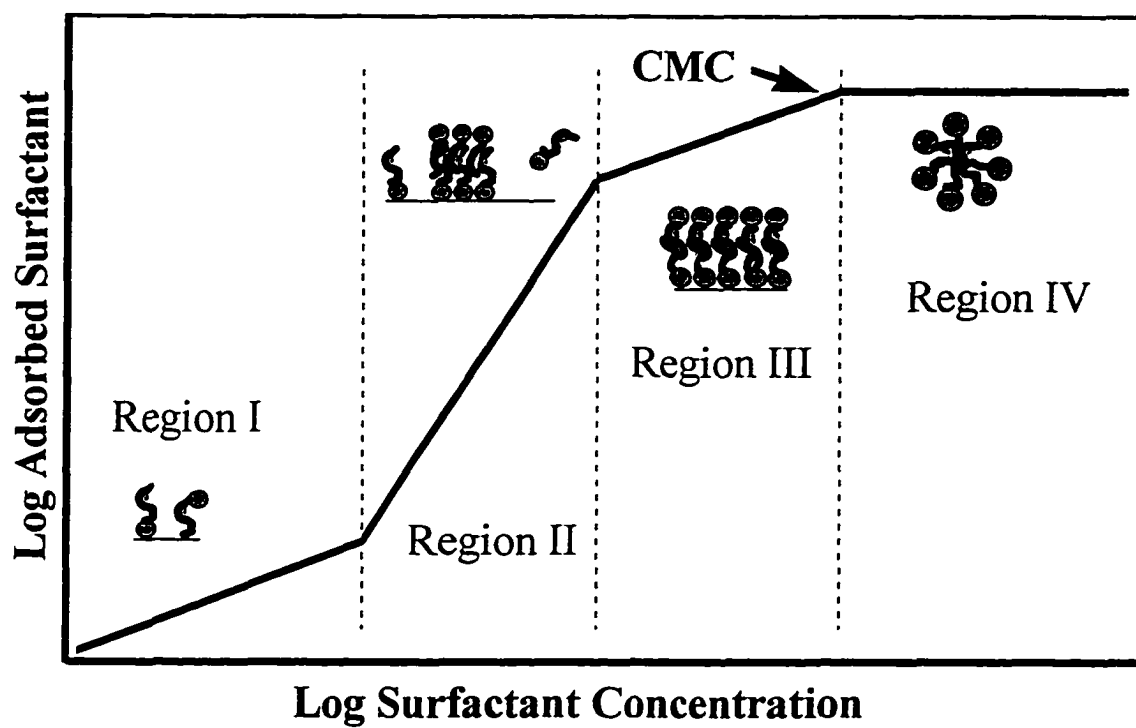
The polymerization reaction is initiated with a water-soluble initiator.

5.2.1.4 Washing

After polymerization, the modified particulates are collected and washed to remove the outer layer of surfactant.

Admicellar polymerization has been performed on silica, glass fibers, nickel, and

Figure 5-2 Schematic Diagram of an Adsorption Isotherm



alumina with monomers such as styrene, ethylene, propylene, tetrafluorethylene and pyrrole. The kinetics of the admicellar polymerization reaction have been studied and modeled by Wu *et al.*¹³ An in-depth study of solubilization and adsolubilization was done by Funkhouser *et al.*³ Articles based on the work presented in this chapter have been published by our research group.^{10,12,14,15}

In this study, the surface of nickel flakes, alumina, and glass fibers were modified by the addition of polypyrrole (PPy), an intrinsically conductive polymer, by admicellar polymerization. The nickel flake was characterized by both an optical microscope and scanning tunneling microscopy (STM) in order to determine the nature of the coating. Both the fillers and the modified fillers were incorporated into a low-density polyethylene (LDPE) matrix and the electrical conductivity of the samples was measured as a function of concentration. The effect of processing on the conductivity of the composites was determined by preparing samples by both solution casting and extrusion, as well as testing the conductivity as a function of draw ratio for the solution cast composites. In addition, the tensile properties of the LDPE and fractional crystallinity of the composite were also determined.

5.3 EXPERIMENTAL PROCEDURES

5.3.1 Adsorption Isotherm

In all cases, an ionic surfactant, sodium dodecyl sulfate (Aldrich) was used. The pH of the water solution was adjusted to be below the point of zero-charge for each

substrate and is listed in Table 5-1. Adsorption isotherms for nickel flake (Sigma) and glass fibers (Owens Corning, Fiberglas Reinforcements) were measured; the adsorption isotherm for alumina (DeGussa) has already been published.³ Solutions of sodium dodecyl sulfate (SDS) from 1000 to 12000 μM were prepared for the adsorption isotherm measurements and as standards for HPLC calibration. Four grams of nickel flake or two grams of glass fibers was placed in 30 milliliters of solution for each concentration and allowed to equilibrate for 24 hours. A Shimadzu 10-A HPLC with a Waters 486 tunable UV absorption detector was used to measure the final concentration of SDS in solution. The SDS adsorbed per gram of substrate was determined from the difference in the concentration between the standard solution and the solution, which contained the sample.

5.3.2 Admicellar Polymerization

Admicellar polymerization was performed on nickel flake, alumina, and glass fibers at the conditions specified in Table 5-1. Surfactant concentrations were adjusted so that polymerizations took place in Region III of the isotherm. The pH of the solution was adjusted to the desired value using hydrochloric acid and SDS was allowed to adsorb on the surface for 24 hours. Pyrrole (Aldrich) was filtered through a packed bed of basic alumina, added to the reaction, and given 24 hours to solubilize into admicelles. Sodium persulfate (Aldrich) was used to initiate the oxidative reaction at a molar ratio of pyrrole to initiator of 1:1. The reaction was carried out for 24 hours at 25°C to

ensure completion. Particulates were collected by vacuum filtration and washed with water, then air dried for 24 hours prior to vacuum oven drying at 70°C for an additional 24 hours.

5.3.3 Particulate Characterization

Samples of both the filler and surface modified filler were placed in a Linburg Hevi-Duti Furnace overnight at 800°C to remove the PPy-coating by burning. The samples were weighted in a Mettler H31AR Balance before and after burning. Assuming the oxidation was the same for both samples, the weight fraction of PPy was determined from a mass balance.

Images of the uncoated and coated particles were compared using an optical microscope and scanning tunneling microscopy (STM) and current imaging tunneling spectroscopy (CITS), as outlined in Sections 2.3.2 and 2.3.3, respectively.

5.3.4 Film Preparation

The volume fraction of filler, V , was determined from the filler weight fraction and the density of both phases as shown in Equation 5-1.

$$V = \frac{\frac{w_F}{\rho_F}}{\frac{w_F}{\rho_F} + \frac{1 - w_F}{\rho_P}} \quad [5-1]$$

Where w_F is the filler weight fraction, and ρ_F and ρ_P are the densities of the filler and matrix, respectively. For the PPy-coated composites, the volume of PPy is accounted for as shown in Equation 5-2.

$$V = \frac{\frac{w_F}{\rho_F} + \frac{w_{PPy}}{\rho_{PPy}}}{\frac{w_F}{\rho_F} + \frac{w_{PPy}}{\rho_{PPy}} + \frac{1 - w_F}{\rho_P}} \quad [5-2]$$

Where the weight fraction of PPy, w_{PPy} , was determined as outlined in Section 5.3.3 and ρ_{PPy} is the density of polypyrrole.

Composite films were produced using solution casting (Section 2.1.1), extrusion (Section 2.2.2), and powder mixing (Section 2.2.3). The solvent used for LDPE in this study was xylene. Uniaxial stretching was performed by the method described in section 2.2.4.

5.3.4 Characterization

Conductivity, tensile properties, and fractional crystallinity were measured using the procedures in Section 2.4.1, 2.4.3, and 2.3.5, respectively.

Table 5-1 Polymerization Conditions

Filler	SDS [μM]	Pyrrole [mM]	pH	Filler [g/L]
Nickel Flake	7500	20	4	50
Alumina	11000	76	3	30
Glass Fibers	4250	8	3	40

5.4 RESULTS AND DISCUSSION

5.4.1 Adsorption Isotherms

Figure 5-3 shows the adsorption isotherm for the nickel flake. Region III adsorption was approximately 17 μmol s per gram of nickel flake corresponding to a final SDS concentration in solution of 6600 μM . Data in the plateau region of adsorption was quite scattered and repeated testing did not remove the scatter from the data. The same amount of scatter was not seen in either the glass fibers (Figure 5-4) or alumina and may be a result of non-uniform particle areas in the randomly cut flakes.

The adsorption isotherm for the glass fibers showed a Region III adsorption of approximately 8 μmol s per gram of glass fibers corresponding to a final concentration of 3900 μM in solution after adsorption. Alumina adsorbed approximately 300 μmol s of SDS per gram of alumina corresponding to a final SDS concentration of 400 μM . Differences in adsorption are due to the difference in surface areas of the substrates. The surface area of alumina is approximately 100 m^2/g as a result of porosity. Nickel flake and glass fibers are non-porous and have a much smaller surface area per gram of material and hence much less SDS can absorb. Therefore, the polymer coating on the nickel flake and glass fibers will be completely on the outside of the substrate and much less pyrrole is needed.

Figure 5-3 Adsorption Isotherm of Sodium Dodecyl Sulfate on Nickel Flake

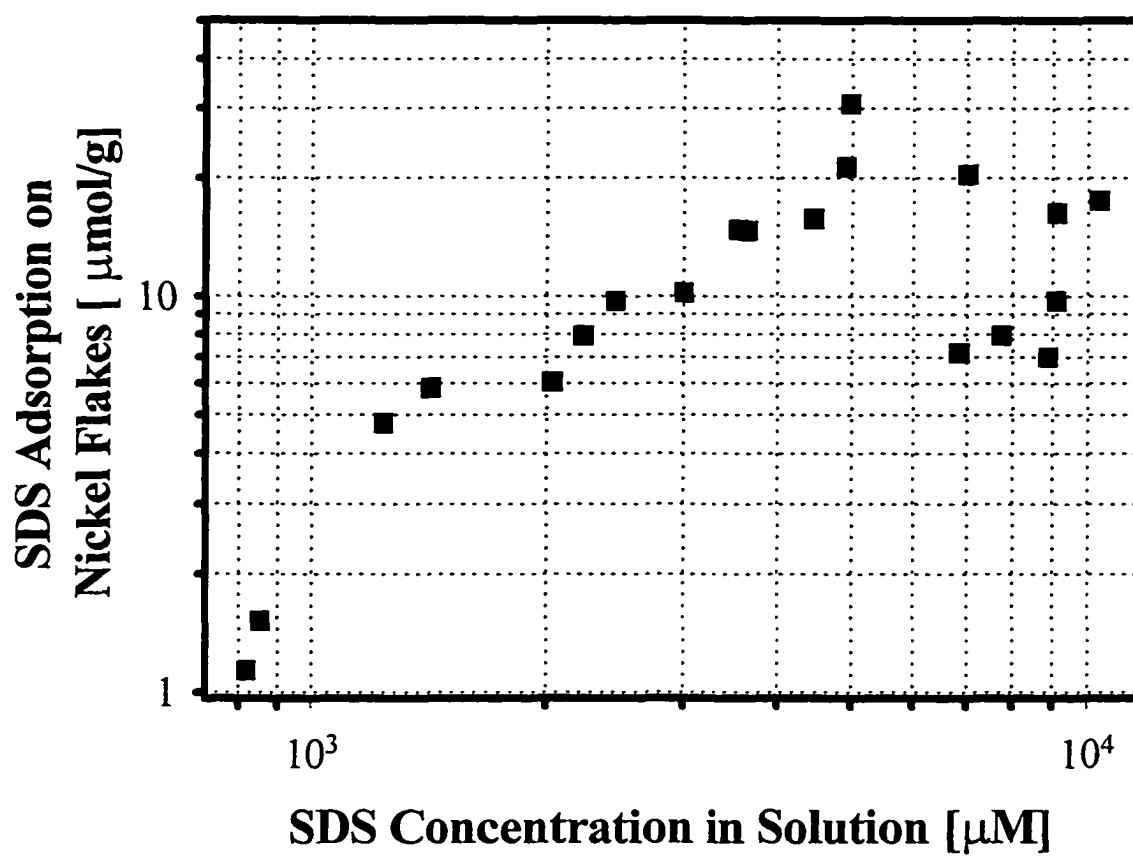
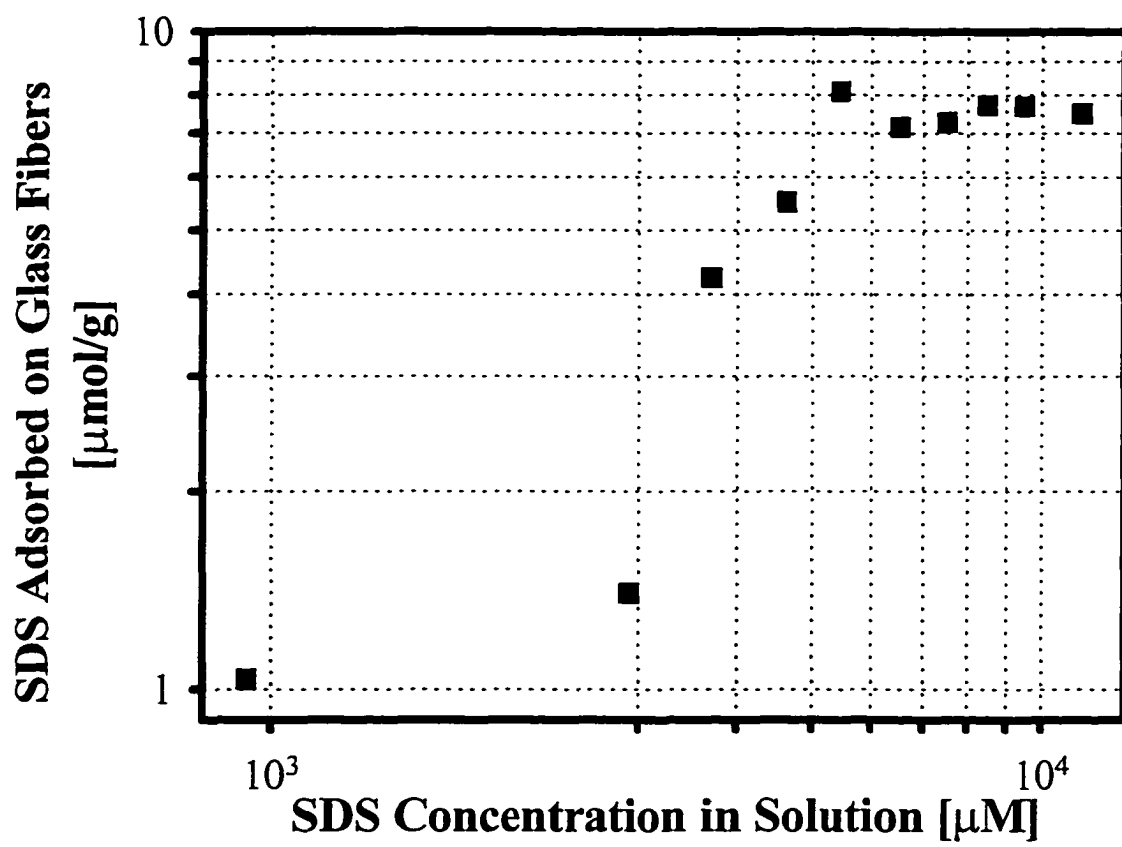


Figure 5-4 Adsorption Isotherm of Sodium Dodecyl Sulfate on Glass Fibers at a pH of 3.0



5.4.2 Particulate Characterization

The weight fraction of PPy on nickel was determined to be approximately 5.8 percent. The large-scale structures of nickel and PPy-coated nickel flakes, observed under an optical microscope, were similar. Both were flakes of approximately 40 μm with sharp edges and the grain boundary size of nickel and PPy-coated nickel were about the same (below 1 μm). No PPy were observed, indicating that the polymer was preferentially polymerized on the nickel surface.

STM, AFM, and CITS were used to investigate the structure of the PPy-coating on the surface of the nickel flakes. Figure 5-5 is a 1 μm STM image of PPy-coated nickel, which shows aggregates protruding up to 300 nm vertically from the substrate surface. The protrusions measured by section analysis ranged in thickness from 20 to 150 nm. To further understand the underlying PPy film, a 0.5 cm x 0.5 cm nickel foil (0.1 mm, Alfa Aesar) was coated with PPy under the same conditions as the flake, except without stirring. Figure 5-6 shows two AFM images: the image on the left is a bare nickel and the image on the right is PPy-coated. PPy-coating increased the horizontal total linear grain size by approximately 50 nm. Even though STM and AFM were able to show increased protrusions and grain size, distinguishing the film from the substrate in topographical images was difficult to achieve due to the randomness of the flake cuts.

Figure 5-7 is a 100 nm X 100 nm STM and CITS image of PPy-coated nickel. The upper left frame in the figure is a standard STM height image in which the tunneling current is kept constant, while the image on the right is a CITS image. The PPy,

Figure 5-5 STM Image of PPy-coated Nickel Flake (scan size, $1\mu\text{m} \times 1\mu\text{m}$; set point, 1 nA; bias voltage 2V)

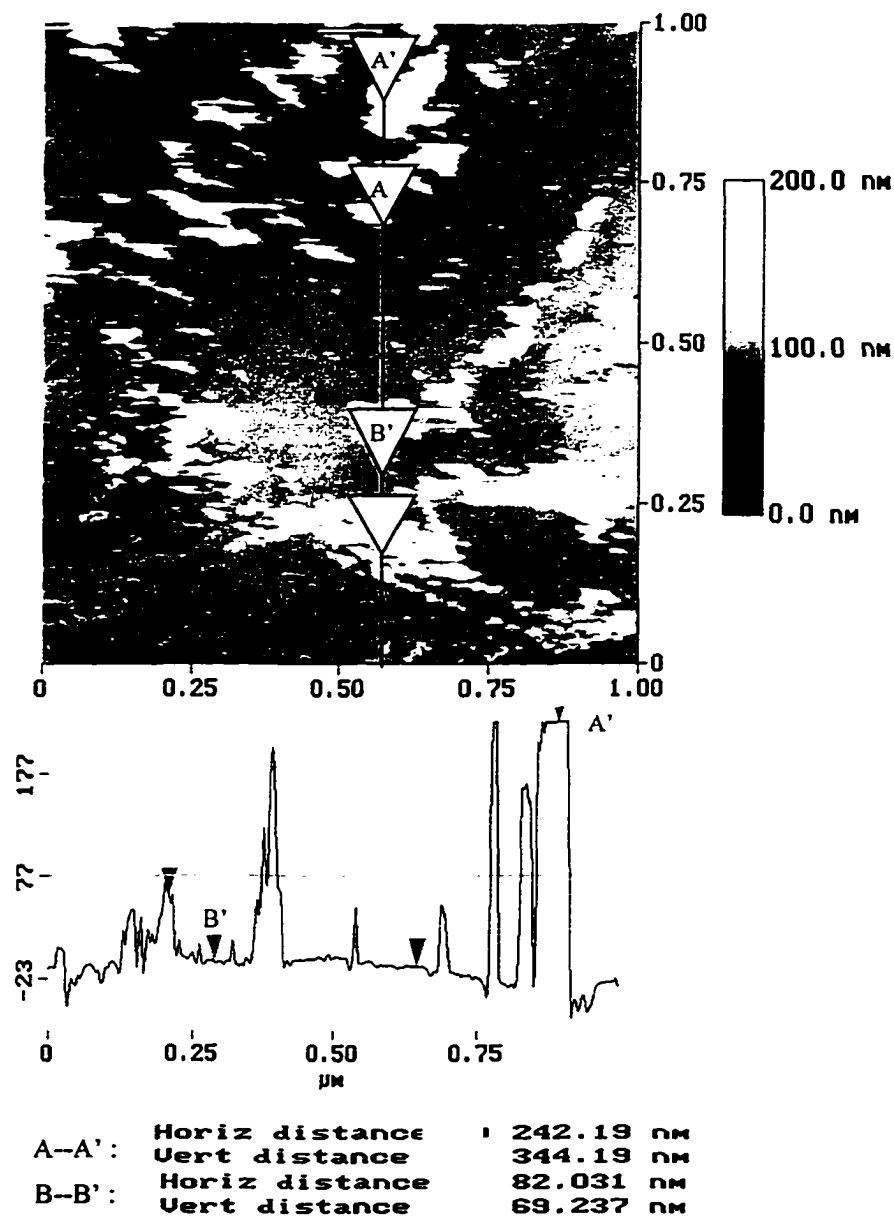


Figure 5-6 AFM Images of Bare (left) and PPy-coated (right) Nickel Foils (image size, 502 nm x 502 nm)

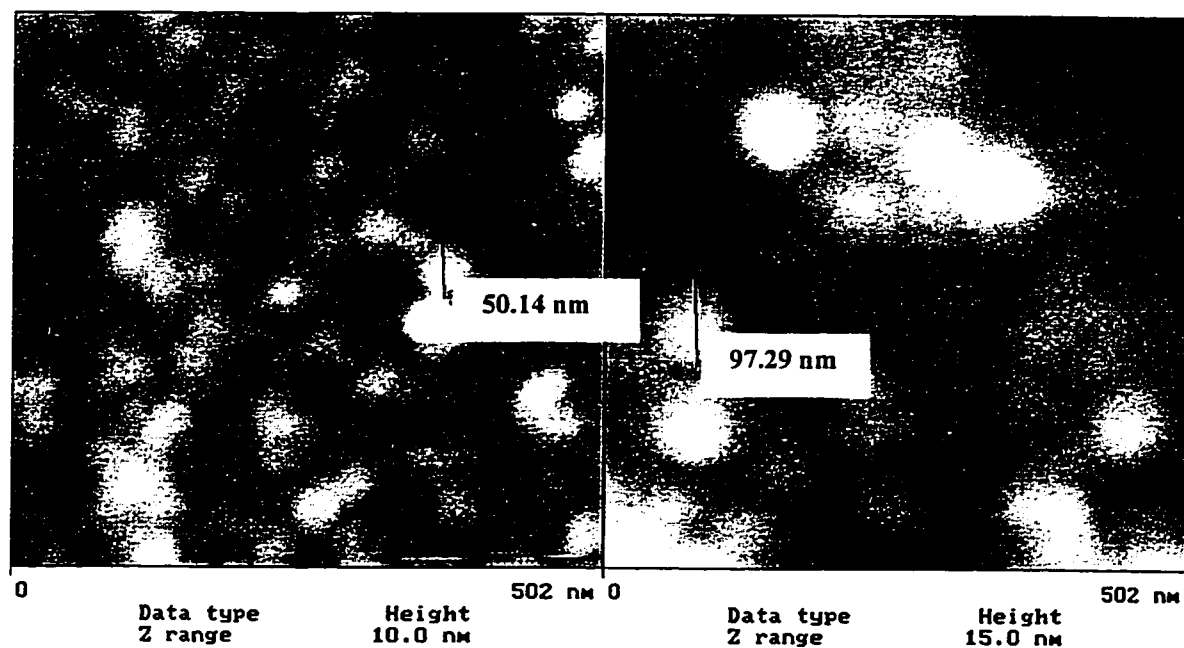
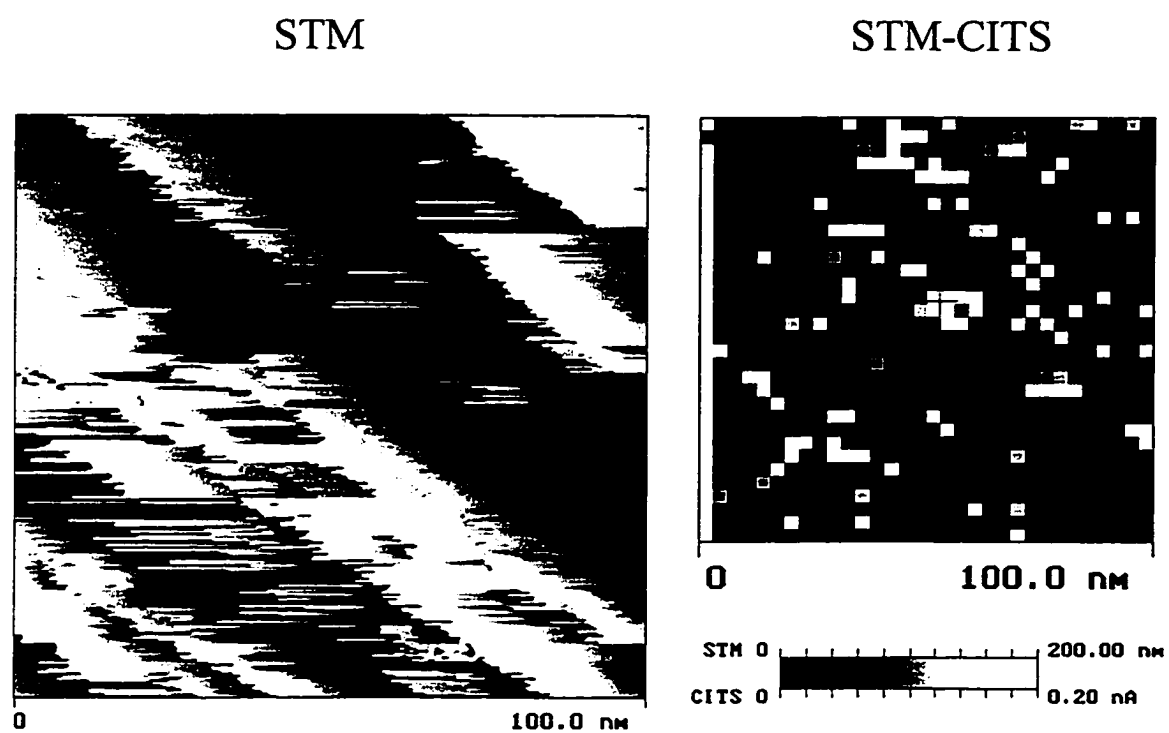


Figure 5-7 STM and CITS Images of PPy-coated Nickel (scan size, 100 nm x 100 nm; bias, 2 V; bias for CITS Image 1 V)



shown as bright regions, in the STM image is consistent with CITS and indicates the higher resistivity of the PPy ($2 \text{ m}\Omega\cdot\text{cm}$) than that of nickel ($6.97 \mu\Omega\cdot\text{cm}$).^{16,17} Both the presence of the protrusions and the higher presence indicate that PPy has coated the nickel surface in a patch-wise structure.

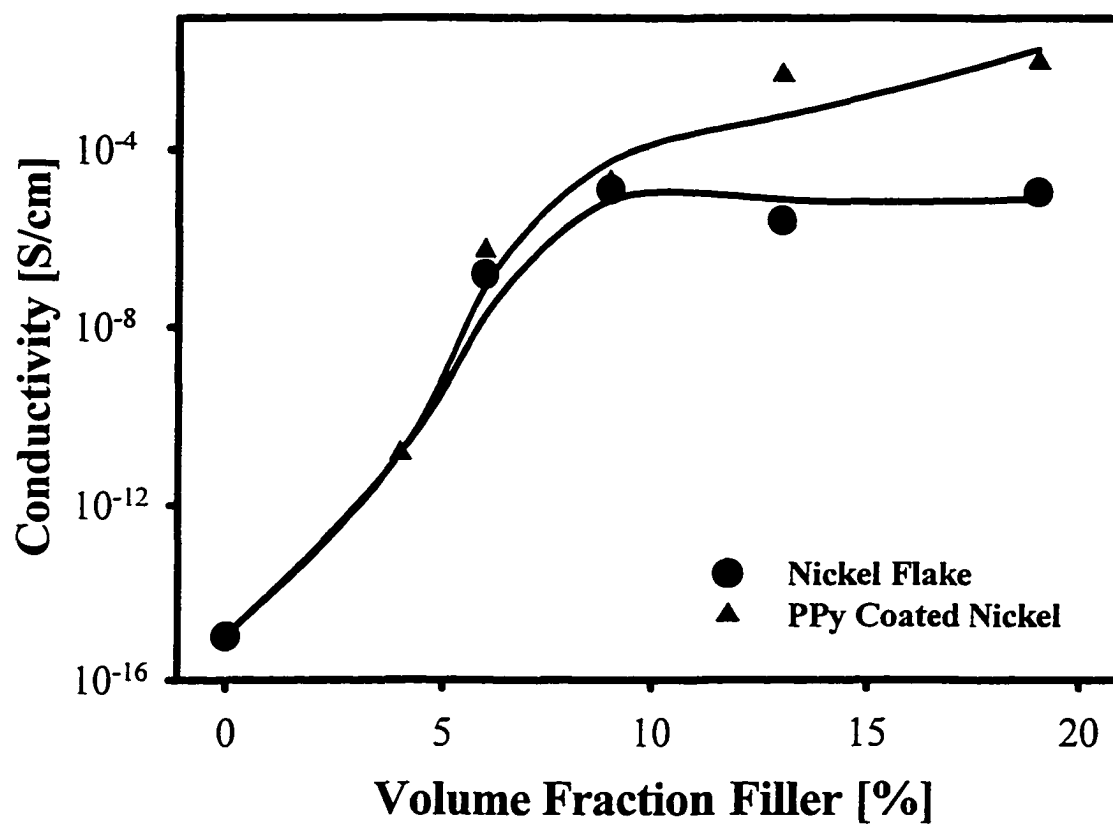
5.4.3 Nickel Composites

5.4.3.1 Conductivity

Figure 5-8 shows the percolation diagram for solution cast nickel and PPy-coated nickel flakes and indicates a percolation threshold for both composites of approximately 5 percent by volume. The conductivity curves have the same shape, but above the critical volume fraction the conductivity of the PPy-coated nickel-filled composites is 3 orders of magnitude greater (10^{-2} S/cm vs 10^{-5} S/cm) than the composite made from the uncoated nickel.

Increased conductivity in the composite films at a given filler loading is a result of either a decrease in the resistivity of the filler, or a decrease in the particle-particle contact and/or tunneling resistances. The resistivity of both the coated and uncoated nickel flakes was measured as approximately $1.1 \text{ ohm}\cdot\text{cm}$. In order to determine if the surface modification could have significantly increased the resistivity of the flakes, the resistivity, with and without the addition of the PPy-coating was calculated. For these simplified calculations, all resistances were assumed to be the same in each direction so

Figure 5-8 Percolation Diagram for Nickel and PPy-coated Nickel – Mixing by Solution Casting



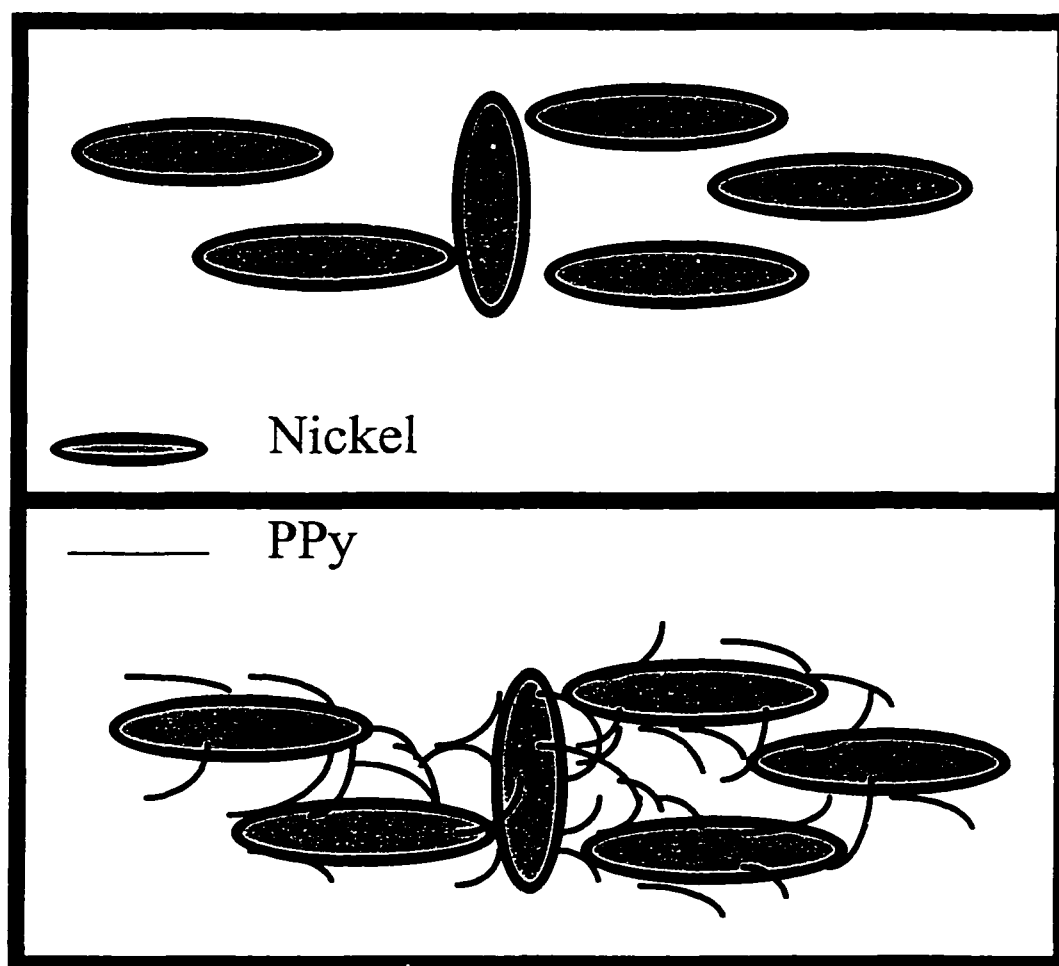
that all the currents canceled except for the current along the direction of the voltage drop. The randomly shaped flakes were modeled as uniform disks. The particle-particle contact resistance of the powder, R_{cr} , was calculated using Equation 5-3,¹⁸

$$R_{cr} = \frac{\rho_0}{d} \quad [5-3]$$

where ρ_0 ($6.97 \mu\Omega\cdot\text{cm}$) is the intrinsic resistivity of the flakes and d is the contact diameter. The average contact diameter was estimated to be approximately $0.79 \mu\text{m}$ by geometrical considerations. The approximate resistivity of the uncoated nickel flakes was calculated to be $2.8 \text{ ohm}\cdot\text{cm}$, which is close to the measured value of $1.1 \text{ ohm}\cdot\text{cm}$. Based on a uniform monolayer of the PPy-coating the particle and the film resistance in series with the packing resistance, the estimated resistivity of the modified nickel powder was calculated to be approximately $8.8 \text{ ohm}\cdot\text{cm}$. While these values are only approximate, they show that the PPy-coating should have significantly increased the resistivity of the powder. This inconsistency between the measured and calculated trend in resistivity is probably due to non-uniform coating of the particles as observed in the STM images. Non-uniform coatings of PPy particulates has been reported in the literature using a different polymerization technique than the one used here.¹ Both the calculated and the experimental resistivities testing indicate that the increase in the conductivity of the composite is not a result of a lower filler resistance.

Since the conductivity of the nickel and PPy-coated powders are not significantly different, we believe the three order of magnitude increase in conductivity is due to the combination of two phenomena. First, the admicellar coating reduces the particle-

Figure 5-9 Schematic Diagram of Molecular Wire Formation in PPy-coated Nickel-LDPE Composites



particle contact resistance. Figure 5-9 is a schematic diagram of the possible interactions of the PPy-coating with the polymer matrix. PPy entanglements are probably formed between the particles and act as bridges. These entanglements increase the contact area between the nickel particles by, in effect, becoming “molecular wires” connecting the filler particles causing an increased contact area due to contacts of PPy particles outside the polymer matrix. Further, the PE matrix shrinks during solvent evaporation and crystallization, internal stresses place forces on the filler particles. The PPy-coating softening the surface enhances this effect. The softer surface on the PPy-coated nickel particles will also increase the contact area versus the non-coated material. Second, entanglements between the PPy and the LDPE will “short circuit” the tunneling resistance because the film thickness between the conductive pathways decreases due to formation of conductive polymer paths between nickel particles.

In order to determine how processing effects the conductivity enhancement of the PPy-coated nickel filler, composites of PPy-coated nickel and nickel flake were prepared by melt mixing in an extruder. The 3 order of magnitude incremental increase in composite conductivity due to the PPy-coating was decreased to 2 orders of magnitude when the composites were processed by extrusion as shown in Figure 5-10. The high shear in the extruder may dislodge some of the PPy film or the particles may be broken apart by mechanical forces exposing more non-coated surface area.

Figure 5-11 shows the conductivity versus draw ratio for both the nickel and PPy-coated nickel at a volume fraction in the critical region (7 percent) in the stretching

direction. As with the conductivity profile, in the critical region the conductivity of the nickel and PPy-coated nickel are approximately 5×10^{-6} S/cm. The composites followed the same trend in conductivity versus draw ratio by initially increasing, then decreasing exponentially as the filler particles are pulled apart breaking the conductive pathways.

Above the critical region (Figure 5-12), the nickel filled composite shows the same trend as in the critical region, but the PPy-coated nickel composite only shows a slight decrease in conductivity at draw ratios as high as 2.5. This observation, as depicted schematically in Figure 5-13, is consistent with the nickel flakes being connected by the PPy “molecular wires.” Intrinsically conducting polymers, such as polypyrrole (PPy), contain conjugated backbones with sp^2 hybridized orbitals that lead to overlap of the unhybridized p orbitals along the chain.¹⁹ Orientation of the polymer chains leads to more linear conductive pathways that increase the conductivity of the material in the stretching direction. The PPy entanglements that tie the particles together and become more conductive with draw ratio may counter the loss in conduction due to the filler particles being pulled apart.

5.4.3.2 Crystallinity

As shown in Figure 5-14, the crystallinity of LDPE increased with increasing volume fraction. While the data indicates that the PPy-coating does slightly increase the crystallinity at low volume fractions, there is no statistical difference in crystallinity

Figure 5-10 Percolation Diagram for Nickel and PPy-coated Nickel – Mixing by Extrusion

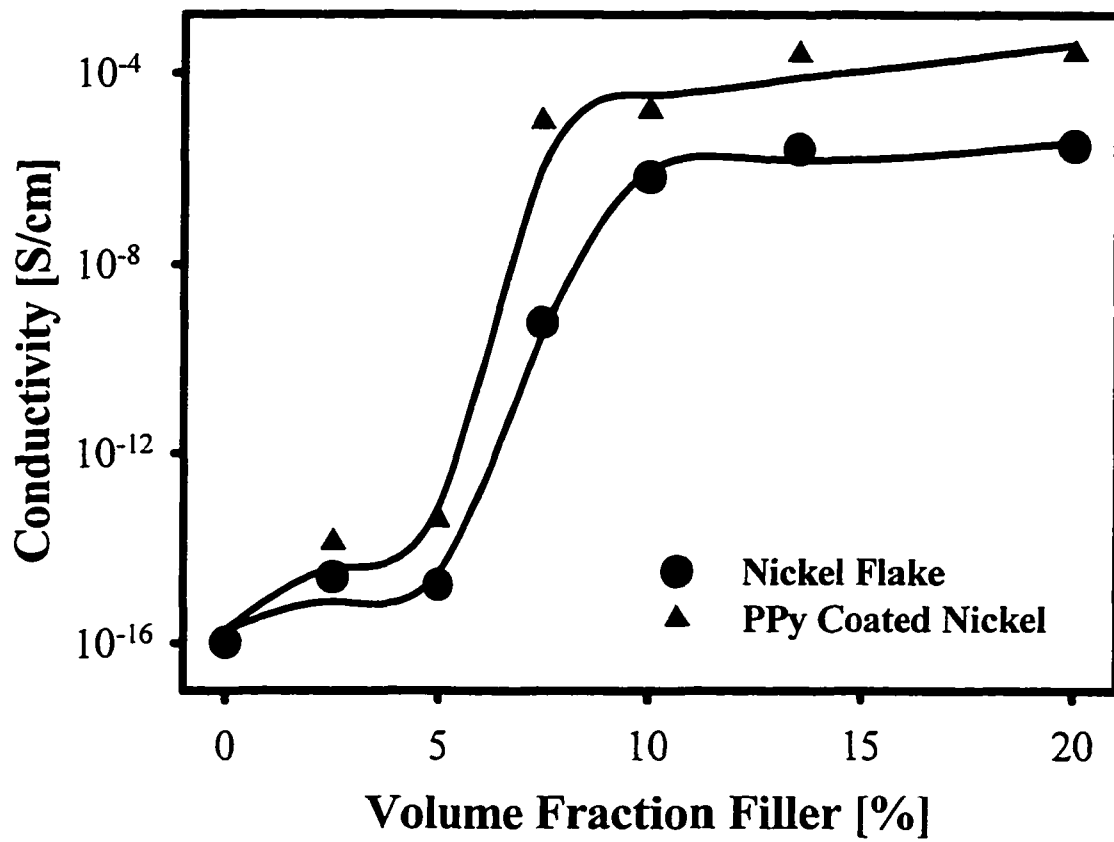


Figure 5-11 Conductivity versus Draw Ratio for Nickel and PPy-coated Nickel - LDPE Composites in the Critical Region (7 % by volume filler)

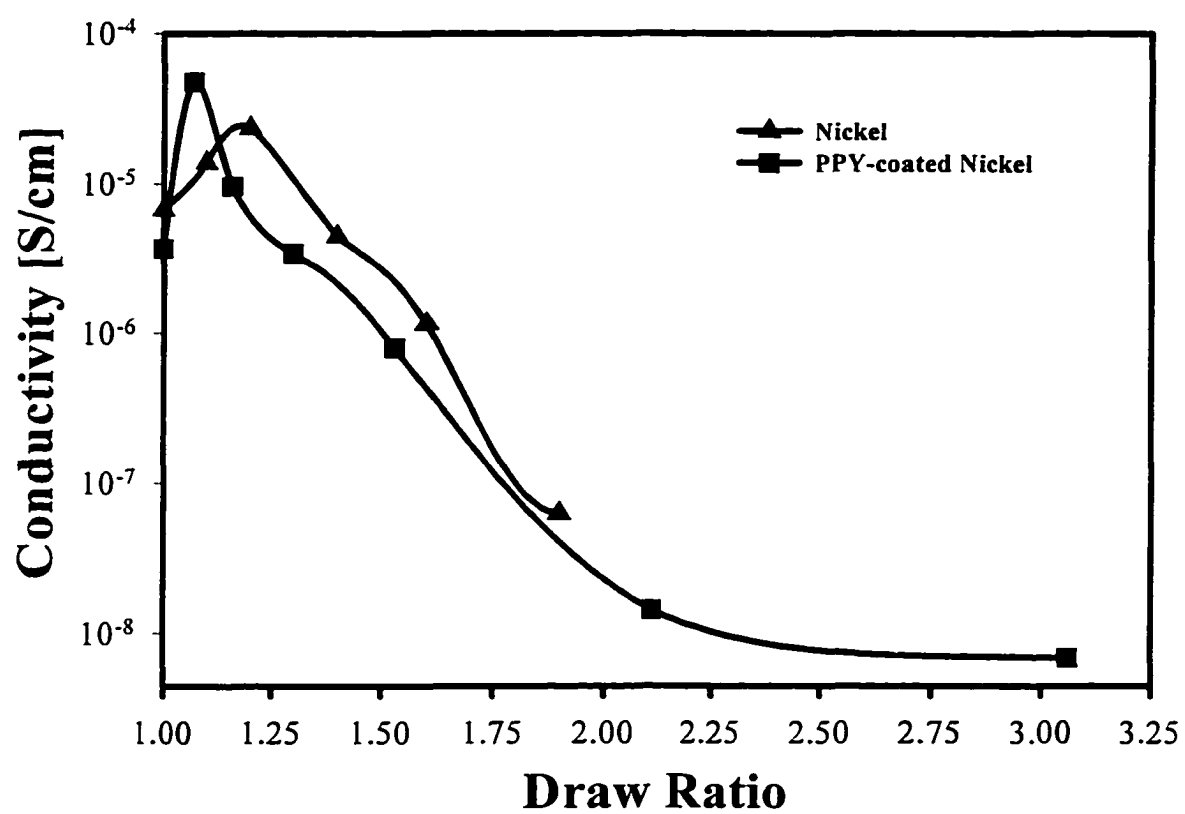


Figure 5-12 Conductivity versus Draw Ratio for Nickel - LDPE (\blacktriangle) and PPy-coated Nickel - LDPE (\blacksquare) Composites in Plateau Region (13 % by volume filler)

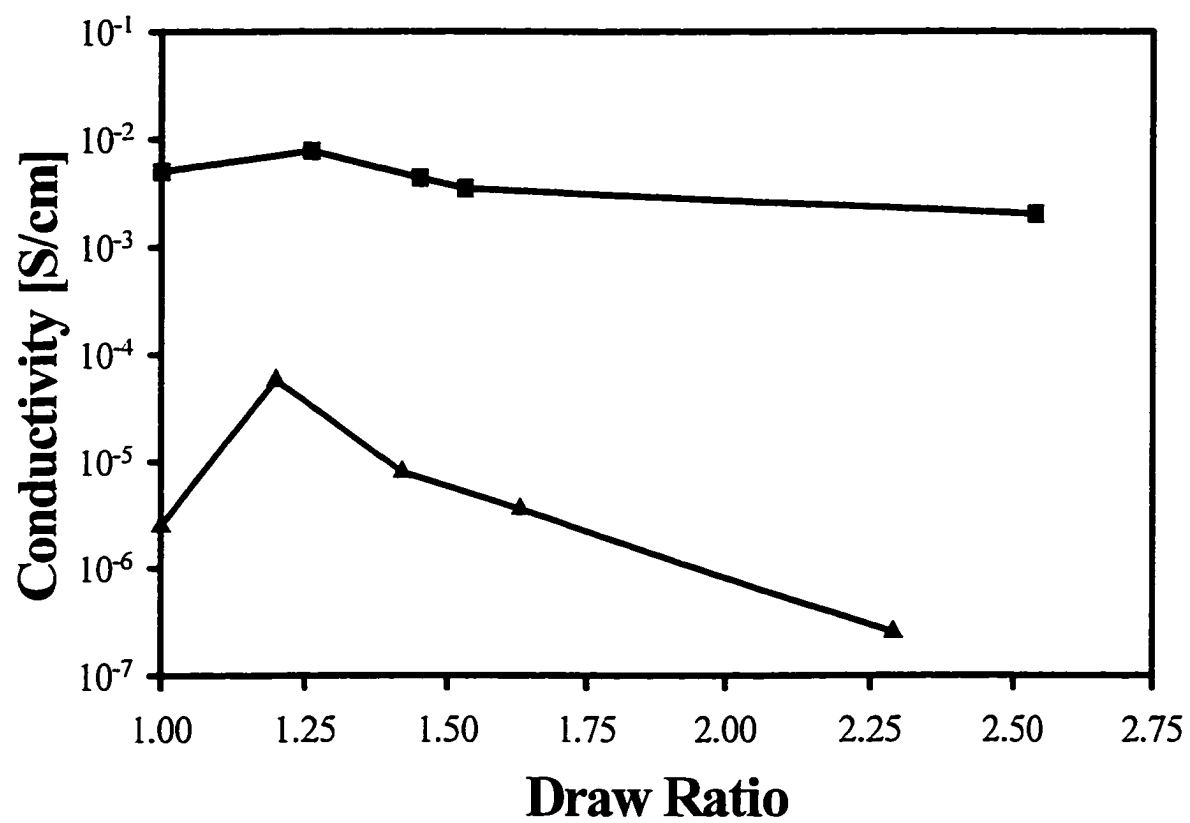
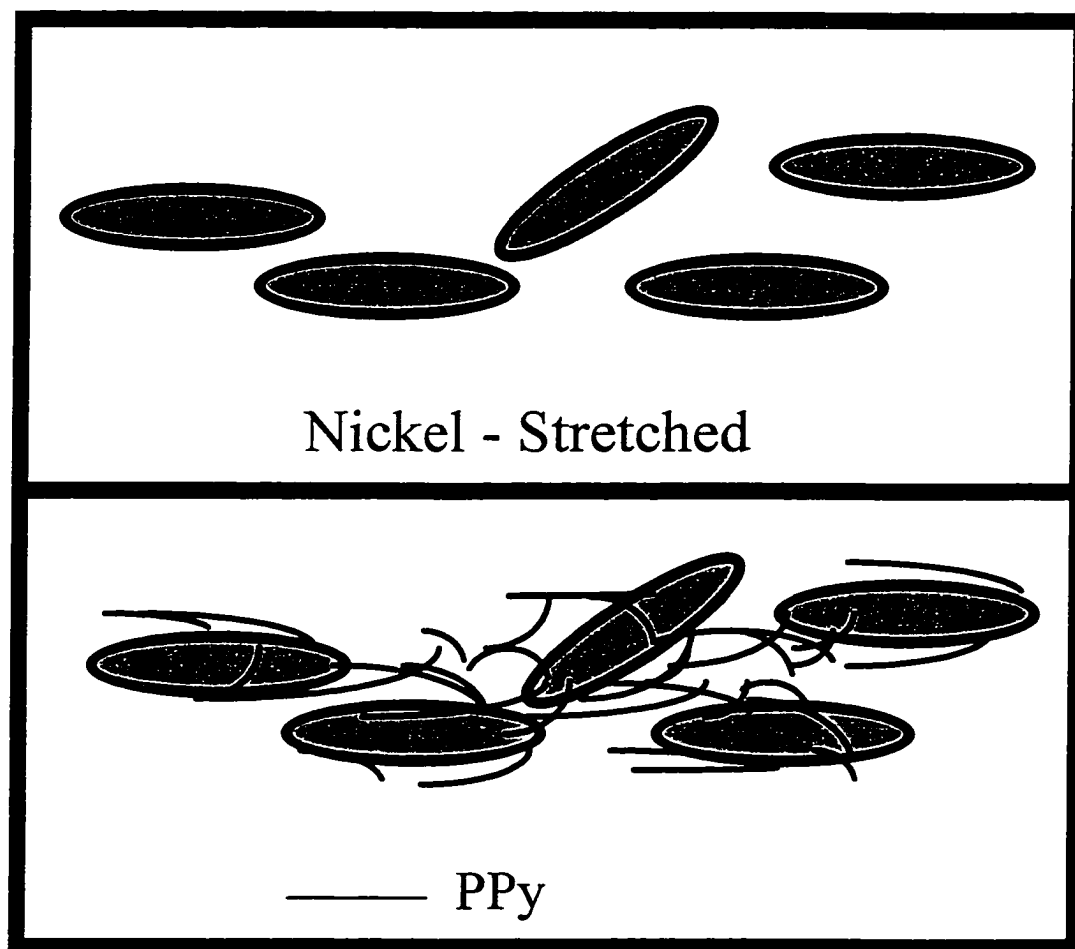


Figure 5-13 Schematic Diagram of PPy Entanglements During Stretching



at high filler loadings. The high branching of the LDPE matrix prevents the polymer from forming large crystalline regions and the crystallinity is consistent with other highly branched polyethylene.²⁰

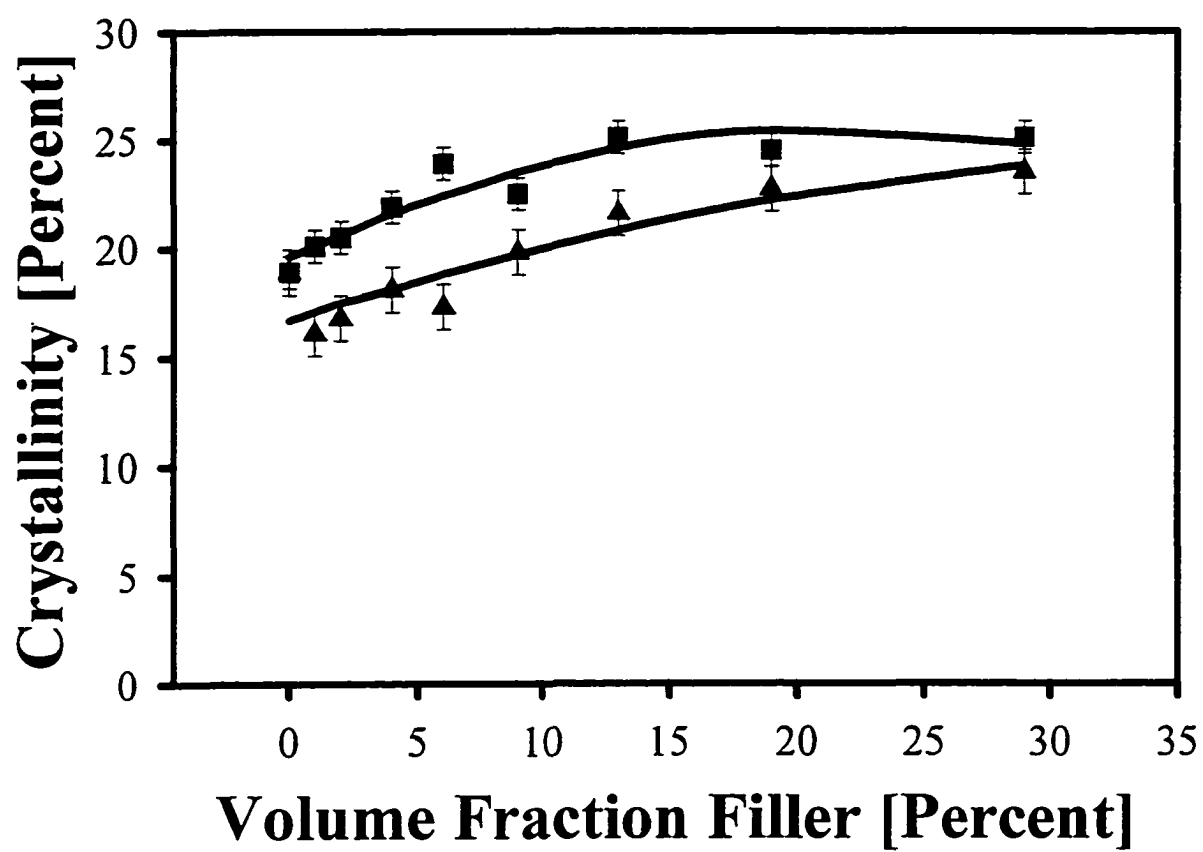
5.4.3.3 Mechanical Properties

The tensile modulus of the composite materials increased with increasing volume fraction, as shown in Figure 5-15. However, the elongation at break, shown in Figure 5-16, and the ultimate strength, shown in Figure 5-17, decreased exponentially by the initial addition of the nickel due to the creation of fracture points at the nickel - LDPE interface. The addition of the PPy-coating to the nickel did not significantly change the mechanical properties as PPy is not miscible with LDPE. PPy is much stiffer than LDPE and is not soluble in xylene and may act as a mechanical reinforcing agent similar to nickel under these conditions. To test this hypothesis, the mechanical properties of a 29 percent by volume LDPE - PPy blend were measured. The blend showed similar values in tensile modulus, elongation at break, and ultimate strength as that of the metal flake filled composites. This indicates that PPy is acting as a filler and that interfacial adhesion between the filler and the polymer-matrix was not significantly changed by the addition of the PPy-coating.

5.4.4 Alumina and Glass Fiber Composites

Figure 5-18 shows the percolation diagram for alumina, indicates that the

Figure 5-14 Crystallinity versus Concentration of Nickel-LDPE (▲) and PPy-coated Nickel-LDPE (■) Composites



percolation threshold is between 10 and 15 percent by volume, and was not affected by the addition of the PPy-coating. The significantly higher percolation threshold of alumina compared to the nickel flakes is a result of a much lower aspect ratio of the former. The plateau conductivity for the PPy-coated alumina composites was on the order of 10^{-6} S/cm, a 4 order of magnitude increase over the non-coated composites. As discussed above, the powder conductivity of the nickel flakes was not affected by the addition of the PPy-coating indicating that the primary electron transfer phase was the nickel particles.

The coated alumina had a powder conductivity of approximately 10^{-6} S/cm, compared to 10^{-9} S/cm for the non-coated alumina powder. This result, coupled with the shift in the percolation threshold, indicates that a significant fraction of electron transfer occurs in the PPy phase independent of the alumina.

The percolation diagram for the glass fiber composites is not presented here. Above the percolation threshold, composites made from the coated material had a 1 order of magnitude higher conductivity than the composite made from the non-coated glass fiber (10^{-13} vs. 10^{-14}). We believe this result indicates that even though the glass fiber is above the percolation threshold, no continuous network of PPy molecules exists in this material.

Figure 5-15 Tensile Modulus versus Concentration of Nickel-LDPE (▲) and PPy-coated Nickel-LDPE (■) Composites

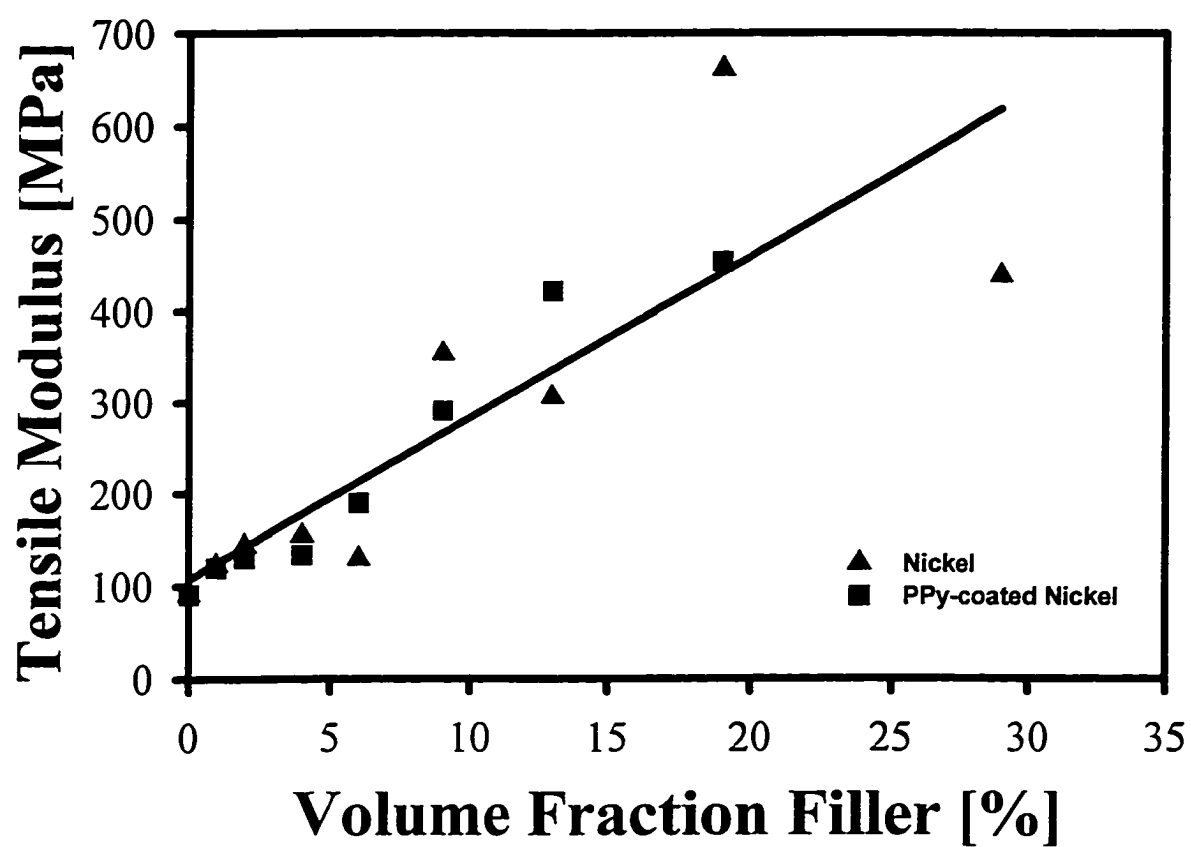


Figure 5-16 Elongation at Break versus Concentration of Nickel-LDPE (▲) and PPy-coated Nickel-LDPE (■) Composites

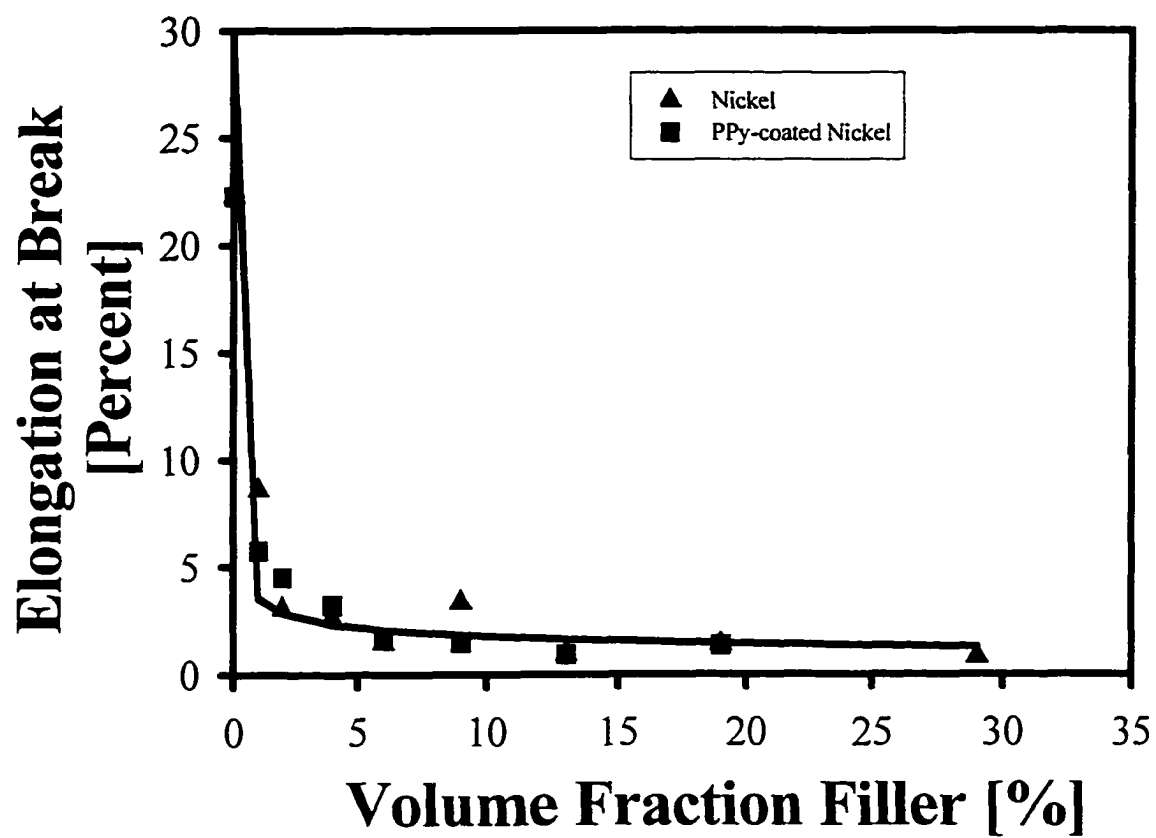


Figure 5-17 Ultimate Strength versus Concentration of Nickel-LDPE (▲) and PPy-coated Nickel-LDPE (■) Composites

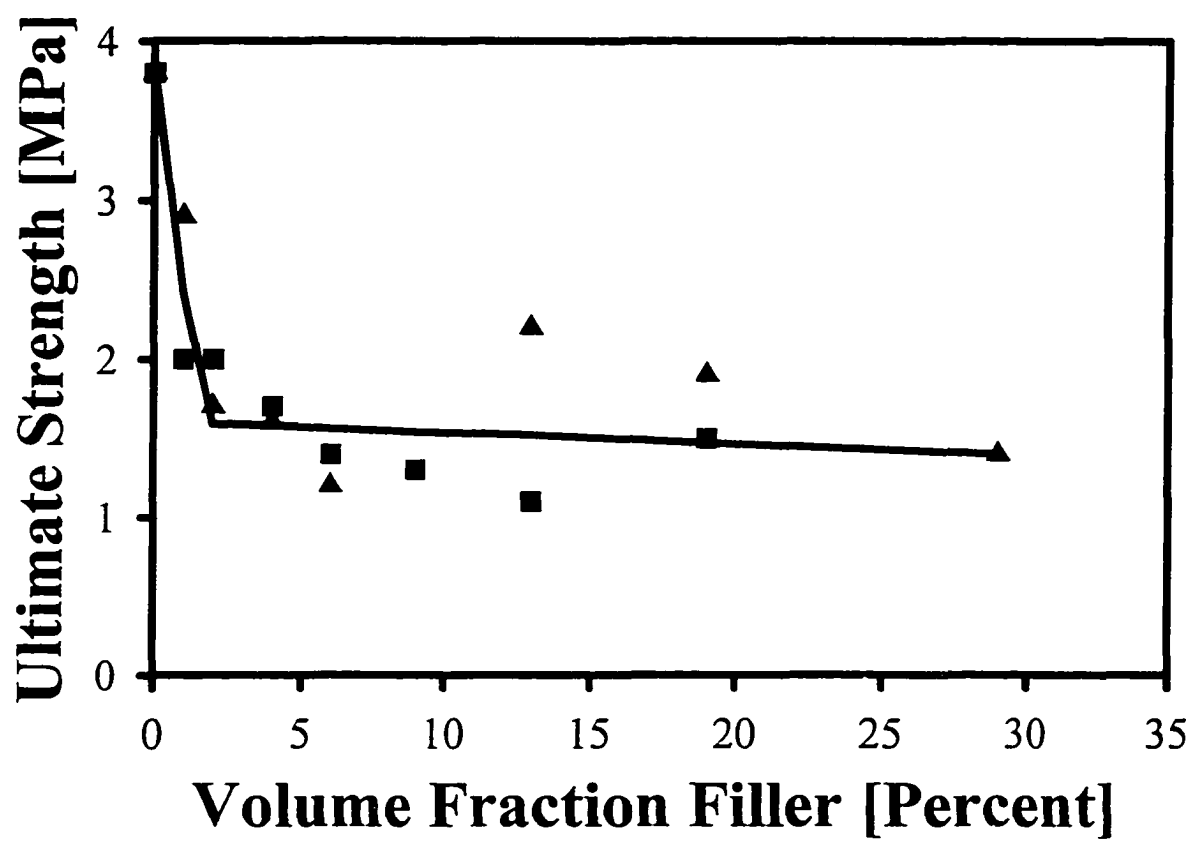
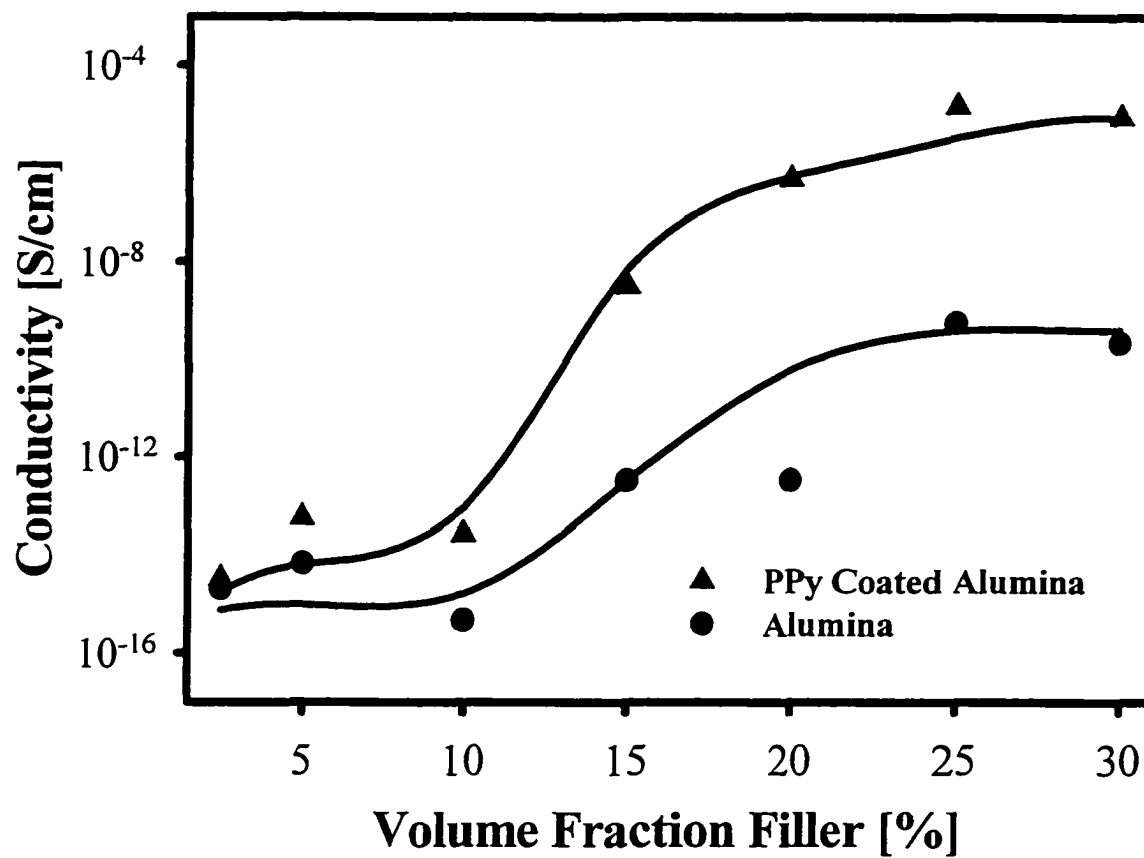


Figure 5-18 Percolation Diagram for Powder Mixed Alumina



5.5 CONCLUSION

PPy-coating by admicellar polymerization increases the conductivity of nickel-filled LDPE above the percolation threshold by approximately 3 orders of magnitude. This increase may be due to the formation of “molecular wires” created by PPy entanglements at the particle-particle interface. These entanglements probably decrease the particle-particle contact resistance by increasing the contact area of the filler particles and may also reduce the tunneling resistance by decreasing the film thickness through which a conducting electron must hop.

The large-scale structures of PPy-coated nickel and nickel flakes are similar. The flake is approximately 40 μm and no PPy particles mixed with PPy-coated nickel flakes were observed. The film-like and strand-like structures observed in STM images of PPy-coated nickel confirms the existence of PPy on the nickel flakes. The small-scale STM study showed the film-like structure had lower conductivity than that of the nickel substrate.

The typical loss in conductivity with draw ratio was not observed in the PPy-coated nickel composites at filler concentrations above the critical region. This retention in conductivity may be explained by the stretching of the “molecular wires” which allows the conductive pathways to stay intact. The mechanical properties of the composite were not affected by the addition of PPy-coating. This composite system has enhanced electrical properties, which may expand the processing techniques available for metal filled polymer matrix composites.

The mechanical and thermal properties of the composite were not affected by the addition of the PPy-coating. The crystallinity of the LDPE increases with increasing filler concentration. At higher volume fractions the coating did not statistically affect the crystallinity. The tensile modulus increased with filler concentration, but the ultimate stress and elongation at break decreased with the increasing filler concentration due to poor polymer-filler adhesion. The mechanical properties of the composite were not affected by the addition of the PPy-coating to the nickel particles as a result of the immiscibility of PPy in LDPE.

The admicellar polymerization technology has been shown as a viable method for producing ultrathin, conductive films on particulates to be used as fillers for conductive composites. The surface modifications increase the conductivity by at an order of magnitude over the unmodified films conductive, resistive, and an insulator substrates. The limitation of this technology is the ability to get uniform coverage necessary to obtain greater increases in conductivity on non-conductive substrates.

5.6 NOTATION

V	Volume Fraction of Discontinuous Phase
ρ_F	Filler Density
ρ_P	Matrix Polymer Density
ρ_{PPy}	Density of Polypyrrole
w_F	Filler Weight Fraction
w_{PPy}	Weight Fraction of Polypyrrole
R_{cr}	Particle-Particle Contact Resistance
ρ_0	Intrinsic Resistivity of Filler
d	Contact Diameter

5.7 REFERENCES

- 1 S. P. Armes, S. Gottesfeild, J. G. Beery, F. Garzon, and S. F. Agnew, *Polymer*, **32**, 2325, (1991).
- 2 R. Partch, S. G. Gangolli, E. Matijevic, W. Cai, and S. ARAJS, *J. Coll. I. Sci.*, **144**, 27, (1991).
- 3 G. P. Funkhouser, M. P. Arevalo, D. T. Glatzhofer, and E. A. O'Rear, *Langmuir*, **11**, 1443, (1995).
- 4 M. A. Fox, and K. L. Worthen, *Chem Mater.*, **3**, 253, (1991).
- 5 M. Gill, S. P. Armes, D. Fairhurst, S. N. Emmett, G. Idzorek, and T. Pigot, *Langmuir*, **8**, 2178, (1992).
- 6 C. L. Huang, R. E. Partch, and E. Matijevic, *J. Col. I. Sci.*, **170**, 275, (1995).
- 7 E. P. Plueddemann, Silane Coupling Agents, 2nd Edition, Plenum Press, New York, 206 and 208, 1991.
- 8 J. H. O'Haver, J. H. Harwell, E. A. O'Rear, L. J. Snodgrass, and W. H. Waddell, *Langmuir*, **10**, 2588, (1994).
- 9 T. A. Ezquerro, R. K. Bayer, and F. J. Balta Calleja, *J. Mater. Sci.*, **23**, 4121, (1988).
- 10 W. B. Genetti, and B. P. Grady, *ACS Polymer Preprints*, **37**, 819, (1996).
- 11 J. Wu, J. H. Harwell, E. A. O'Rear, and S. C. Christian, *AIChE J.*, **34**, 1511, (1988).
- 12 W.B. Genetti, B.P. Grady, and E.A. O'Rear, in "Electronic Packaging Materials Science IX," S.K. Groothuis, P.S. Ho, K. Ishida, and T. Wu, editors, MRS, Pittsburgh, PA, Vol. 445, 153, (1997).

- 13 J. Wu, J. H. Harwell, and E. A. O'Rear, *J. Phys. Chem.*, **91**, 623, (1987).
- 14 W. B. Genetti, W. L. Yuan, B. P. Grady, E. A. O'Rear, C. L. Lai, and D. T. Glatzhofer, *J Mater. Sci.*, **33**, 3085, (1998).
- 15 W. B. Genetti, P.M. Hunt, M. Shah, A.M. Lowe, E.A. O'Rear and B. P. Grady, submitted to The Proceedings of the 7th International Symposium on Chemically Modified Surfaces Fundamental and Applied Aspects of Chemically Modified Surfaces.
- 16 J. A. Dean, Lange's Handbook of Chemistry, 14th Edition, McGraw-Hill, Inc., New York, NY, 47, 1992.
- 17 J. R. Fried, Polymer Science and Technology, Prentice Hall PTR, Englewood Cliffs, New Jersey, 463, 1995.
- 18 R. G. Ruschau, S. Yoshikawa, R. E. Newnham, *J. Appl. Phys.*, **72**, 953, (1992).
- 19 A. L. Blythe, Electrical Properties of Polymers, Cambridge University Press, Massachusetts, 104, 1979.
- 20 S. L. Aggarwal, in Polymer Handbook, 2nd Edition, edited by J. Brandrup and E. M. Immergut, John Wiley & Sons, New York, V-13, 1975.

CHAPTER 6

CONCLUSIONS AND FUTURE WORK

6.1 INTRODUCTION

Past research on conductive polymer-matrix composites has focused on the relationships between concentration, geometry, and dispersion of the discontinuous phase and the physical properties of the resulting material. However, the volume fraction – geometry approach does not take into account the influence of polymer morphology and polymer-filler interactions on the composite properties. The work presented in this dissertation has focused on the following questions:

- How does the presence of the filler affect the polymer?
- How does particulate surface modification change the properties of the composite material?

The preferential orientation and crystallization kinetics studies presented in Chapters 3 and 4, respectively, describe changes in the matrix polymer induced by the filler.

Changes in both the electrical conductivity and processibility of the composite due to modifications of the particulate surface are presented in Chapter 5.

6.2 HOW DOES THE PRESENCE OF THE FILLER AFFECT THE POLYMER?

These studies have shown that the filler changes the structure and morphology of the polymer in the following ways:

- Addition of whisker like fibers by reticulate doping formed a two-dimensional network in the casting plane. This network of TTF-TCNQ changed morphology by shifting the preferential orientation of the LDPE crystallites from perpendicular to parallel to the casting surface.
- An incremental increase in preferential orientation of the uniaxially stretched TTF-TCNQ – LDPE was observed with increasing draw ratio, but this incremental increase was reduced at higher filler loadings.
- Addition of metal flakes alters the crystallization kinetics due to the changes in local heat transfer.

6.2.1 Polymer Crystallite Orientation

WAXS was used to study PE crystallite orientation in reticulate doped polymer composites of TTF-TCNQ supported by PE. The solution cast films of PE showed orientation of the crystallite lamella perpendicular to the casting surface, but the addition of TTF-TCNQ microcrystallizing inside the matrix forced PE crystals to preferentially form parallel to the casting surface. Uniaxial stretching parallel to the casting surface increased the orientation of the crystallites along the stretching direction. The incremental increase in orientation with stretching was decreased with higher filler loading.

WAXS studies were only performed on systems of TTF-TCNQ, which form branched whiskers with high aspect ratios. The change in preferential orientation has been attributed to the formation of a two-dimensional network of TTF-TCNQ parallel to the casting plane. Additional experimentation with fillers produced in different shapes, such as spheres, flakes, and fibers, could induce different preferential orientation profiles for each geometry.

Many novel switching devices have been designed based the temperature dependence of composite conductivity. Studying the temperature dependence of the CTC – polymer composites may lead to devices for applications in as temperature induced switching devices. In addition, only the DC conductivity was measured and characterization of the AC conductivity may also improve our understanding of reticulate doped polymer composites.

All samples in the WAXS study were solution cast. Testing different processing techniques, such as extrusion and calendaring, which may also produce a two dimensional network of anisotropic particles, would provide additional insight into the cause of the shift in preferential orientation. This work should also be expanded to include non-conductive fillers, such as reinforcing agents.

6.2.2 Crystallization

Isothermal crystallization experiments have been carried out for nickel-LDPE composites from 95° to 104° C. The network of nickel particles described by

percolation statistics, used to characterize electrical conductivity, can also be applied to changes in crystallization kinetics. There is an upward shift in the crystallization rate, which corresponds to the end of the critical region in electrical conduction. I believe the continuous network of nickel particles dissipates the heat of crystallization, thus allowing crystallization to occur more rapidly.

Work has already begun to expand the crystallization kinetics study from isothermal crystallization to in-situ film formation in extruded nickel-LDPE composites. Nickel supported by LDPE was examined with varying filler loadings and draw ratios. A plunger type extruder with a film die head and a stretching apparatus, shown in Figure 6-1, was built at the University of Oklahoma. As shown in Figure 6-2, the device mounted directly to the χ -circle of a wide angle x-ray scattering camera. The effect of nickel on the crystallization of the LDPE was studied in-situ by specifying a particular bragg reflection peak and setting the detector at its scattering angle (θ) in order to measure the intensity versus crystallization time. In order to fully characterize the relationship between processing properties and crystallization time, samples with both increasing volume fraction and draw ratio were examined. These experiments were done in conjunction with conductivity measurements and viscometry in order to understand the effects of nickel on the electrical properties of the composites and the crystallization kinetics of the polymer.

Figure 6-1 Plunger Extruder with Film Die and Stretching Apparatus

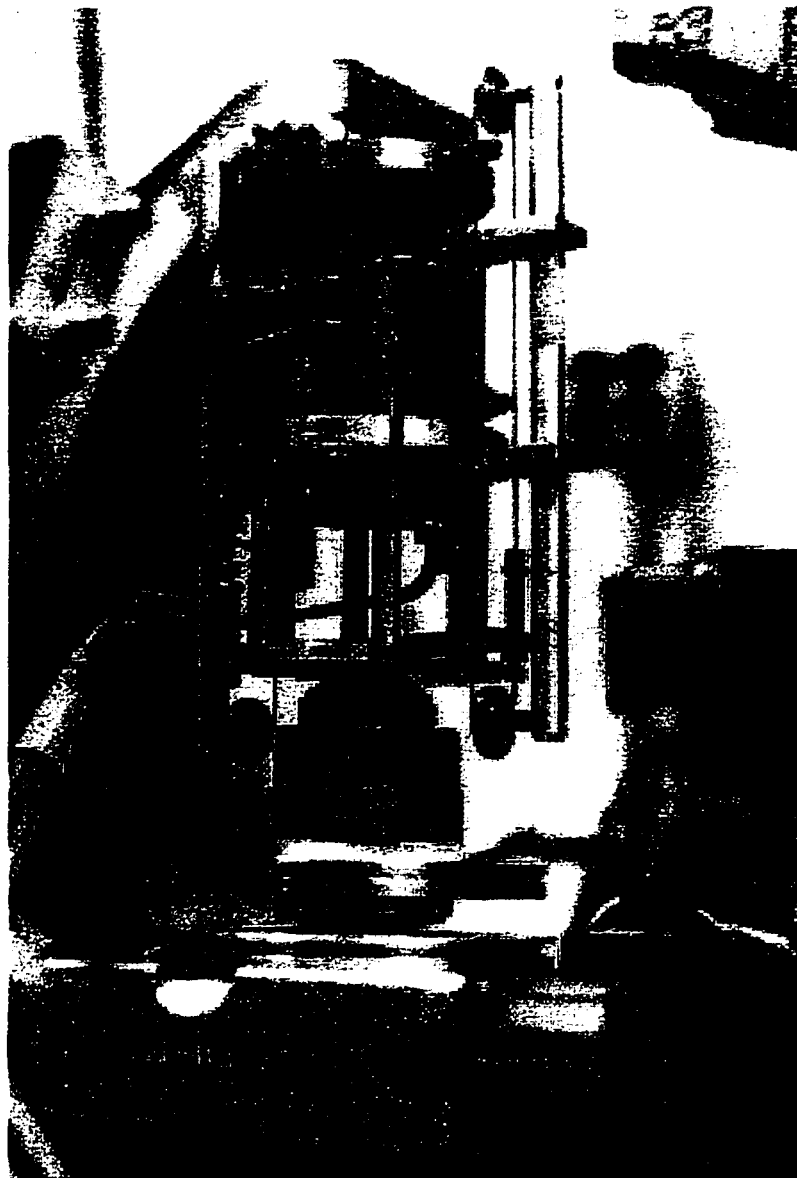
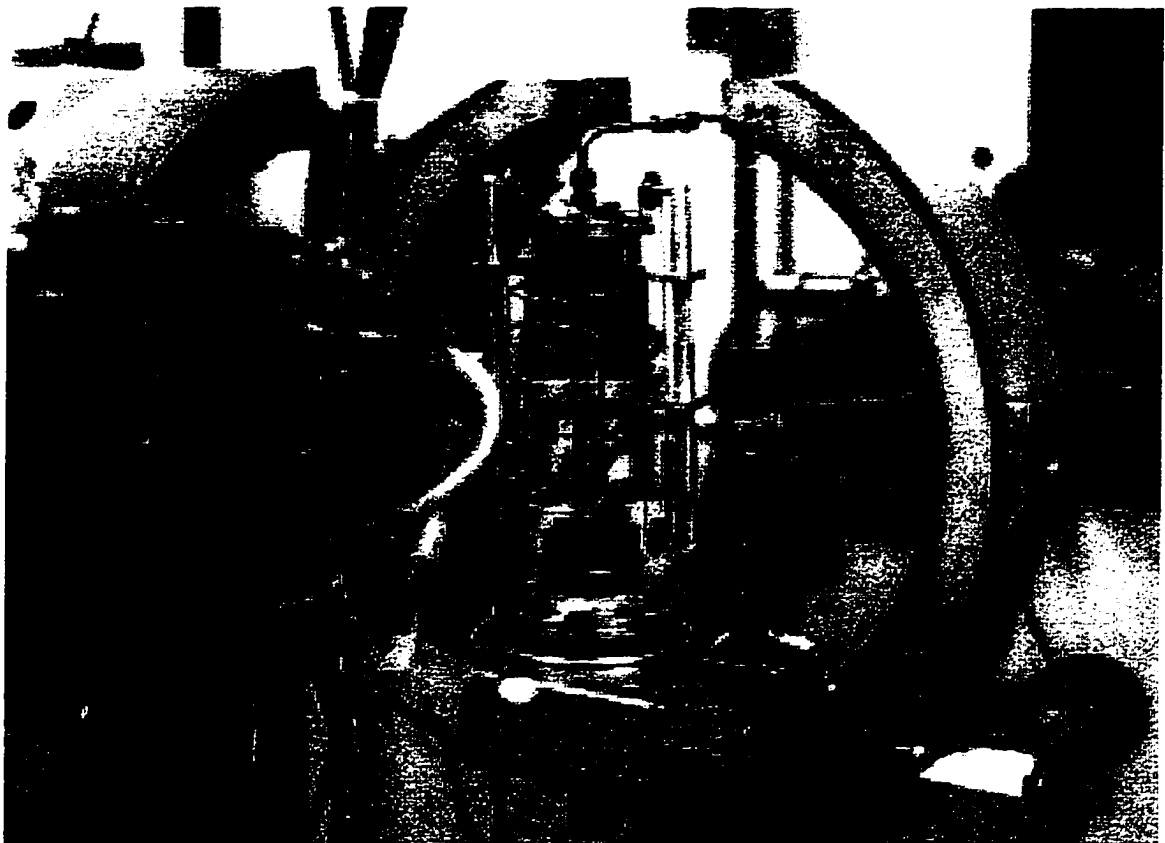


Figure 6-2 Extruder and Stretcher shown in χ -Circle



6.3 HOW DOES PARTICULATE SURFACE MODIFICATION CHANGE THE PROPERTIES OF THE COMPOSITE MATERIAL?

The addition of an ultrathin PPy film to the surface of particulates for applications in conductive composites induced the following changes in composite properties and processibility:

- Polypyrrole (PPy) coating of the particulates enhanced composite conductivity due to the reduction in the particle-particle contact and tunneling resistances.
- The PPy coating increased conductivity for conductive and resistive fillers: however, conductivity for insulating fillers did not increase substantially.
- The loss of conductivity due to processing was reduced by the addition of the PPy film.
- Mechanical properties were not affected by the addition of the PPy coating.

The admicellar polymerization technology has been shown as a viable method for producing ultrathin, conductive films on particulates to be used as fillers for conductive composites. The typical loss in conductivity with draw ratio was not as significant in the PPy-coated nickel composites at filler concentrations above the critical region. Addition of a polypyrrole film to nickel particulates increased the conductivity of nickel-filled composite 2-3 orders of magnitude, depending on the processing method used to mix the polymer and the filler. In aluminum oxide, the conductivity increased 4 orders of magnitude. The larger increase in the latter is probably due to the fact that polypyrrole acts as an alternate current path in portions of the composite, since the conductivity of polypyrrole is actually larger than the conductivity of alumina. In glass fiber composites, the increase in conductivity with the addition of a coating to the filler

was minimal, which confirms that polypyrrole does not form a continuous network throughout the sample.

If the polypyrrole film totally covered the glass surface, then the polypyrrole network would have been continuous since the glass concentration was well above the percolation threshold. The composite conductivity in this case would be expected to be on the order of 10^{-5} S/cm. Changing polymerization conditions, in particular the surfactant used, might provide better coverage. In fact, a systematic study of reaction variables (surfactant type, surfactant amount, polymer amount) needs to be made for all three types of fillers. It may be possible to "fine tune" the plateau conductivity for a particular application by controlling these variables. Characterization of the conductivity as a function of both surfactant and monomer content should be obtained by varying each of these variables independently and measuring percolation diagrams.

The capability of using the modified particulate composites as temperature switching devices should be addressed through characterization of the temperature dependence of composite conductivity and could be carried out for both AC and DC conductivity. Experimentation into the time dependence of the conductivity would also help in understanding the reliability of devices produced from these conductive materials.

The mechanical properties of the composite films were not affected by the addition of the PPy coating due to the immiscibility of the PPy and LDPE. Other types of conductive polymers may be more compatible with the matrix polymer and better

adhesion at the filler-polymer interface could be achieved. This interface enhancement may increase the mechanical properties, while reducing the typical loss in conductivity associated with good polymer-filler adhesion by forming entanglements of the conductive polymer with matrix phase.

6.4 CONCLUSIONS

The morphology of the matrix and the structure of the polymer-filler interface play an essential role in the physical properties of the resulting composite. The experiments described in this dissertation have only begun to characterize the effect of the filler on the polymer and the interfacial phenomenon. By expanding this work, tailoring conductivity for specific applications through control of polymer morphology and filler coating might be possible.

APPENDIX A

X-RAY BEAM ALIGNMENT OF THE HUBER 6-CIRCLE DIFFRACTOMETER: STANFORD SYNCHROTRON RADIATION LABORATORY BEAM LINE: 7-2

A.1 INTRODUCTION

The procedure to align the Huber 6-Circle Diffractometer was compiled from notes taken at the Stanford Synchrotron Radiation Laboratory (SSRL) in January 1997. This document was updated from notes taken during beam alignment in February 1998 and from a short outline of alignment procedures provided by SSRL staff scientists.

A.1.1 Equipment Setup

Figure A-1(a) is a photograph of the Huber Diffractometer on beam line 7-2 at SSRL and Figure A-1(b) is a schematic diagram of the experimental setup. The x-ray beam is delivered to the hutch through a set of culmination slits with dimensions specified by the user, but set by the SSRL staff prior to the beam line being turned over to the users. After the x-ray beam enters the hutch, it through a vacuum flight path to scattering by air. A sets of slits are directly attached to the entrance of the flight path

that to eliminate beam broadening. An x-y positioner attached to the flight path was used to align the flight path with the beam. The x-ray beam then passes through the sample, which is attached to the χ -circle. Another set of slits, used to define the diffraction angle, is attached to the entrance of the flight path to the detector.

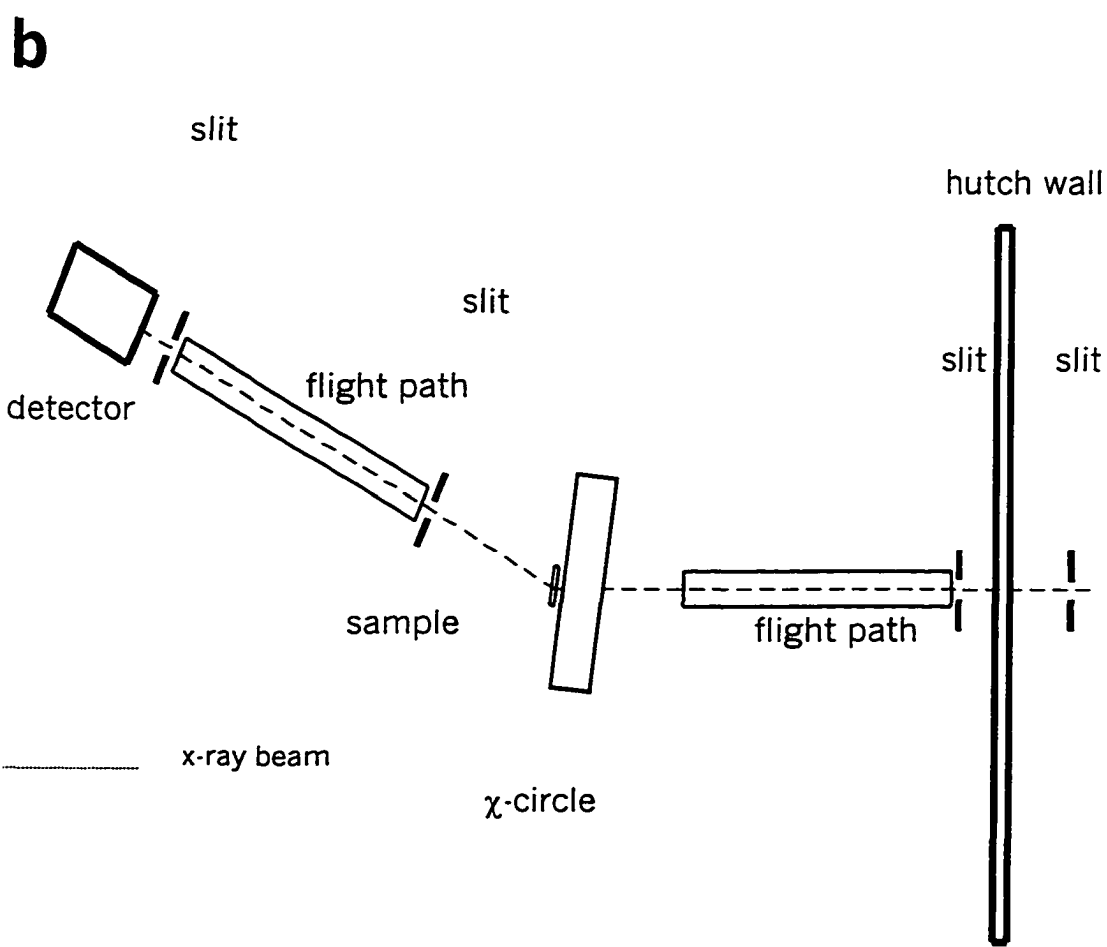
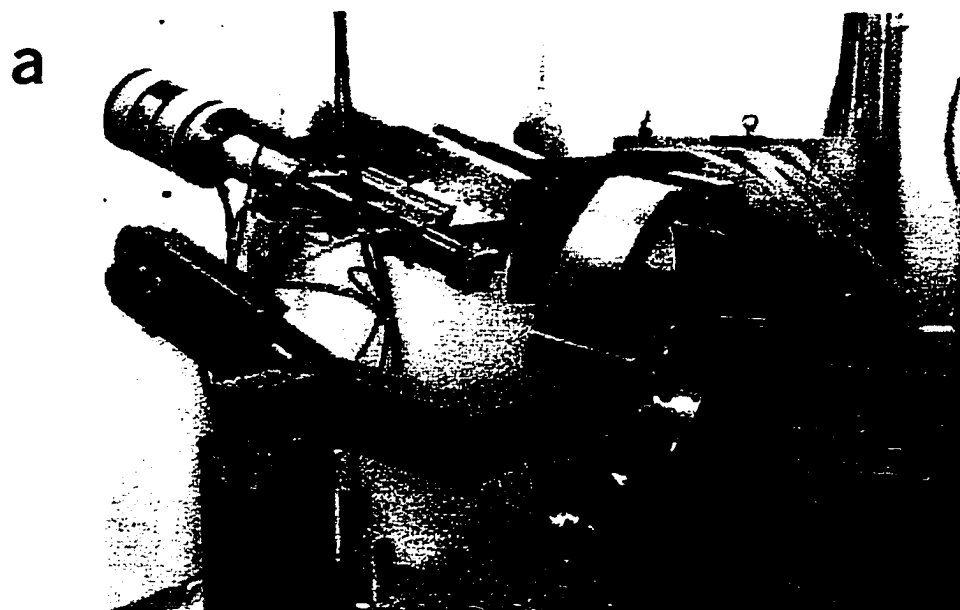
A.1.2 Overview of Alignment Procedures

The following steps are required in aligning the Huber 6-Circle Diffractometer:

1. Telescope Alignment - Align the center of the chi and phi circles with a pin, then align the cross-hairs of the telescope to the center of the chi circle.
2. Align the beam by setting a pinhole at the center of the chi circle and doing a horizontal and vertical table scan to find the maximum intensity.
3. Find 2-theta = zero by slitting down on the slits in front of the ionization chamber and doing a 2-theta scan. The point of maximum intensity is set as 2-theta = zero.
4. Set theta = 0
5. Center the initial intensity via the x-y positioner supporting the front slits and set the slit width and height.
6. Set the chi hardware and software limits.
7. Set the 2-theta hardware and software limits.
8. Set discriminator upper and lower limits from a known bragg reflection.

Note: Another set of motorized collimating slits located in front of the detector flight path can also be adjusted, but were left completely open for the experiments described in this dissertation.

Figure A-1 X-ray Experimental Setup a) Photograph b) Schematic Diagram



A.2 PRE-ALIGNMENT PROCEDURES

Most of the alignment procedure requires the measurement of the direct x-ray beam. The germanium detector used in the experiment cannot be used in the direct beam and must be replaced by an ionization chamber before alignment begins. The ionization chamber has two electronic hookups, the first for the high voltage power input - the red wire- (strait) and the second to be attached to the Keithley amplifiers - the green wire - (bent), then on to the computer system.

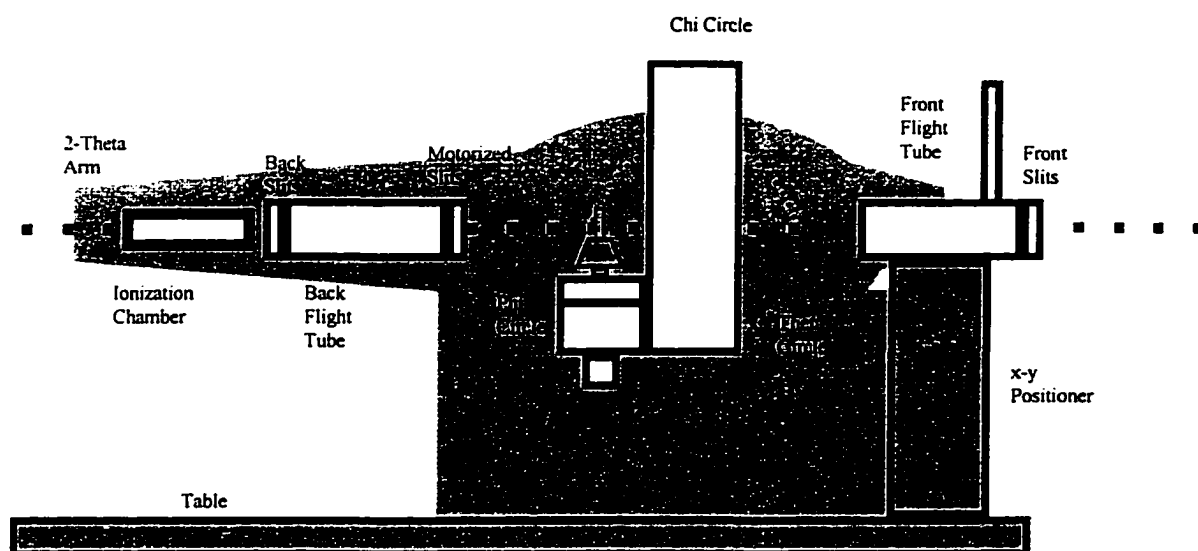
After the ionization chamber has been put in place, the 2-theta arm must be balanced to keep from over burdening the motor (see Figure A-2). This is done with weights located in the far left hand corner of the hutch or the diffractometer cabinet located across the pedestrian walkway. These should either be bolted into place or held into place by vinyl tape, which can be purchased from the storeroom. Balance is achieved when the set screw on the 2-theta arm can be released without significant movement of arm.

Note: After the ionization chamber is replaced with the Germanium Detector, the 2-theta arm must be re-balanced.

Before alignment begins, the motors to be used both for alignment and for the actual experiments must be set up on the computer. These motors include:

THETA
2THETA

Figure A-2 Side View of Huber Diffractometer with Ionization Chamber used in Alignment.



CHI
PHI
TABLE (TABLE VERTICAL)
THOR (TABLE HORIZONTAL)
VERT (X-Y POSITIONER VERTICAL)
HORZ (X-Y POSITIONER HORIZONTAL)
S2V (MOTORIZED SLITS VERTICAL)
S2H (MOTORIZED SLITS HORIZONTAL)

From the \$-prompt, you can list all motors by using the following command:

ASSIGN

The motor numbers can be changed or additional motors assigned by the set command:

SET [MOTOR NAME] AT [MOTOR NUMBER]

For example:

Set 2THETA AT M1

would set the 2THETA motor as motor 1. Up to 8 motors can be assigned. The motor properties can be viewed or changed via the motor control command by typing,

MOT/C

at the \$-prompt.

A.3 ALIGNMENT PROCEDURES

A.3.1 Chi and Phi Circle Alignment.

The chi and phi circles are made up of a Huber 512 eulerian cradle and a Huber 410 goniometer and the goniometer head is a Huber type 1003; these are depicted schematically in Figures A-3 and A-4. The chi and phi alignment allows rotation in

either direction without any spatial deviation. The rotation of the chi and phi circles is done manually during alignment by loosening the set screws on the side of each circle. These are large hexagonal screws, but are only finger tight and can easily be loosened. There are several directional controls that can be adjusted in order to obtain this alignment. The first is the z-control on the Huber 410 goniometer, located at the bottom of the goniometer. The second the x and y positioners on the Huber 1003 Goniometer head. A special tool is required in order to make these adjustments. The third is the diagonal adjustment on the Goniometer head. Place the calibration pin, shown in Figure A-5, in the Goniometer head and view through the telescope while making all adjustments.

- Rotate the Chi Circle while making adjustments to the three dimensional controls.
- Rotate the Phi Circle While making adjustments to the three dimensional controls.
- Repeat this process until there is no spatial deviation upon rotation in both the chi and phi directions.

After the Chi and Phi alignment is finished, the telescope must be set such that the cross-hairs are aligned directly on the center of the pin (which should be exactly at the center of the Chi circle). This is done by loosening the allen screws holding the telescope in place and making the appropriate adjustments.

Figure A-3 Side View of Chi and Phi Circles

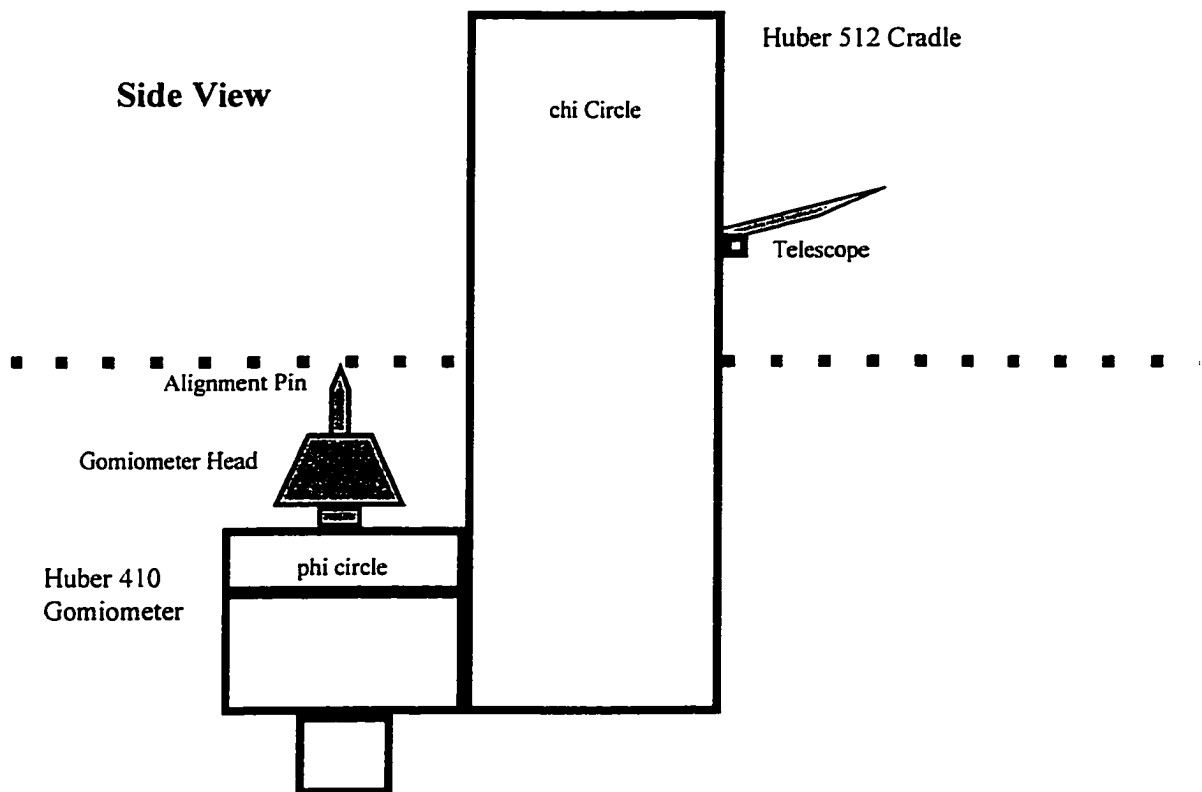


Figure A-4 Front View of Chi and Phi Circles

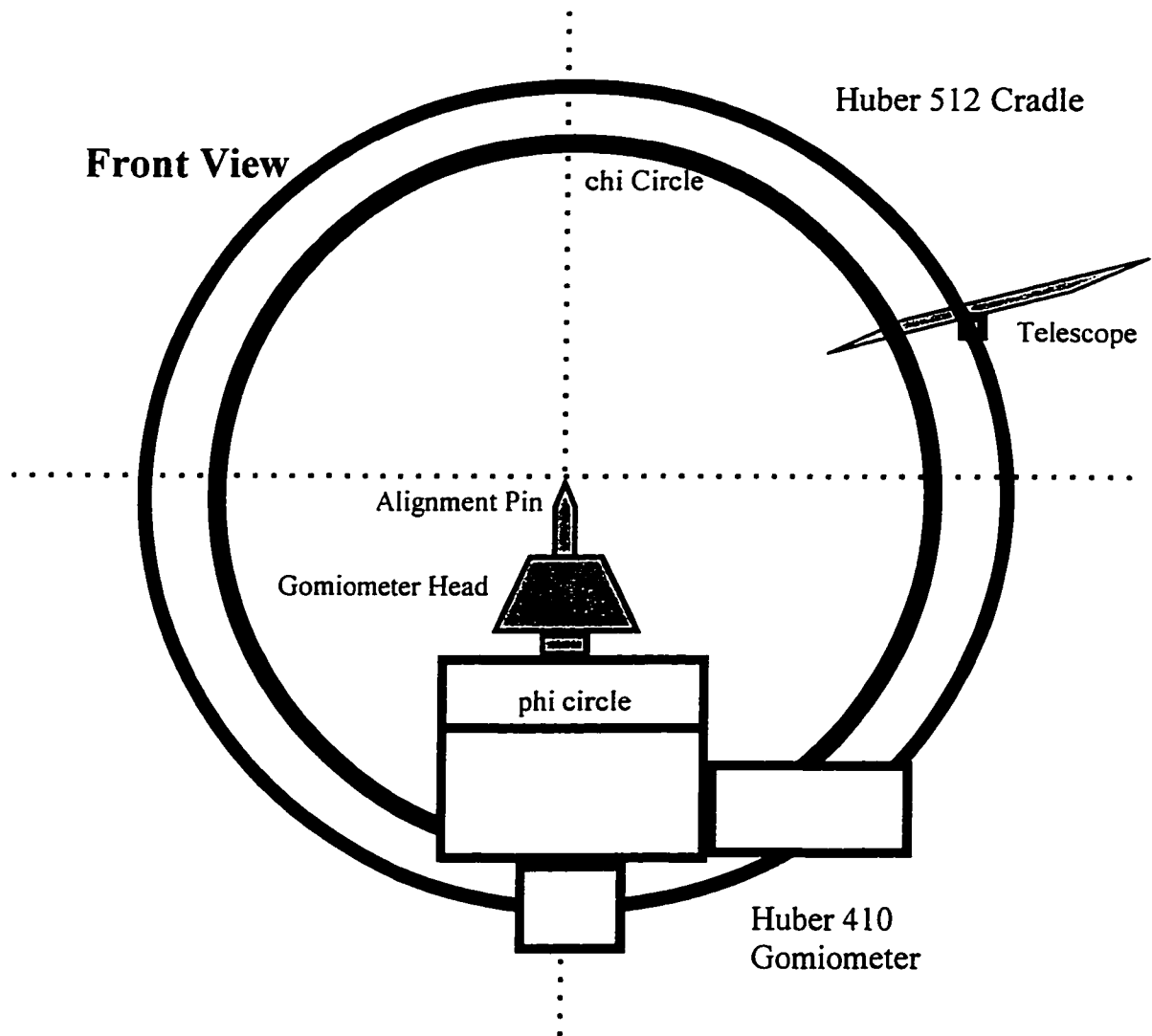
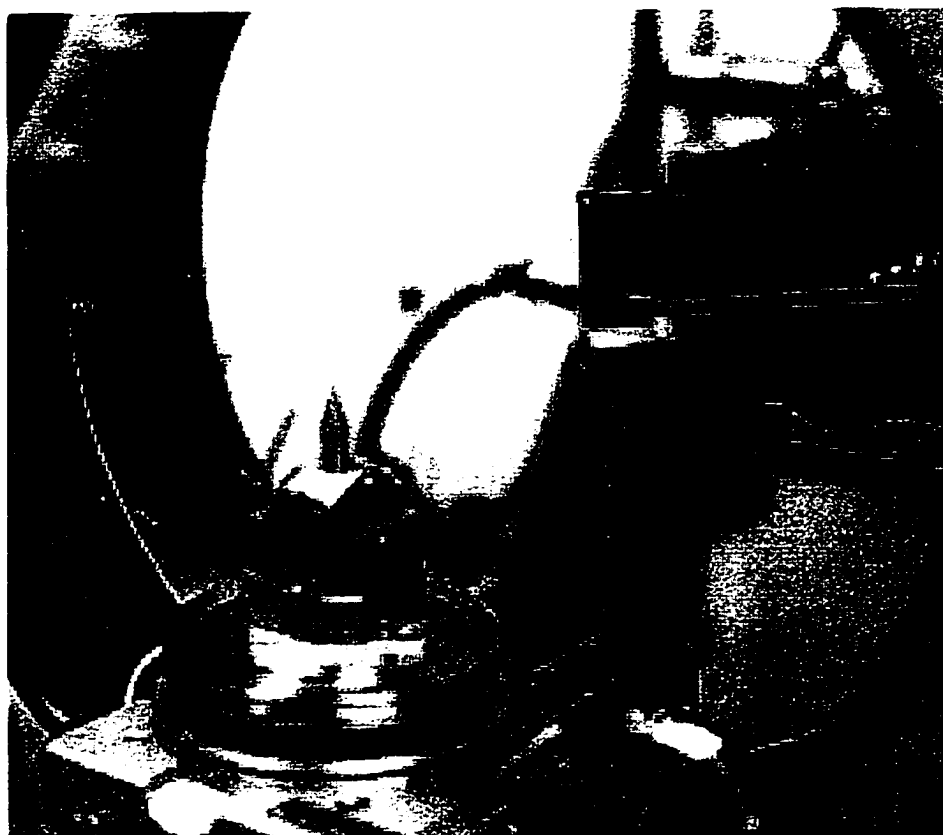


Figure A-5 Photograph of Chi and Phi Circles with Calibration Pin in Goniometer Head.



A.3.2 Beam alignment through the center of the chi circle.

Figure A-2 is a schematic drawing of the Huber Diffractometer, as it would be arranged for alignment for the pole figure measurements. The Germanium Detector must be replaced with the ionization chamber and the 2-theta arm must be balanced as discussed above. The pin (from Section A.3.2) in the Huber Goniometer Head model 1003 is replaced with an alignment pinhole through an absorbing lead shield as shown in Figures A-6 and A-7.

Open all three sets of slits and follow the procedure listed below:

A.3.2.1 Vertical Alignment

- Do a LINE SCAN above and below the pinhole. By the following command:

LINE [MOTOR] [INCREMENT] [NUMBER OF POINTS]

- The increment is the distance between points and the number of points is the number both before and after the point at which the motor is currently located. For example:

LINE TABLE 0.1 20

- This line scan will scan 20 points every 0.1 millimeters above and below the height at which the vertical motor is located for a total of 40 points.

Figure A-6 Pinhole for Alignment

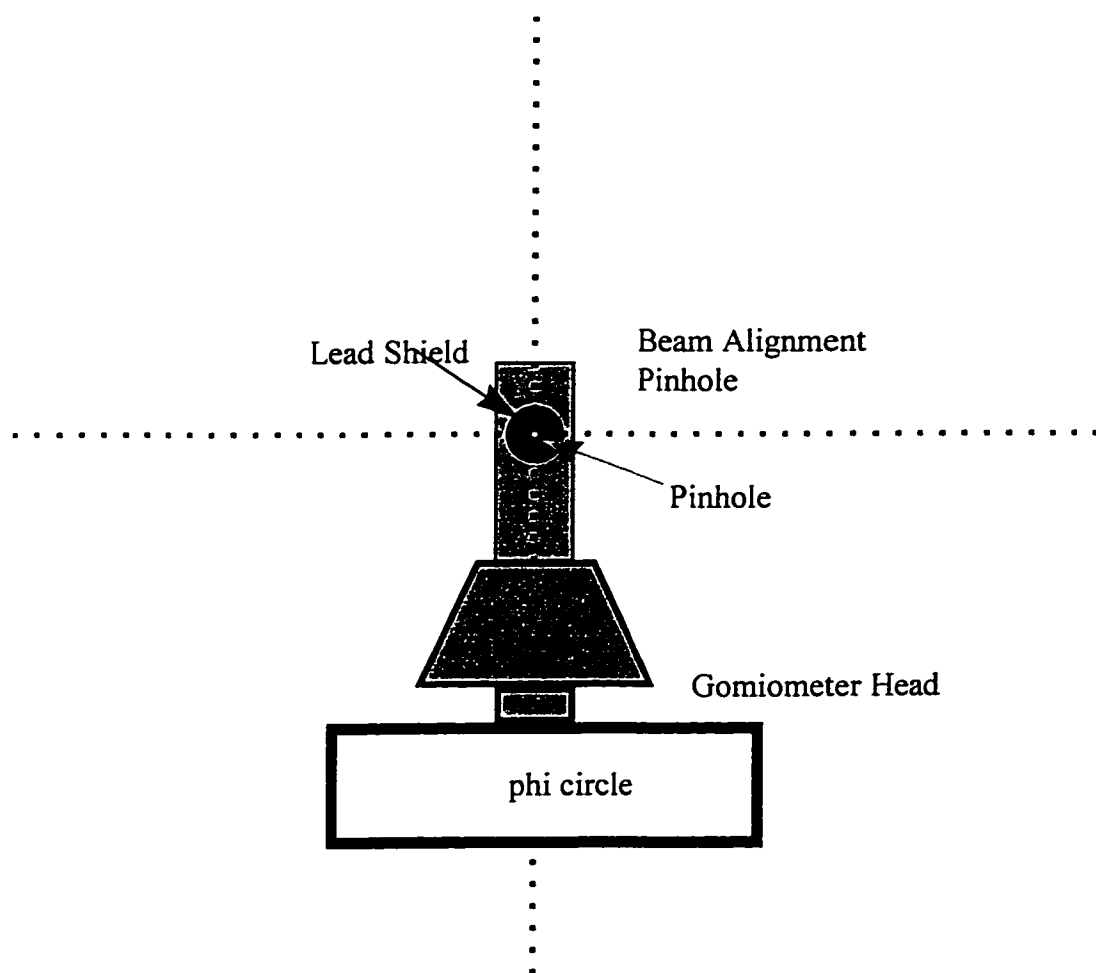


Figure A-7 Photograph of Pin Hole on Goniometer Head



- Line Scan can the table vertically and plot this in s-plot
- To start s-plot open a new window and at the \$ prompt type:

SPL

Once the SPL prompt has been obtained, type: **DISPLAY**

- To watch the progress, type:

UPDATE/REPEAT

- When the scan has fished press [CONTROL][C] to stop the display, then at the prompt type:

FIT

- One of the items listed by the fit is the maximum value. If you prefer to find this point from the data itself, type:

CURSUR

- Now set the table vertical motor to the height that corresponds to the maximum intensity by typing:

TABLE [MAXIMUM VALUE]

- For example, if the maximum value occurred at 45.35 millimeters then to set the table to 45.35 millimeters type:

TABLE 45.35

Repeat this process for smaller values of the increment until satisfied that the maximum intensity is going through the center of the hole.

A.3.2.2 Horizontal Alignment

The procedure for the horizontal alignment is the same as vertical alignment, except motor THORZ is being optimized.

The line scan would be as follows:

LINE THORZ 0.1 20

Setting the motor position would follow the as follows:

THORZ 16.25

A.3.3 Setting 2-THETA = zero

Setting 2-THETA to zero is done by doing a line scan with the 2THETA motor and optimizing the intensity.

- The line scan is set by the following command line:

LINE 2THETA 0.1 20

- Follow the same procedure as in the table alignment in order to determine the maximum position.
- To set the value first move the motor to the maximum position by a command line similar to:

2THETA 2.15

- To reset 2.15 (or whatever the value is) to zero type:

2THETA/RESET 0

- Repeat with smaller increments to optimize this procedure.

A.3.4 Set Theta = 0.

THETA was set equal to zero by using a removing the set screw on the front end of the diffractometer and using a level to determine the point where it was perpendicular to the table. This is not an exact technique, but since the theta will not be used in the experiment, it was not necessary to be more exact than this.

A.3.5 Set Front and Back Slits

- Remove the pinhole.

A.3.5.1 Front Slits

A.3.5.1.1 Vertical Alignment

- Set the vertical position on the front slits
- Do a LINE scan with the VERT motor
- Move the motor at the maximum intensity
- Repeat until optimized

A.3.5.1.2 Horizontal Alignment

- Set the horizontal position on the front slits
- Do a LINE scan with the HORZ motor
- Move the motor at the maximum intensity
- Repeat until optimized

A.3.5.2 BACK SLITS

- Set the vertical and horizontal slits at the desired dimensions.
- Repeat the 2THETA motor alignment with very small increments.

Note: This also optimizes the 2THETA alignment using the smaller beam size.

A.3.6 Set Chi hardware and software limits

A.3.6.1 Hardware Limits

- Set the minimum angle the chi motor will move without binding the electrical cords or contacting/damaging any other equipment. This is a limit switch which will turn off the motor if contacted
- This is done by placing the switch at the appropriate angle and tightening the set screw.

A.3.6.2 Software Limits

- Set the software limits for each motor in the computer by going to the motor control screen:

MOT/C

- Then change the limit by typing:

Ph1

- It is best to set these limits based on what your experiment will require while setting the hardware limits based on what the equipment can do thus giving a double check that the equipment will not be damaged.

A.3.7 Setting the 2THETA Hardware and Software Limits

A.3.7.1 Hardware Limits

- The hardware limits are set by the same procedure for the CHI limits except the major considerations are to have the germanium detector NEVER be directly in the beam. The lower limit must be at least 3°.

A.3.7.2 Software Limits

- Software limits are set by the same procedure as for the CHI software limits.

A.3.8 Set Discriminator Limits

- The discriminator removes all signals except those coming from the desired components (i.e. inelastic scattering).
- Replace the ionization chamber with the germanium detector.
- Balance the 2THETA arm.
- Set 2Theta at a known diffraction angle for a known sample (alumina in our case).
- Set the upper and lower windows of the discriminator using the oscilloscope as a guide
- NOTE: I may need a little help with this one determining which signal is the primary signal.

A.4 HELPFUL SSRL STAFF

- Bart Johnson bart@slac.stanford.edu

- Sean Brennan bren@slac.stanford.edu
- John Arthur jarthur@slac.stanford.edu
- Tom Hostetler hostetler@slac.stanford.edu
- Dave Day dday@slac.stanford.edu
- Duty Operators

APPENDIX B

DSC CALIBRATION PROCEDURES

B.1 INTRODUCTION

This appendix is designed to be a systematic procedure for obtaining a baseline and calibrating the DSC II and supersedes the operation manual due to the modifications to the cooling system and the addition of a computerized data acquisition. Due to the different types of experiments possible with DSC equipment, this appendix only outlines setting up the equipment, obtaining a baseline, and calibration of the temperature scale.

B.2 EQUIPMENT SET UP

1. The computer used with the DSC-II is on a cart and is also used in data collection with other equipment. Two wires, white and gray, are attached to the DAS800 board in the computer. Attach the wires as labeled on the yellow wires on the DSC.
2. Turn power on to both the DSC and the computer.
3. Connect the helium cylinder to the purge line and set the regulator at a discharge pressure of 20 psi.

4. Connect the nitrogen cylinder to the glove box gas inlet connection. Set the flow to 10 scfh.
5. The DSC is equipped with a connection and hose for a 160L dewar of liquid nitrogen (LN). Connect the LN dewar and open the liquid valve on the top. Allow the DSC to fill until the level indicator reaches the first black line, then shut the valve.
6. Allow the system to equilibrate for approximately 60 minutes. Additional LN will be required during the equilibration.

B.3 BASE LINE CALIBRATION

Before beginning the calibration of the baseline, the high temperature (T_H) and low temperature (T_L) must be determined. It is suggested T_H be set at least 50° above T_L be set at least 50° below the temperature range of interest in the experiments. The scanning rate (SR) should also be re-determined.

1. Set cooling rate to 320° per minute.
2. Set heating rate to SR.
3. Set low temperature set point to T_L .
4. Set high temperature set point to T_H .
5. Set range to 10 mcal.
6. Place empty aluminum pans in both the sample and reference holders.
7. Use the program:
 - c:\das800\temp\dscbgd.exe
 - Start Temp. = T_L
 - End Temp. = T_H

- Scanning Rate = SR

8. Press the heat button and enter simultaneously.

9. View baseline on computer to determine needed changes; Figure B-1 shows the effects of different control changes.

- Should changes in the ΔT_b be required, an estimate of the numerical change required can be obtained from Equations B-1 and B-2, with H estimated as shown in Figure B-2 (in inches).

$$\Delta T_b = H * 60 \quad [B-1]$$

$$T_b = T_b + \Delta T_b \quad [B-2]$$

10. Repeat as necessary. An acceptable baseline has a variation between the beginning and ending of less than 50 arbitrary units (AU).

The calibrated base line, as depicted schematically in Figure B-3, will have program peaks at the initial and final temperatures.

B.4 TEMPERATURE RANGE CALIBRATION

B.4.1 Gallium Sample

1. Load an empty pan into the reference chamber.
2. Load the gallium sample into the sample chamber.
3. Heat or cool chamber to 280°K.
4. Start computer program:
 - C:\das800\temp\dscal.exe

Figure B-1 Changes in DSC Controls; a) Calibration Zero; b) Calibration Range; c) ΔT_b ; Clockwise and Counterclockwise refer to the rotation of the control knob

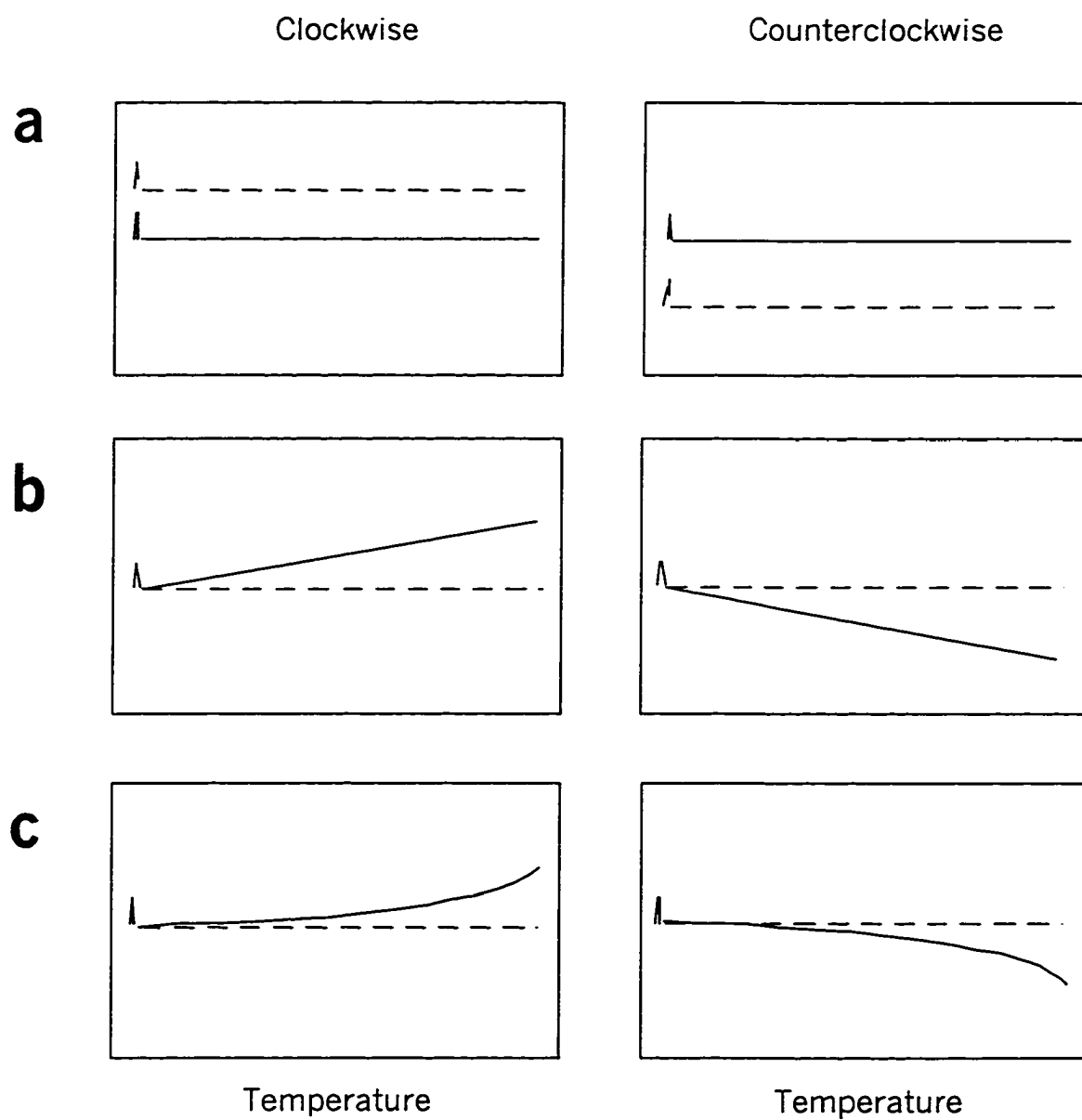


Figure B-2 ΔT_b Change Estimation; Initial and Final Peaks are Program Peaks

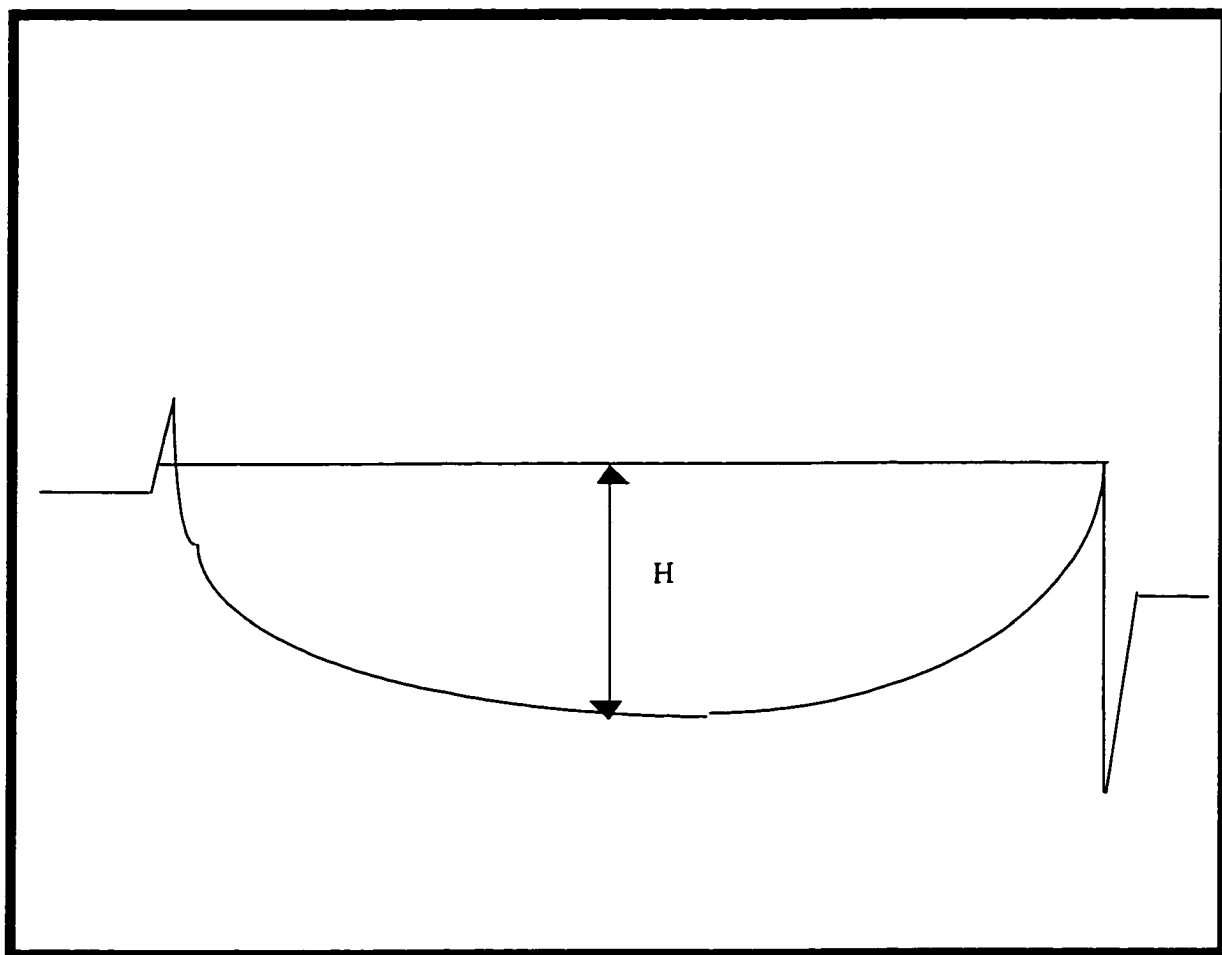
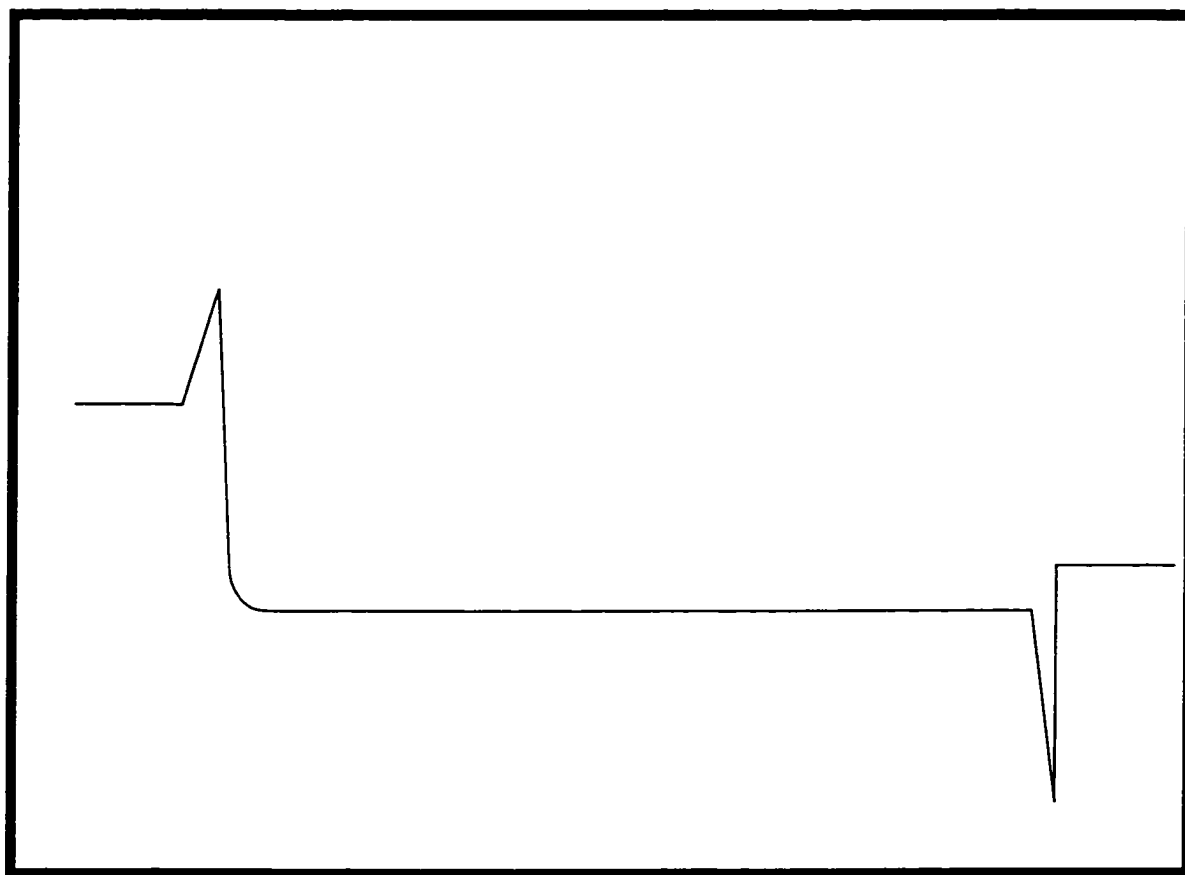


Figure B-3 Schematic Diagram of Base Line with Initial and Final Temperature Program Peaks



- Start Temp = 280
- End Temp = 320
- Scan Rate = SR

Note: The melt temperature of gallium is 302.9°K.

5. Press the heat button and enter on the computer simultaneously.
6. Determine the melt temperature from the DSC output using the dsccal.exe graphics routine.

B.4.2 Indium Sample

1. Load an empty pan into the reference chamber.
2. Load the indium sample into the sample chamber.
3. Heat or cool chamber to 415°K.
4. Start computer program:
 - C:\das800\temp\dsccal.exe
 - Start Temp = 415
 - End Temp = 440
 - Scan Rate = SR

Note: The melt temperature of indium is 429.8°K.

5. Press the heat button and enter on the computer simultaneously.
6. Determine the melt temperature from the DSC output using the dsccal.exe graphics routine.

B.4.3 Determine New Temperature Calibration Range Setting

1. Determine the indicated difference between the melting points of gallium and indium.
2. Use Equations B-3 to determine the change in the range calibration setting. The actual difference in melting points of gallium and indium, ΔT_{act} , is 126.9°.

$$\Delta R = R^2 \left[\frac{\Delta T_{\text{ind}} - \Delta T_{\text{act}}}{\Delta T_{\text{act}}} \right] * \frac{1}{1000} \quad [\text{B-3}]$$

3. The new temperature calibration range setting is determined by Equation B-4.

$$R = R + \Delta R \quad [\text{B-4}]$$

4. Change the Temperature Range Calibration to the new setting, R.
5. Repeat this the procedure outlined in Section B.4 until the difference between the melting points of gallium and indium is 126.9°.

B.5 TEMPERATURE ZERO CALIBRATION

1. Load the gallium sample in the sample chamber.
2. Set heating rate to SR.
3. Heat or cool chamber to 280°K.
4. Start computer program:
 - C:\das800\temp\dscal.exe
 - Start Temp = 280
 - End Temp = 320

- Scan Rate = SR

Note: The melt temperature of gallium is 302.9°K.

5. Press the heat button and enter on the computer simultaneously.
6. Adjust the temperature calibration zero; clockwise to adjust the temperature lower; counterclockwise to adjust the temperature higher.
7. Repeat this process until the gallium melt temperature reads 302.9°K.

B.6 ENERGY CALIBRATION

1. Load the indium sample in the sample chamber.
2. Set heating rate to SR.
3. Heat or cool chamber to 280°K.
4. Heat until the indium melt peak is produced (T=429.8°K).
5. Calculate the area under the peak, A.
6. The transition energy, ΔH_t , for indium is 6.8 cal/gram and is equal to the Equation B-5.

$$\Delta H_t = \frac{K * r * A}{w * S} \quad [B-5]$$

Where K is DSC calibration constant, r is range sensitivity, w is weight of sample, and S is 1. K is determined by rearranging Equation B-5, as shown in Equation B-6.

$$K = \frac{\Delta H_t * W * S}{R * A} \quad [B-6]$$

The energy calibration can also be done with gallium; the transition energy is 19.19 cal/gram.

B.7 ADDITIONAL NOTES

- If using oriented samples, you can only get one heating because the heating will change the morphology of the sample.
- The base line is sensitive to the liquid nitrogen level. For optimal results, the liquid nitrogen should be refilled to the first black line between each step of calibration and between each sample.

APPENDIX C

TTF SYNTHESIS

C.1 INTRODUCTION

Tetrathiafulvalene (TTF) was synthesized and purified by a three-step procedure adapted from Narita and Pittman.¹

1. Synthesis of 1,3-dithiole-2-thione (intermediate)
2. Synthesis 1,3-dithiolium hydrogen sulfate (intermediate)
3. Synthesis of TTF

This appendix is designed to be a step-by-step procedure.

C.2 SYNTHESIS PROCEDURE

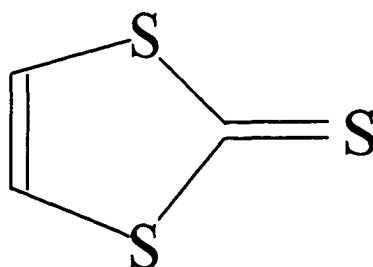
C.2.1 1,3-dithiole-2-thione

C.2.1.1 Synthesis

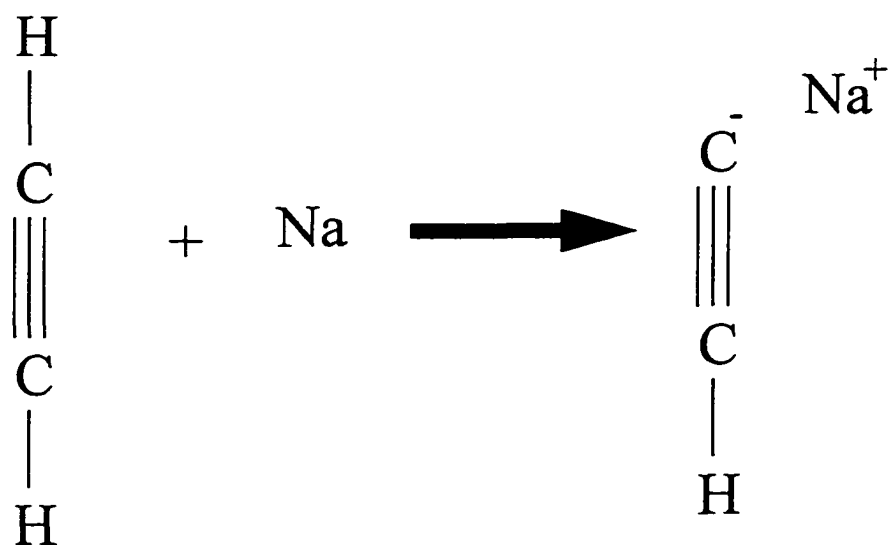
1. Obtain 10 lbm dry ice from the chemistry stock room.
2. Add the dry ice to the baths filled with propanol.
 - The first bath contains the stainless steel condenser.

Figure C-1 a) 1,3-dithiole-2-thione; b) Synthesis of Sodium Acetylenide

a



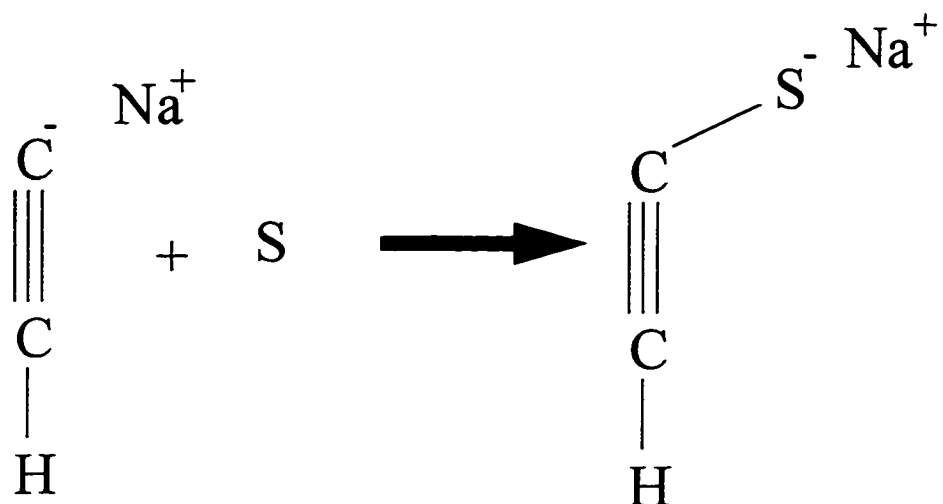
b



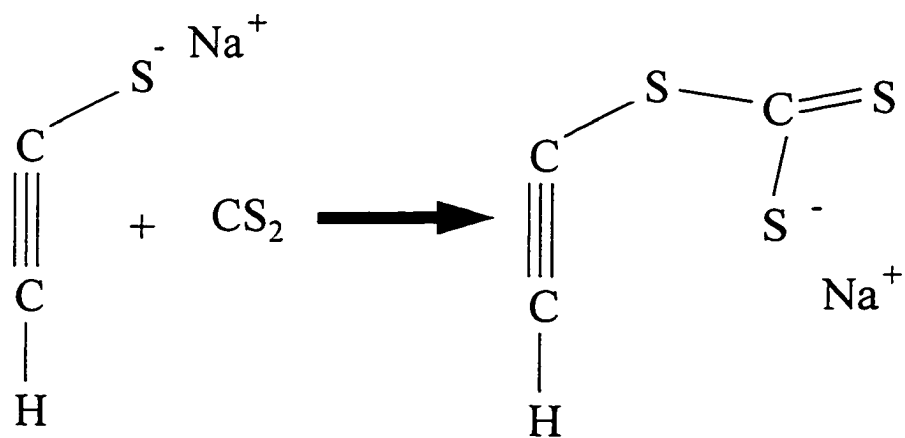
- The second bath contains the 1 liter reactor (orange top 1 liter flask).
3. Condense 600 milliliters of ammonia into the reactor
 4. The reactor contains 3 holes:
 - Nitrogen spurge/blanket.
 - Acetylene inlet.
 - Purge hole.
 5. Add 9.2 grams (0.4 mole) of sodium in small chunks.
 - The sodium was is cut using an exacto knife with a clean blade on a clean rubber mat. Sodium reacts violently with water and care must be taken not to have any moisture contact.
 - The sodium is weighted in a polypropylene petri dish.
 - When the sodium is added to the reactor, the ammonia turns a deep blue color. Give 10 to 15 minutes to allow all of the sodium to dissolve.
 - After the sodium has been charged to the reactor, fill the petri dish with the residual solvent with propanol. The propanol reacts with the with the sodium slowly.
 6. Bubble acetylene in until all the sodium is reacted
 - at dry ice temperatures this is approximately 2 minutes.
 - This is indicated by the solution turning a milky white color.
 7. Add 400 milliliters of anhydrous ether.
 - The ether is introduced using a funnel through the same port used for sodium.

Figure C-2 a) Reaction of Sodium Acetylenide with Sulfur b) Reaction with Carbon Disulfide

a



b



- This must be added in two 200 milliliter portions in order for the solution to stay below the boiling point of ammonia.
8. Add 12.8 grams (0.4 mole) of sulfur.
 - In order to keep the sulfur powder from being fluidized, the nitrogen purge must be turned off during the sulfur addition.
 - Make sure to restart the nitrogen purge after the addition of the sulfur.
 - As the sulfur reacts, the solution turns a deep purple color.
 9. Add a magnetic mixer to the solution.
 10. Remove reactor from dry ice bath and place it on a stirring hot plate at a low temperature setting (3) and a medium to high mixing speed (6).
 11. Allow ammonia to evaporate - takes about 1 1/2 hours for the reactor to heat to room temperature and the ammonia to evaporate.
 - The solution was kept under nitrogen during the entire operation.
 - When the solution has reached room temperature, turn off the heat part of the hot plate, but continue to stir the mixture.
 12. Add 600 milliliters of acetonitrile.
 13. Two 120 milliliter container fixed with a lid and tube for pumping were prepared with the following ingredients:
 - 12 milliliters of carbon disulfide.
 - 100 milliliters of anhydrous ether.
 14. Pump the carbon disulfide solution into the reaction vessel slowly of 1 hour.
 15. Allow the solution to react for an additional hour.
 16. Add 100 milliliters of 12M hydrochloric acid to 100 milliliters of deionized water.

17. Add the acid mixture to the reaction mixture.

18. Allow the solution to mix for 10 minutes.

C.2.1.2 Separation

C.2.1.2.1 Filtration

1. Filter the solution.
2. Phase separate the water and organic phase.

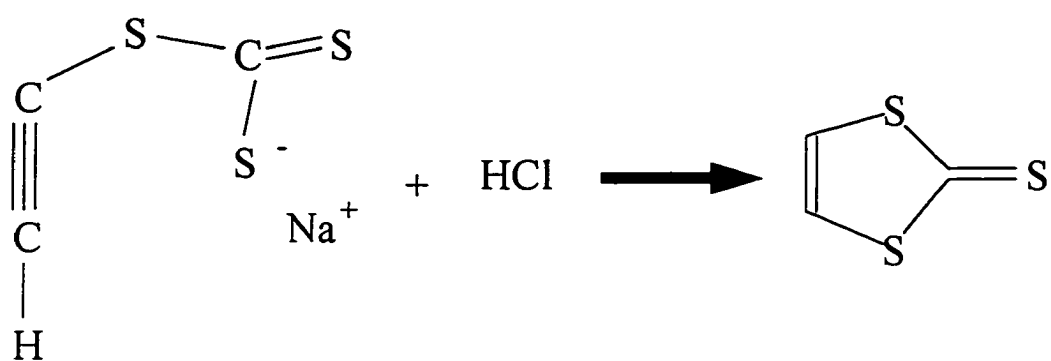
C.2.1.2.2 Ether Liquid-Liquid Extraction

1. Add 100 milliliters of anhydrous ether to the water phase.
2. Phase separate the water and ether phases. Add the ether to the organic phase.
3. Repeat step 22 additional several times (approximately 1 liter of ether used in the extraction).
4. Add 2 grams of magnesium sulfate to dry the organic phase and stir.
 - Allow at least 2 to 4 hours, but it is good if you let it set overnight.
5. Filter the solution to remove the magnesium sulfate.
6. The ether was removed by distillation (bp 38°C).
7. Filter the solution to remove black by-products.

C.2.1.2.3 Methylcyclohexane Liquid-Liquid Extraction

1. 200 milliliters of methylcyclohexane brought to a boil.

Figure C-3 Acidification



- The boiling point is 101.8°C.
2. Add the boiling methylcyclohexane to the acetonitrile phase.
 3. The solution was phase separated.
 4. The liquid –liquid extraction with methylcyclohexane was repeated four times.

C.2.1.2.4 Crystallization of 1,3-dithiole-2-thione

1. Distill the solution to remove all residual acetonitrile and all of the methylcyclohexane so the mother liquor contains 300 milliliters.
2. Filter the solution to remove byproducts that were carried into the reaction mixture by the residual acetonitrile.
3. Place the solution in a 500 milliliter beaker with a stopper and seal with parafilm.
4. Place in freezer overnight to allow crystallization to take place.
5. Separate the methylcyclohexane from the crystals by allowing the crystals to settle in a glass petri dish and taking the liquid off the top.
6. Allow the crystals to dry in the glove box for 48 hours.

The crystals are yellow-orange in color and have a melting point of approximately 49°C, which was measured by DSC to ensure the correct product was obtained. The reaction yield was low and several batches were required before enough 1,3-dithiole-2-thione was obtained to use in the next step of the synthesis. Refrigeration was required in order to keep the intermediate from reacting.

C.2.2 Synthesis of 1,3-Dithiolium Hydrogen Sulfate

The 1,3-dithiole-thione synthesized by the procedure in Section C.2.1 was reacted with peracetic acid to form a salt, 1,3-dithiolium hydrogen sulfate.

1. Obtain dry ice from the chemistry store room.
2. Form a dry ice bath by adding dry ice to 2-propanol in a insulated container.
3. Dissolve 12.7 grams (0.095 mol) of 1,3-dithiole-thione in 250 milliliters of reagent grade acetone in a 1 liter reactor.
 - MW (1,3-dithiole-thione) = 134.24 g/mol.
4. Place the solution in the dry ice bath and cool to -50°C.
5. Add 0.38 mol of peracetic acid (dissolved in acetic acid) to 150 milliliters of reagent grade acetone.
 - The density of the peracetic/acetic acid solution is 1.130 g/cc.
 - The molecular weight of the peracetic acid is 76.05 g/mol.
 - The weight fraction of the peracetic/acetic acid solution is 32 percent peracetic acid.
 - The volume of acid solution to add to the acetone is 80 milliliters.
6. Charge approximately 50 milliliters of the peracetic/acetic acid/acetone solution to the reactor.
7. Remove the reactor from the dry ice bath.
8. Allow the reactor to warm to 15°C.
9. Place the reactor back in the dry ice bath and cool to -50°C.
10. Repeat steps 6 through 9 until all of the acid solution has been charged to the reactor. While the reactor is at approximately 15°C, filter the solution using the vacuum filter to collect the solids (1,3-Dithiolium Hydrogen Sulfate).

11. Dry the salt overnight in the glove box.

The physical appearance of the salt is brown/orange (like dirt). The yield was approximately 87 percent (16.6 grams).

C.2.3 TTF Synthesis

The final product, tetrathiafulvalene (TTF) was formed by coupling the 1,3-dithiolium hydrogen sulfate.

1. Dissolve 0.03 moles (6.0 grams) of 1,3-dithiolium hydrogen sulfate (MW = 200.2 grams per mole) in 200 milliliters of acetonitrile.
2. Add a nitrogen inlet so the reaction can be done in an inert environment.
3. Add a magnetic stirrer.
 - note that the dithiolium hydrogen sulfate does not completely dissolve in the acetonitrile.
4. Purged the solution with nitrogen for 15 minutes.
5. Add 5 milliliters of triethylamine (0.035 moles) was added dropwise over a 15 minute period.
 - Triethylamine MW = 101.19 grams per mole.
 - Triethylamine density = 0.726 grams per milliliter.
6. Allow the solution to react for an additional 15 minutes.
7. Add excess deaired water to precipitate the TTF.
8. Stir for 10 minutes.
9. Filter to collect the solids.
10. Dry in glove box overnight.

11. Dissolve the filtrate in boiling cyclohexane.

12. Dilute with n-hexane.

13. Cool overnight at 5°C (in refrigerator).

14. Separate crystals from mother liquor.

15. Allow crystals to dry in glove box.

16. Distill the mother liquor to 150 milliliters.

17. Cool overnight at 5°C.

18. Separate crystals from mother liquor.

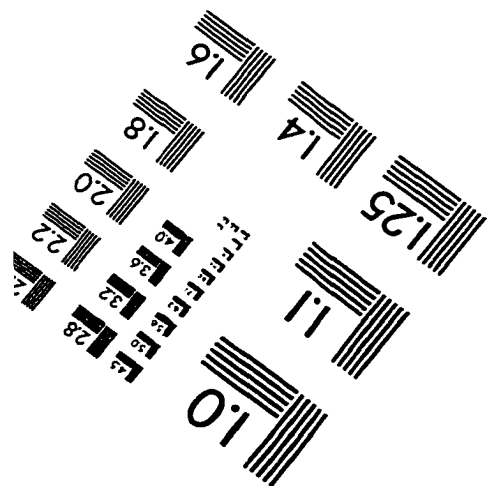
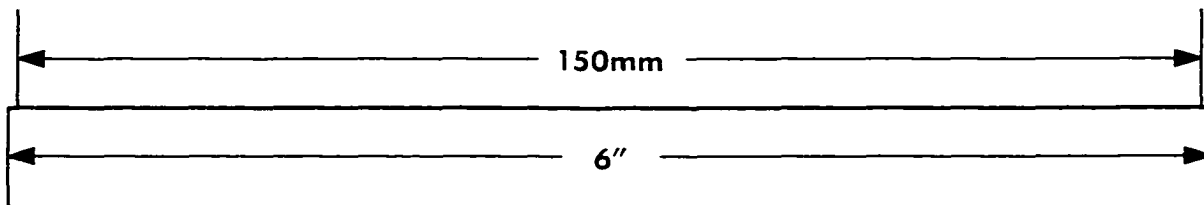
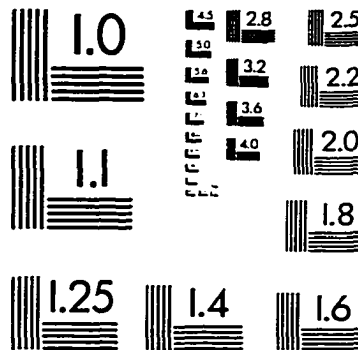
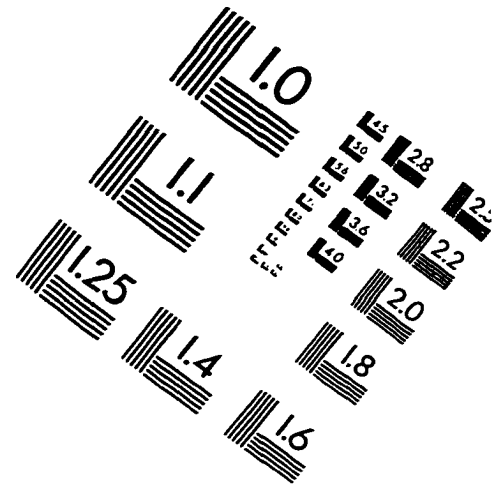
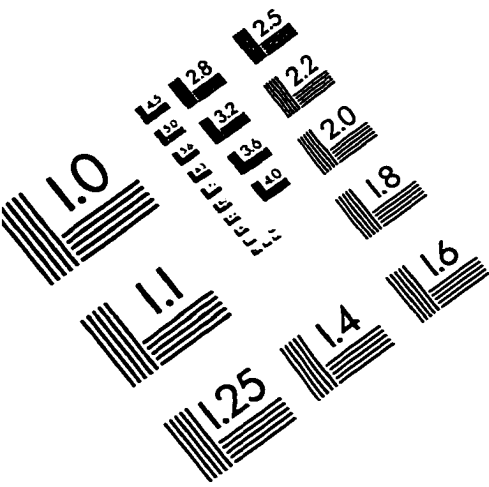
19. Allow crystals to dry in glove box.

Yield was approximately 80 percent. The product was a long orange needle with a melting point of approximately 119.5°C as determined by DSC.

C.3 REFERENCES

- 1 M. Narita, and C.U. Pittman, Jr., *Synthesis*, 489 (1976).

IMAGE EVALUATION TEST TARGET (QA-3)



APPLIED IMAGE, Inc
1653 East Main Street
Rochester, NY 14609 USA
Phone: 716/482-0300
Fax: 716/288-5989

© 1993, Applied Image, Inc., All Rights Reserved

